Dissertation
submitted to the
Combined Faculties for the Natural Sciences and for Mathematics
of the Ruperto-Carola University of Heidelberg, Germany
for the degree of
Doctor of Natural Sciences

presented by

Oliver Thomas Niedermaier

born in Ravensburg

Oral examination: 06.07.2005

Low-Energy Coulomb Excitation of the Neutron-Rich Mg Isotopes ^{30}Mg and ^{32}Mg

Referees: **Prof. Dr. Dirk Schwalm**

Prof. Dr. Hans Emling

Abstract

The first "safe" Coulomb excitation experiments with beam energies below the Coulomb barrier have been performed at the newly commissioned radioactive beam facility REX-ISOLDE at CERN in conjunction with the modern HPGe γ-spectrometer MINIBALL. REX-ISOLDE and MINIBALL offer unique possibilities to study collective and single-particle properties of nuclei far from stability by standard techniques such as "safe" Coulomb excitation and transfer reactions in inverse kinematics.

From the Coulomb excitation experiments with beams of ^{30}Mg and ^{32}Mg, the reduced transition probabilities $B(E2;\ 0^+_{\rm g.s.} \rightarrow 2^+_1)$ of these isotopes could be extracted in a model-independent way to be $253\,(21)\ e^2{\rm fm}^4$ and $434\,(52)\ e^2{\rm fm}^4$, respectively. While the $B(E2)\uparrow$ value of ^{30}Mg is that expected for a pure *sd*-shell nucleus, the unusually large collective value observed for the "semi-magic" $N = 20$ nucleus ^{32}Mg reflects the vanishing neutron shell gap between *sd*- and the $f_{7/2}$-shell configurations which has been conjectured for the neutron-rich isotopes of Ne, Na and Mg. The large $B(E2)\uparrow$ value of ^{32}Mg can indeed be well described by a pure intruder configuration. The present result thus manifests a surprisingly abrupt transition to the so-called "island of inversion" between ^{30}Mg and ^{32}Mg.

Zusammenfassung

An dem neu in Betrieb genommenen Beschleuniger für radioaktive Strahlen REX-ISOLDE am CERN wurden die ersten Experimente zur niederenergetischen Coulomb-Anregung mit Strahlenergien unterhalb der Coulomb-Barriere unter Benutzung des modernen, hochauflösenden Ge-Spektrometers MINIBALL durchgeführt. REX-ISOLDE und MINIBALL bieten einzigartige Möglichkeiten, kollektive und Ein-Teilchen-Eigenschaften von Kernen weitab der Stabilität mit Hilfe von Standardtechniken wie der niederenergetischen Coulomb-Anregung und Transferreaktionen in inverser Kinematik zu untersuchen.

Aus den Experimenten zur Coulomb-Anregung von ^{30}Mg und ^{32}Mg konnten die reduzierten Übergangswahrscheinlichkeiten $B(E2;\ 0^+_{\rm g.s.} \rightarrow 2^+_1)$ dieser Isotope modellunabhängig zu $253\,(21)\ e^2{\rm fm}^4$ bzw. $434\,(52)\ e^2{\rm fm}^4$ bestimmt werden. Während der $B(E2)\uparrow$-Wert von ^{30}Mg für einen Kern der *sd*-Schale erwartet werden konnte, spiegelt der ungewöhnlich grosse, kollektive Wert des semi-magischen ($N = 20$) ^{32}Mg-Kerns das Verschwinden der Neutron-Schalen-Lücke zwischen der *sd*- und der $f_{7/2}$-Schale wider, was für die neutronenreichen Ne-, Na- und Mg-Isotope vermutet wurde. Der grosse $B(E2)\uparrow$-Wert von ^{32}Mg kann in der Tat gut mit Hilfe einer reinen Intruder-Konfiguration beschrieben werden. Das vorliegende Ergebnis offenbart daher einen überraschend abrupten Übergang zur sogenannten "Insel der Inversion" zwischen ^{30}Mg und ^{32}Mg.

Contents

1 Introduction **1**

2 Low-energy Coulomb excitation **7**
2.1 Excitation cross section 7
2.2 First order perturbation theory 9
2.3 Coulomb excitation parameters 10
2.4 "Safe" Coulomb excitation 12
2.5 Comparison to high-energy Coulomb excitation 12
2.6 Angular distributions 14
2.7 Deorientation effect 14
2.8 Experimental method 15

3 The Experimental setup **17**
3.1 The ISOLDE facility 17
3.1.1 Production of radioactive ion beams 17
3.1.2 The ISOLDE facility at CERN 18
3.2 The REX-ISOLDE post-accelerator 19
3.2.1 The Charge Breeding System 19
3.2.2 The REX-LINAC 20
3.3 The MINIBALL γ-spectrometer 21
3.3.1 The MINIBALL HPGe detectors 21
3.3.2 Digital electronics and Pulse Shape Analysis 23
3.4 The MINIBALL setup at REX-ISOLDE 28
3.4.1 The $\Delta E - E$ telescope 29
3.5 Readout electronics and Data acquisition 30

4 Data analysis **35**
4.1 Doppler correction 35
4.2 Calibration of the MINIBALL array 37
4.2.1 Energy calibration with ^{60}Co and ^{152}Eu 37
4.2.2 Efficiency determination at the Full energy peak 38
4.2.3 Cluster position optimization 40
4.2.4 PSA parameter optimization 44

4.3 Calibration of the CD-Si detectors . . . 44
4.3.1 Energy calibration . . . 44
4.3.2 CD azimuth angle optimization . . . 46
4.4 Determination of beam impurities . . . 47
4.4.1 Sources for beam contaminations . . . 47
4.4.2 Methods for determination of beam purity . . . 49
4.5 Determination of Angular Correlation Factors . . . 54

5 Test measurements **57**
5.1 Coulomb excitation of ^{22}Ne at 2.25 MeV/u . . . 57
5.1.1 Event selection and determination of γ-intensities . . . 57
5.1.2 Extraction of the $B(E2)\uparrow$ value . . . 61
5.2 Coulomb excitation of ^{22}Ne at 2.86 MeV/u . . . 61
5.2.1 Extraction of the $B(E2)\uparrow$ value . . . 62
5.2.2 Differential cross section measurement . . . 62
5.2.3 Calibration of ^{107}Ag $E2$ matrix elements . . . 65

6 Analysis and Results **67**
6.1 Coulomb excitation of ^{30}Mg at 2.25 MeV/u . . . 67
6.1.1 Purity of the ^{30}Mg beam . . . 67
6.1.2 Extraction of the $B(E2;\ 0^+_{\text{g.s.}} \rightarrow 2^+_1)$ value . . . 68
6.1.3 Time dependence . . . 73
6.2 Coulomb excitation of ^{30}Mg at 2.69 MeV/u . . . 74
6.2.1 Purity of the ^{30}Mg beam . . . 76
6.2.2 Extraction of the $B(E2;\ 0^+_{\text{g.s.}} \rightarrow 2^+_1)$ value . . . 76
6.2.3 Differential cross section measurement . . . 79
6.2.4 Measurement with a ^{107}Ag target . . . 81
6.3 Coulomb excitation of ^{32}Mg . . . 82
6.3.1 Purity of the ^{32}Mg beam . . . 82
6.3.2 Extraction of the $B(E2;\ 0^+_{\text{g.s.}} \rightarrow 2^+_1)$ value . . . 83

7 Discussion **89**
7.1 The neutron-rich isotopes ^{30}Mg and ^{32}Mg . . . 89
7.1.1 The $B(E2;\ 0^+_{\text{g.s.}} \rightarrow 2^+_1)$ values for ^{30}Mg and ^{32}Mg . . . 89
7.1.2 Comparison with intermediate-energy measurements . . . 91
7.1.3 Comparison with theoretical predictions . . . 92
7.2 Summary . . . 94

A Coulomb excitation **95**
A.1 Excitation cross section . . . 95
A.2 Angular distributions . . . 96

B Rotational model **97**
B.1 Quadrupole moment and Deformation 97
B.2 Quadrupole moment and Reduced matrix element 98

C Electromagnetic transitions and Collectivity **99**
C.1 Emission of electromagnetic radiation 99
C.2 Collectivity of transitions 100

D Coulomb excitation calculations **101**
D.1 Sample CLX calculation 101
D.2 Sample GOSIA calculation 102

E Analysis software **105**
E.1 Data processing 105
E.2 Energy calibration 107
E.3 MINIBALL cluster position optimization 108

List of Figures

1.1 Chart of the nuclides. 2
1.2 Effective single-particle energies for oxygen isotopes and $N = 20$ isotones. . 2
1.3 Excitation energies of the 2_1^+ states of the neutron-rich Si and Mg isotopes. 3
1.4 Comparison of $B(E2)\uparrow$ values for the neutron-rich Mg isotopes ^{30,32,34}Mg measured at intermediate-energy facilities. 4

2.1 Schematical view of the Coulomb excitation process. 8
2.2 Comparision of single and multiple step excitations. 13

3.1 Schematical layout of the ISOLDE facility. 18
3.2 Schematical view of the REX-ISOLDE post-accelerator. 19
3.3 Schematical layout of the REX-LINAC. 21
3.4 Pictures of the REX-ISOLDE accelerator in 2002 and 2004. 22
3.5 Schematical drawing of a MINIBALL crystal. 24
3.6 Picture of a MINIBALL triple cluster. 24
3.7 Picture of the MINIBALL frame. 25
3.8 The steepest-slope method for the determination of the radius r. 26
3.9 The induced charge method for the determination of the angle ϕ. 27
3.10 Schematical view of the MINIBALL setup at REX-ISOLDE. 28
3.11 Schematic structure and picture of the CD-detector. 29
3.12 Picture of the MINIBALL target chamber. 30
3.13 Typical gate widths for the trigger logic of the MINIBALL electronics. . . 31
3.14 Electronics layout for the creation of the DAQ triggers. 32

4.1 Schematic of the kinematical reconstruction. 36
4.2 Sample MINIBALL γ-spectrum of a ^{152}Eu source. 37
4.3 Absolute MINIBALL efficiency for Exp_Sep04 with and without cluster addback. 39
4.4 Definition of the MINIBALL cluster angles Θ_c, ϕ_c and α_c. 40
4.5 Energy loss vs. total energy for a stable ^{22}Ne beam (2.25 MeV/u) impinging on a 10μm PE target. 41
4.6 Cluster position optimization for one sample MINIBALL triple cluster. . . 42
4.7 Resulting γ-spectrum of the MINIBALL cluster position optimization. . . . 43

4.8 Comparison of ^{23}Ne 1017 keV γ-line Doppler correction on core, segment and PSA level. . . . 45
4.9 $E - \Delta E$-Plot showing the result of the CDE-calibration for one sector. . . 46
4.10 Doppler corrected ^{22}Ne 1274.5 keV line for different offset angles $\Delta\Phi_{\mathrm{CD}}$ of the CD-detector. . . . 48
4.11 Result of the CD azimuth angle optimization for Exp_Oct03. . . . 49
4.12 CD-energy vs. Θ_{CD} for Laser on/off-measurements with a 2.69 MeV/u ^{30}Mg impinging on a 1.1 $\frac{\mathrm{mg}}{\mathrm{cm}^2}$ ^{107}Ag target for Exp_Sep04. . . . 50
4.13 Analysis of release curves to determine ^{30}Al contaminants in ^{30}Mg beam for Exp_Oct03. . . . 51
4.14 Analysis of data from thin ΔE-detectors for the determination of the beam composition. . . . 53
4.15 γ-ray efficiency distributions obtained from a GEANT4-simulation of the MINIBALL setup. . . . 55
4.16 γ-ray angular distributions for exited states in ^{32}Mg and ^{107}Ag. . . . 56

5.1 Time difference of γ-rays and particles for the selection of coincident events. 58
5.2 CD-energy vs. Θ_{CD} for a 2.25 MeV/u ^{22}Ne beam impinging on a 1.0 $\frac{\mathrm{mg}}{\mathrm{cm}^2}$ natural Ni target. . . . 59
5.3 γ-spectra relevant for the determination of the $B(E2)\uparrow$ value of ^{22}Ne relative to ^{58,60}Ni. . . . 60
5.4 CD-energy vs. Θ_{CD} for a 2.86 MeV/u ^{22}Ne beam impinging on a 1.1 $\frac{\mathrm{mg}}{\mathrm{cm}^2}$ ^{107}Ag target. . . . 63
5.5 γ-spectra relevant for the determination of the $B(E2)\uparrow$ value of ^{22}Ne relative to ^{107}Ag. . . . 63
5.6 Low-energy part of the level scheme of ^{107}Ag. . . . 64
5.7 Differential cross section $\left(\frac{d\sigma}{d\Omega}\right)_{\mathrm{cm}}$ for the Coulomb excitation of 2.86 MeV/u ^{22}Ne projectiles on a ^{107}Ag target. . . . 65

6.1 Random-subtracted γ-spectra showing the Coulomb excitation of the 244 keV state in ^{30}Al for Exp_Oct03. . . . 69
6.2 CD-energy vs. Θ_{CD} for the 2.25 MeV/u ^{30}Mg beam impinging on a 1.0 $\frac{\mathrm{mg}}{\mathrm{cm}^2}$ natural Ni target. . . . 70
6.3 Doppler corrected γ-spectra for the 2.25 MeV/u ^{30}Mg incident on a 1.0 $\frac{\mathrm{mg}}{\mathrm{cm}^2}$ natural Ni target. . . . 70
6.4 Spectra with fits for the determination of the γ-yields for the Mg and Ni transitions. . . . 72
6.5 ^{30}Mg $B(E2)\uparrow$ value dependence on the time T_{p} since the last T1 proton pulse. 74
6.6 Time structure of the beam pulse extracted from the EBIS for the ^{30}Mg beam of Exp_Oct03. . . . 75
6.7 ^{30}Mg $B(E2)\uparrow$ value dependence on the time after the EBIS pulse. . . . 75
6.8 CD-energy vs. Θ_{CD} for a 2.69 MeV/u ^{30}Mg beam impinging on an isotopically enriched ^{60}Ni target. . . . 77

6.9 Doppler corrected γ-spectra for 2.69 MeV/u ^{30}Mg incident on the 3.85 $\frac{\text{mg}}{\text{cm}^2}$ ^{60}Ni target. 78
6.10 Fit to determine the peak area of the ^{60}Ni 1332.5 keV transition γ-ray. . . 79
6.11 Differential cross section $\left(\frac{d\sigma}{d\Omega}\right)_{\text{cm}}$ for Coulomb excitation of 2.69 MeV/u ^{30}Mg projectiles on a ^{60}Ni target. 80
6.12 γ-spectra for a 2.69 MeV/u ^{30}Mg beam incident on a 4.4 $\frac{\text{mg}}{\text{cm}^2}$ ^{107}Ag target. 81
6.13 CD-energy vs. Θ_{CD} for the 2.84 MeV/u ^{32}Mg beam impinging on a 4.4 $\frac{\text{mg}}{\text{cm}^2}$ ^{107}Ag target. 83
6.14 Mg-Doppler corrected γ-spectra for the 2.84 MeV/u ^{30}Mg incident on the 4.4 $\frac{\text{mg}}{\text{cm}^2}$ ^{107}Ag target. 85
6.15 Doppler corrected γ-spectra for the 2.84 MeV/u ^{32}Mg Coulomb excitation experiment. 85

7.1 $B(E2)\uparrow$ values for ^{30,32}Mg of the present work compared to intermediate-energy measurements and theoretical predictions. 91
7.2 Differential cross section for 32 MeV/u ^{24}Mg impinging on a ^{208}Pb or a ^{12}C target showing Coulomb and nuclear contributions to the excitation. 93
7.3 $B(E2)\uparrow$ values determined in the present work for ^{30}Mg and ^{32}Mg compared to different theoretical predictions. 93

List of Tables

2.1 Comparison of low-energy and high-energy Coulomb excitation. 13

4.1 Energy resolution of MINIBALL array at ^{60}Co energies for Exp_Oct03. . . 38
4.2 Energies and intensities of used γ-ray calibration sources ^{60}Co and ^{152}Eu. . 39
4.3 Relative angular correlation factors $\frac{W_\gamma^t}{W_\gamma^p}$ for the Coulomb excitation experiments of Exp_Sep04. 56

5.1 Summary of determined ^{22}Ne $B(E2)\uparrow$ values from the test measurements. . 64
5.2 ^{107}Ag $B(E2)\uparrow$ values for the $\frac{1}{2}^-_{\text{g.s.}} \rightarrow \frac{3}{2}^-_1$ and $\frac{1}{2}^-_{\text{g.s.}} \rightarrow \frac{5}{2}^-_1$ transitions. 66

6.1 Amount of ^{30}Al in the ^{30}Mg beam deduced from different methods for Exp_Oct03 ($0 \leq T_{\text{p}} \leq 1.2\,\text{s}$). 68
6.2 Amount of ^{30}Al in the ^{30}Mg beam deduced from different methods for Exp_Sep04. 76
6.3 Contributions of ^{32}Al and ^{32}Si in the ^{32}Mg beam for Exp_Sep04. 82
6.4 Summary and error budget for the ^{32}Mg $B(E2)\uparrow$ value. 87

7.1 Summary of the $B(E2;\ 0^+_{\text{g.s.}} \rightarrow 2^+_1)$ values of ^{30}Mg and ^{32}Mg in the present work. 90
7.2 Influence of quadrupole moment on deduced $B(E2)\uparrow$ values for ^{30}Mg and ^{32}Mg. 90
7.3 Half lifes and quadrupole deformation parameters for ^{30}Mg and ^{32}Mg derived from the determined $B(E2)\uparrow$ values. 94

D.1 Sample CLX input file with description of parameters. 101
D.2 Sample GOSIA input file with description of parameters. 103

E.1 Description of most important analysis code files. 106

Chapter 1

Introduction

Nuclear structure physics is the science dealing with the atomic nucleus, its composition and its properties. The goal of nuclear structure physics is the examination and understanding of the structure of the nucleus and the interaction between its constituents, the nucleons.

The atomic nucleus is a many-body system consisting of A nucleons: Z protons and N neutrons. All nuclei expected to be bound are gathered in the nuclear chart displayed in figure 1.1. Only 270 of the about 2700 isotopes, which are known so far, are stable with respect to radioactive decay; they form the so-called *valley of stability*. When leaving this region and approaching the proton and neutron drip lines, the nuclei are characterized by extreme N/Z-ratios. The knowledge on these so-called *exotic* nuclei is limited and the experimental data, especially on the neutron-rich side, are sparse.

The double black horizontal and vertical lines in figure 1.1 indicate the magic numbers which were first predicted by the shell model of Mayer and Jensen in 1949 [1, 2]. These magic numbers are 2, 8, 20, 28, 50, 82 and 126. Nuclei with magic proton and/or neutron numbers, corresponding to a closed proton/neutron shell, were found to be very stable and are characterized by strong binding and large 2_1^+ excitation energies in case of even-even nuclei (see also the Si isotopes in figure 1.3). Although the lines indicating the magic numbers in figure 1.1 are plotted well beyond the valley of stability, recent experimental and theoretical developments indicate that these numbers are only valid for nuclei in the vicinity of the stable isotopes and new magic numbers may appear when going to more exotic nuclei.

A possible explanation for the occurrence of new magic numbers is given e.g. in [3]. In figure 1.2 the effective single particle energies for the oxygen isotopes with $N = 8 - 20$ (a) and $N = 20$ isotones with proton numbers $Z = 8 - 20$ (b) are shown. For an *occupied* orbit the effective single-particle energy (ESPE) is defined as the separation energy of the orbit (with opposite sign); if the orbit is *unoccupied* the ESPE is defined as the gain in binding energy when a proton or a neutron is put into this orbit (with opposite sign). From figure 1.2 (b) it is obvious that for the $N = 20$ isotones with proton numbers $Z \geq 14$, due to the gap between the *sd* and *pf* shell, the usual magic number $N = 20$ is valid. For $Z < 14$, however, the energy gap between the two major shells is decreasing resulting in the appearance of the new magic neutron number $N = 16$ at $Z = 8$.

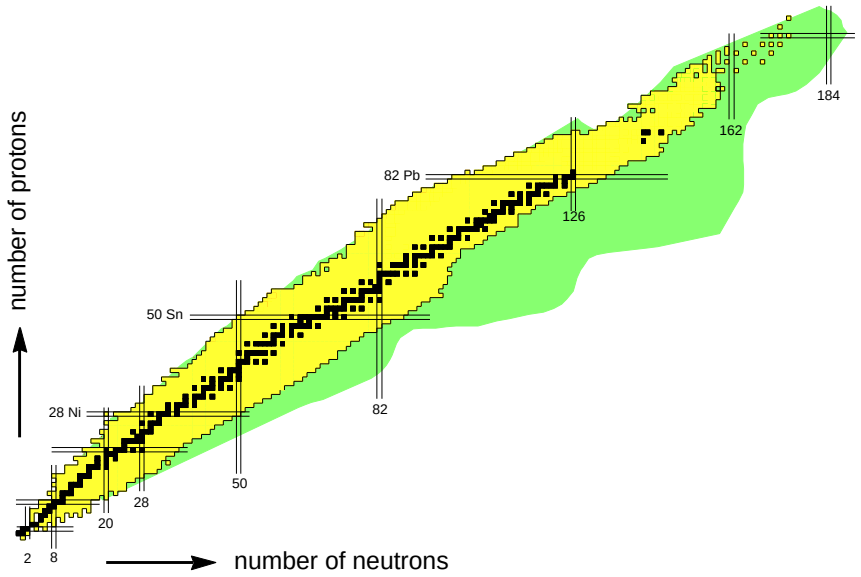

Figure 1.1: Chart of the nuclides. The proton number Z is plotted versus the neutron number N. The stable nuclei are indicated by the black boxes, the yellow area includes all known isotopes. Only the isotopes inside the area marked in green are thought to exist as bound systems.

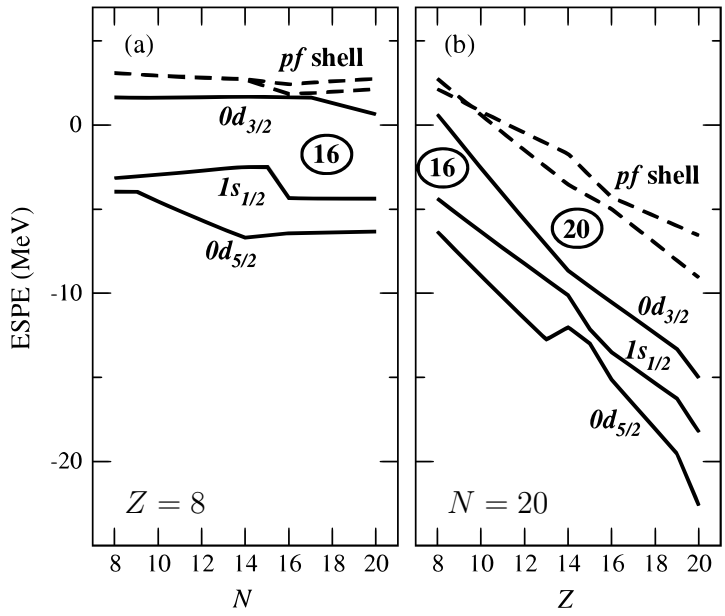

Figure 1.2: Effective single-particle energies of neutrons (a) for the oxygen isotopes ^{16}O to ^{28}O and (b) for the $N = 20$ isotones ^{28}O to ^{40}Ca (from [3]).

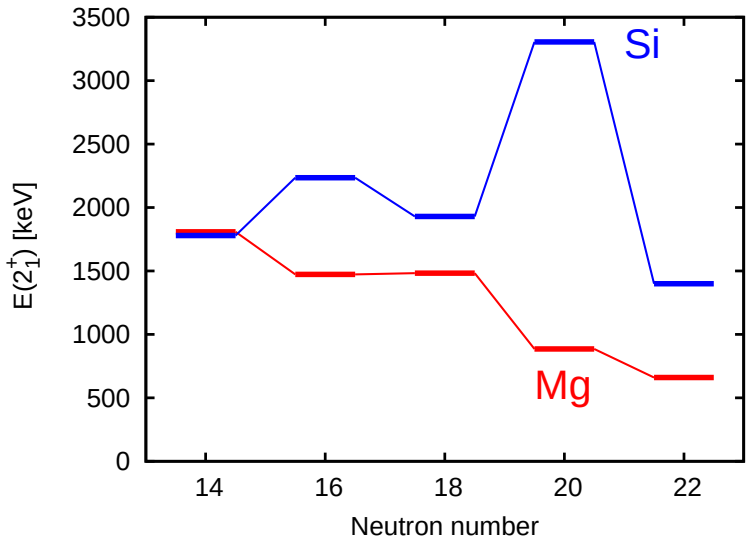

Figure 1.3: Excitation energies of the 2_1^+ states of the neutron-rich Si and Mg isotopes. For Si ($Z = 14$) one can clearly see the $N = 20$ shell closure which is not observable in the case of Mg ($Z = 12$).

Concerning the $N = 20$ Mg isotope ^{32}Mg, no clear conclusion can be drawn from figure 1.2 (b) regarding the magic neutron number. ^{32}Mg is expected to belong to the so-called *island of inversion*. Already in 1975, the mass measurements of Thibault *et al.* [4] for the Na isotopes ^{31,32}Na showed deviations from the expectations for a closed neutron shell at $N = 20$. The unusual large masses and the increase in the two-neutron separation energy S_{2n} for these isotopes was explained in 1975 by Campi *et al.* [5] who proposed the exotic Na nuclei to be deformed due to the filling of the $1f_{7/2}$ orbital intruding in the *sd* shell.

In 1990, Warburton *et al.* [6] predicted the *island of inversion* (the denotation was first introduced by Wildenthal *et al.* in 1980 [7]) to consist of the neutron-rich isotopes ^{30,31,32}Ne, ^{31,32,33}Na and ^{32,33,34}Mg, i.e. of the nuclei with $Z = 10-12$ and $N = 20-22$. In a recent β-decay measurement [8], however, the ground state spin and parity of ^{31}Mg were determined to be $J^\pi = 1/2^+$ and the magnetic moment of ^{31}Mg was measured. Comparisons of the obtained results with shell model calculations suggested the $1/2^+$ ground state to be a pure $2p-2h$ intruder state which would assign ^{31}Mg to belong also to the *island of inversion* and therefore expand this region to the nucleus with $Z = 12$ and $N = 19$.

The anomalous behavior of the neutron-rich Mg isotopes is also illustrated in figure 1.3 where the excitation energies of the first 2^+ states are shown for the neutron-rich even-even Mg and Si isotopes. The high excitation energy of the $N = 20$ nucleus ^{34}Si shows a strong shell effect for $Z = 14$, whereas for the Mg isotopes with $Z = 12$ the low excitation energy of ^{32}Mg points to a complete vanishing of the $N = 20$ neutron shell closure for $Z = 12$.

The first $B(E2)\uparrow$ value for an *island of inversion* nucleus was determined in 1995 by Motobayashi *et al.* [9] for ^{32}Mg using the new technique of intermediate-energy Coulomb excitation; a large $B(E2)\uparrow$ value of 454 (78) e^2fm^4 was measured which was much larger

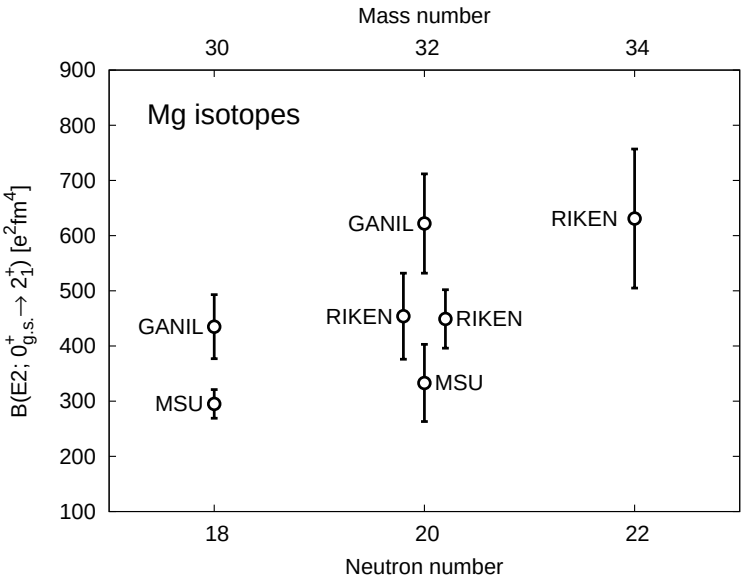

Figure 1.4: Comparison of $B(E2)\uparrow$ values for the neutron-rich Mg isotopes ^{30,32,34}Mg measured at intermediate-energy facilities (data from [9–12]).

than expected for a semi-magic nucleus. Although several other experiments have been performed for neutron-rich nuclei in the vicinity of the *island of inversion*, some of the results are not yet consistent, even 30 years after the discovery of Thibault *et al.*. As an example the $B(E2)$ values for the neutron-rich Mg isotopes ^{30,32,34}Mg measured by different groups at the intermediate-energy facilities MSU [10], RIKEN [9, 11] and GANIL [12] are displayed in figure 1.4. It is obvious that these measurements show some inconsistencies, as e.g. the ^{32}Mg $B(E2)\uparrow$ values measured at MSU and GANIL deviate by a factor of 2. Regarding the boundaries of the *island of inversion*, no conclusion can be drawn from the existing experimental data, and also the various theoretical model predictions [13–21] (which are not displayed) cannot be distinguished.

In order to clarify this situation an experimental program was started with the aim to measure $B(E2)\uparrow$ values in the vicinity of the *island of inversion* employing the standard nuclear physics technique of sub-barrier Coulomb excitation in inverse kinematics. In order to perform such "safe" Coulomb excitation experiments as well as other standard techniques (as e.g. nucleon-transfer reactions), the **R**adioactive beam **EX**periment REX [22] for the post-acceleration of radiaoctive beams, located at the ISOLDE facility [23] at CERN, is ideally suited. With the REX-ISOLDE accelerator the feasibility of a novel technique to bunch, charge breed and post-accelerate radioactive ions provided by an ISOL[1] facility is demonstrated. The maximum beam energy which is currently achievable with the REX-ISOLDE accelerator is 3.0 MeV/u.

Due to the rather low intensities of the radioactive ion beams it is important to detect

[1] **I**sotope **S**eparation **O**n-**L**ine

de-excitation γ-rays originating from nuclear reactions with high efficiency and large solid angle coverage. In addition, the radioactive beam experiments are performed in inverse kinematics, i.e. beams of the investigated nuclei are used since no targets from these radioactive ions can be produced. This inverse reaction kinematics results in large recoil velocities of the decaying nuclei of up to 8 % of the speed of light (corresponding to a beam energy of 3.0 MeV/u) and thus in large Doppler shifts. To keep the Doppler broadening small and correct for the Doppler shifts the solid angle covered by the Ge detectors should be small enough to achieve a good angular resolution. All these requirements are fulfilled by the modern HPGe γ-spectrometer MINIBALL [24]. In addition to the electronic segmentation of the Ge crystals, the use of pulse shape analysis (PSA) algorithms [25] allows to determine the interaction points of the impinging γ-rays resulting in an about 100-fold increased granularity compared to a non-segmented detector.

The aim of this thesis was to perform the first "safe" sub-barrier Coulomb excitation experiments with the neutron-rich isotopes ^{30}Mg and ^{32}Mg at the REX-ISOLDE accelerator in conjunction with the MINIBALL γ-spectrometer, and to extract the ^{30,32}Mg reduced transition probabilities $B(E2)$ for the transitions from the 0^+ ground states to the first excited 2^+ states.

In chapter 2 the theory of low-energy Coulomb excitation will be presented. The experimental setup for the Coulomb excitation experiments is described in chapter 3 including the ISOLDE facility, the REX-ISOLDE accelerator and the MINIBALL array. In chapter 4 the technical procedures necessary for the analysis of the Coulomb excitation experiments are outlined. Test measurements with stable beams are summarized in chapter 5. In chapter 6 the analysis and the results of the Coulomb excitation experiments with the neutron-rich Mg isotopes ^{30}Mg and ^{32}Mg are presented. The obtained results are discussed in chapter 7 and a summary of the presented work is given.

Chapter 2

Low-energy Coulomb excitation

Coulomb excitation is the excitation of a projectile (target) nucleus by the electromagnetic field of the target (projectile). For pure Coulomb excitation the excitation cross section can be expressed by the same electromagnetic multipole matrix elements characterizing the electromagnetic decay of the involved nuclear states. A determination of the Coulomb excitation cross section thus allows to study the electromagnetic properties of low-lying nuclear states and extract fundamental nuclear structure information.

The theory of Coulomb excitation is discussed extensively in [26, 27]. There are two different approaches: the semiclassical and the fully quantum-mechanical. In the semiclassical approach the projectile is assumed to move on a classical trajectory which is not affected by the energy loss during the excitation process. In the fully quantum-mechanical approach the whole process is treated quantum-mechanically. In the following an overview of the semiclassical theory of Coulomb excitation is presented since this approach is also used in the coupled-channel codes for the determination of the theoretical Coulomb excitation cross sections. Although first order perturbation theory is not strictly applicable for low-energy Coulomb excitation experiments between heavy nuclei (see section 2.3), this approximation is outlined here since it leads to comprehensive expressions for the excitation amplitudes and cross sections. The analysis of the present data, however, is performed with the coupled-channel codes CLX [28] and GOSIA [29].

2.1 Excitation cross section

The Coulomb excitation process for projectile excitation is shown schematically in figure 2.1 [1]. In the semi-classical theory of Coulomb excitation where the projectile is assumed to move on a classical Rutherford trajectory the differential Coulomb excitation (CE) cross section is given by

$$\left(\frac{d\sigma}{d\Omega}\right) = \left(\frac{d\sigma}{d\Omega}\right)_{\text{Ruth}} P_{i\to f} \ , \tag{2.1}$$

[1] In the following projectile excitation will be considered. By exchanging target and projectile properties (i.e. $Z_p \leftrightarrow Z_t$, ...) target excitations can be considered accordingly.

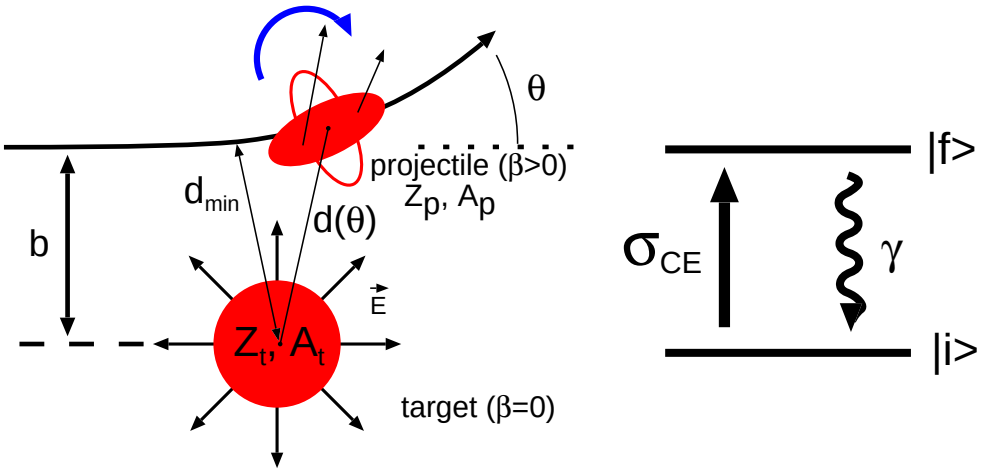

Figure 2.1: Schematic view of the Coulomb excitation process. (a) The projectile nucleus (which in this picture is statically deformed) can be excited in the electric field of the target. The arrows on the projectile indicate the acting force vectors. The torque which is generated because of the orientation of the projectile induces excitations. (b) Schematic of the first-order excitation of the projectile from the initial state $|i\rangle$ to the final state $|f\rangle$ with the subsequent emission of a de-excitation γ-ray.

where $P_{i\to f}$ is the probability to excite the final state $|f\rangle$ from the initial state $|i\rangle$ in a collision in which the projectile is scattered into the solid angle $d\Omega$, and the Rutherford cross section is given by

$$\left(\frac{d\sigma}{d\Omega}\right)_{\text{Ruth}} = \left(\frac{a_0}{2}\right)^2 \frac{1}{\sin^4\left(\frac{\Theta_{\text{cm}}}{2}\right)} \tag{2.2}$$

with Θ_{cm} being the center-of-mass deflection angle and $2a_0$ the distance of closest approach in a head-on collision:

$$a_0 = \frac{Z_p Z_t e^2}{m_0 v^2} \,. \tag{2.3}$$

In equation 2.3 m_0 denotes the reduced mass of the two nuclei with charge numbers Z_p (projectile) and Z_t (target), and v is the relative velocity at large distances. The quantity $\frac{1}{2}m_0v^2$ gives the kinetic energy in the center-of-mass (cm) system which can be expressed as

$$E_{cm} = \frac{A_t}{A_p + A_t} E_{lab} \tag{2.4}$$

with E_{lab} being the projectile kinetic energy.

2.2 First order perturbation theory

The electromagnetic interaction between the projectile and the target is described by the time-dependent interaction potential $V(\vec{r}(t))$. When treating this potential as time-dependent perturbation, the excitation amplitude $a_{i\to f}$ is given by

$$a_{i\to f} = \frac{1}{i\hbar}\int_{-\infty}^{\infty} e^{i\omega_{fi}t}\langle f|V(\vec{r}(t))|i\rangle dt \tag{2.5}$$

with $\omega_{fi} = (E_f - E_i)/\hbar$ and E_i and E_f being the energies of the initial and final states, respectively. The Coulomb excitation probability is then obtained as

$$P_{i\to f} = |a_{i\to f}|^2 \, . \tag{2.6}$$

In order to evaluate the matrix element in 2.5 and thus determine differential and absolute cross sections a multipole expansion of the electromagnetic potential $V(\vec{r}(t))$ has to be performed [26]. As $V(\vec{r}(t))$ has both an electrostatic and a magnetic part the projectile Coulomb excitation cross sections caused by the electric and magnetic fields of the target have to be considered separately.

With the multipole expansion of the electrostatic part of $V(\vec{r}(t))$ the total CE cross section of order $E\lambda$ is given by

$$\sigma_{E\lambda} = \left(\frac{Z_t e}{\hbar v}\right)^2 a_0^{-2\lambda+2} B(E\lambda) f_{E\lambda}(\xi) \tag{2.7}$$

with

$$f_{E\lambda}(\xi) = \int_{\Theta_1}^{\Theta_2} \frac{df_{E\lambda}(\Theta,\xi)}{d\Omega} d\Omega \, , \tag{2.8}$$

where in the Coulomb excitation function $f_{E\lambda}(\xi)$ the integration is performed over all scattering directions given by the minimum (Θ_1) and the maximum (Θ_2) particle scattering angles in the cm-system. An explicit form for $f_{E\lambda}(\xi)$ is given in appendix A.1. The *adiabaticity parameter* ξ is described in section 2.3. In equation 2.7 $B(E\lambda)$ is the reduced transition probability associated with a radiative transition of multipole order $E\lambda$. Generally, the reduced transition probabilities for electromagnetic transitions are defined by [30]

$$\begin{aligned} B(\pi\lambda; I_i \to I_f) &= \sum_{\mu M_f} |\langle I_f M_f|\mathcal{M}(\pi\lambda\mu)|I_i M_i\rangle|^2 \\ &= \frac{1}{2I_i+1}|\langle I_f||\mathcal{M}(\pi\lambda)||I_i\rangle|^2 \end{aligned} \tag{2.9}$$

with I and M being the total angular momentum and the magnetic quantum number of the initial (I_i, M_i) and final (I_f, M_f) states, $\mathcal{M}(\pi\lambda\mu)$ the multipole operator and

$\langle I_f||\mathcal{M}(\pi\lambda)||I_i\rangle$ the reduced matrix element of the corresponding transition. The quantity μ gives the angular momentum transfer along the beam direction, i.e. $\mu = M_i - M_f$. For electric transitions π is given by $\pi = E$, for magnetic transitions by $\pi = M$.

Similar to the excitation caused by the electric field the total CE cross section caused by the magnetic field of the target can be determined to be

$$\sigma_{M\lambda} = \left(\frac{Z_t e}{\hbar c}\right)^2 a_0^{-2\lambda+2} B(M\lambda) f_{M\lambda}(\xi) \tag{2.10}$$

with $f_{M\lambda}(\xi)$ defined analog to 2.8 (see appendix A.1 for the definition of $f_{M\lambda}(\xi)$). When comparing equations 2.7 and 2.10 it stands out that, apart from differences in the nuclear matrix elements and the excitation functions, magnetic excitations are suppressed by a factor of $(\frac{v}{c})^2$ compared to electric excitations. Due to maximum β values of $(\frac{v}{c}) \approx 0.08$ and therefore $(\frac{v}{c})^2 \approx 0.006$ (corresponding to the maximum REX-ISOLDE beam energy of 3.0 MeV/u) the electric excitations are by far dominating the excitation process in the low-energy Coulomb excitation experiments described in this work.

As the electromagnetic excitation involves the same nuclear matrix elements as the radiative transition of corresponding multipole order, the excitation process is subject to the same selection rules as for the emission of electromagnetic radiation (see appendix C.1).

From equations 2.7 and 2.10 it follows that in first order perturbation theory the cross section is directly proportional to the reduced transition probability

$$\sigma_{\pi\lambda} \propto B(\pi\lambda; I_i \rightarrow I_f) \; . \tag{2.11}$$

By measuring the cross section it is therefore possible to extract the $B(\pi\lambda)$ value. In the special case of an electric quadrupole transition ($E2$) from a 0^+ ground state to a first excited 2^+ state the determination of the σ_{E2} cross section allows to determine the $B(E2;\ 0^+_{\text{g.s.}} \rightarrow 2^+_1)$ value for the corresponding transition. From the $B(E2)\uparrow$ value the magnitude of the quadrupole deformation parameter β_2 of the investigated nucleus and the life time of the excited state can be deduced (see appendixes B.1 and C.1).

2.3 Coulomb excitation parameters

In the following, three important parameters governing the Coulomb excitation process are discussed: the *Sommerfeld parameter* η, the *adiabaticity parameter* ξ and the *excitation strength parameter* χ.

Sommerfeld parameter η

The most important parameter concerning the Coulomb excitation process is the *Sommerfeld parameter* η. It compares the de Broglie wave length $\lambda\!\!\!^{-}$ of the relative motion of the two particles with half the distance of closest approach in a head-on collision a_0 which is characteristic for the classical orbit

$$\eta = \frac{a_0}{\lambda\!\!\!^{-}} = \frac{Z_p Z_t e^2}{\hbar v} \; . \tag{2.12}$$

In heavy ion collisions below the Coulomb barrier, usually the condition

$$\eta \gg 1 \tag{2.13}$$

is fulfilled (e.g. $\eta \approx 35$ for ^{30}Mg with an energy of 2.25 MeV/u on ^{60}Ni). The condition 2.13 ensures that the size of a wave packet containing several waves is still small compared to the dimensions of the classical orbit. Since such a wave packet will move along the classical trajectory the semi-classical approach with the classical description for the relative motion of the two nuclei is justified. If condition 2.13 is fulfilled also no penetration through the Coulomb barrier will take place.

Adiabaticity parameter ξ

To excite a final state $|f\rangle$ from the initial state $|i\rangle$ through the time-dependent electromagnetic potential $V(\vec{r}(t))$ the collision time τ_{coll} (which is of the order $\tau_{coll} = \frac{a_0}{v}$) has to be shorter or of the same order of magnitude as the time of the internal motion of the nucleus τ_{nucl} which is given by $\tau_{nucl} = \frac{\hbar}{\Delta E_{if}}$ where ΔE_{if} is the excitation energy difference. The *adiabaticity parameter* ξ is defined as

$$\xi = \frac{\tau_{coll}}{\tau_{nucl}} = \frac{a_0 \Delta E_{if}}{\hbar v} \ . \tag{2.14}$$

For short enough collisions times τ_{coll} the adiabaticity parameter ξ is small and excitations are possible. If the projectile velocities become smaller the projectile is able to follow adiabatically the perturbation caused by $V(\vec{r}(t))$ of the target, and so no excitations can occur. For such adiabatic processes with $\xi > 1$ the excitation probabilities given by the excitation functions $f_{\pi\lambda}$ (cf. equations 2.8 and 2.10) drop exponentially with ξ.

For the low-energy Coulomb excitation experiments described in this work with beam energies of a few MeV/u, the adiabatic cutoff essentially limits the possible excitation energies to below 1 - 2 MeV.

Excitation strength parameter χ

The *excitation strength parameter* χ for a transition of order $\pi\lambda$ from state $|i\rangle$ to $|f\rangle$ is defined by

$$\chi_{\pi\lambda}^{i\to f} = \frac{\sqrt{16\pi} Z_t e}{\hbar g(\pi\lambda)} \frac{(\lambda-1)!}{(2\lambda+1)!!} \frac{\langle I_f || \mathcal{M}(\pi\lambda) || I_i \rangle}{a_0^\lambda \sqrt{2I_i+1}} \tag{2.15}$$

with $g(E\lambda) = v$ and $g(M\lambda) = c$. $\chi_{\pi\lambda}^{i\to f}$ measures the λ-pole strength of the coupling of the states $|i\rangle$ and $|f\rangle$ in a collision of $\Theta = 180°$ and $\xi = 0$. The parameter $\chi_{\pi\lambda}^{i\to f}$ can be estimated by

$$\chi_{\pi\lambda}^{i\to f} \approx \frac{V_\lambda(a_0)\tau_{coll}}{\hbar} \ , \tag{2.16}$$

where $V_\lambda(a_0)$ is the monopole-λ-pole interaction potential which is proportional to $a_0^{-(\lambda+1)}$.

The quantity $\chi_{\pi\lambda}^{i\to f}$ can also be considered as the number of quanta of angular momentum $\lambda\hbar$ which are exchanged during the collision of the two nuclei. For beam energies below the Coulomb barrier one finds for electric quadrupole transitions $\chi_{E2} \leq 10$. By the use of $\chi_{\pi\lambda}^{i\to f}$ it is also possible to formulate a more restrictive condition than 2.13 for the applicability of the semi-classical approach: $\frac{\chi_{\pi\lambda\lambda}}{\eta} \ll 1$.

Due to the possible rather large excitation strengths in sub-barrier Coulomb excitation, multi step excitations are possible (see section 2.5). In such cases with excitation strengths of the order $\chi(\Theta) \gtrsim 1$, the treatment of the excitation process by first order perturbation theory is not valid any more and the perturbation expansion has to be carried out to high order.

2.4 "Safe" Coulomb excitation

In heavy-ion collisions, the distance $d(\Theta)$ between the centroids of the target and projectile nuclei depends on the scattering angle Θ (see figure 2.1) and is given by

$$d(\Theta) = a_0 \left(1 + \frac{1}{\sin\left(\frac{\Theta}{2}\right)} \right) . \tag{2.17}$$

Increasing the projectile bombarding energy leads to a reduction of the distance between the colliding nuclei (cf. equations 2.3 and 2.4). To ensure that the Coulomb excitation process is "safe" and nuclear contributions to the excitation are negligible, the bombarding energy has to be chosen such that the distance of closest approach, $2a_0$, has to be larger than the sum of the radii of the nuclei plus an additional safety distance Δ_s

$$2a_0 > R_p + R_t + \Delta_s . \tag{2.18}$$

Δ_s, which accounts for the range of the nuclear forces and the surface diffuseness of the nuclear density distribution, can be determined experimentally by comparing measured and theoretically determined Coulomb excitation cross sections at different bombarding energies [31]. When requiring a nuclear contribution to be excitation of $\leq 1\,\%$, Δ_s values of $\Delta_s = 5.0$ - 6.6 fm could be determined where the radii of projectile (R_p) and target (R_t) nuclei were calculated using [32]

$$R_i = 1.28A^{1/3} - 0.76 + 0.8A_i^{-1/3} . \tag{2.19}$$

A different group [33] experimentally determined a value for the separation of the nuclear surfaces of $\Delta_s = 5$ fm when requiring the influence of the nuclear excitation to be $< 0.1\,\%$. The radii of the nuclei were here calculated with $R_i = 1.25A_i^{1/3}$.

2.5 Comparison to high-energy Coulomb excitation

As the beam energies in high-energy (i.e. intermediate-energy and relativistic) experiments are much higher than in low-energy Coulomb excitation, also the range of the parameters

parameter	low-energy	high-energy
η	semi-classical approach valid as $\eta \gg 1$	
ξ	$\Delta E \lesssim 1-2\,\mathrm{MeV}$ for $\xi \lesssim 1$	$\Delta E \lesssim 5-15\mathrm{MeV}$ for $\xi \lesssim 1$
χ	multi step excitation, as $\chi > 1$	single step excitation, as $\chi < 1$

Table 2.1: Comparison of the Coulomb excitation parameters for low-energy and high-energy Coulomb excitation.

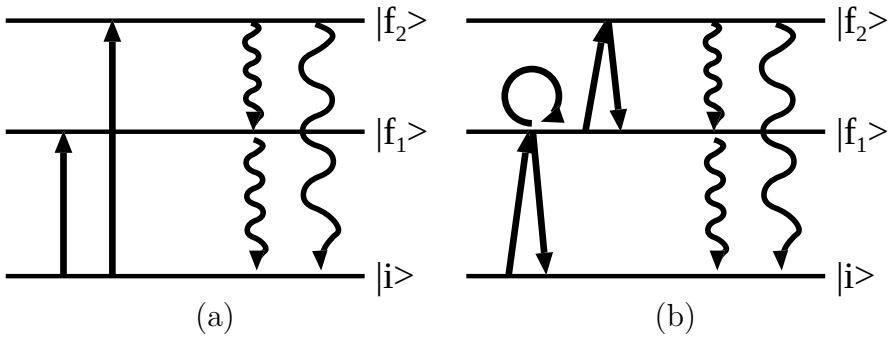

Figure 2.2: Comparision of single (a) and multiple (b) step excitations. The different possible (virtual) excitations are indicated by the black arrows.

describing the Coulomb excitation process is different. In table 2.1 the Coulomb excitation parameters η, ξ and χ are compared for low-energy and high-energy experiments. For both types of experiments the semi-classical approximation is valid since the condition $\eta \gg 1$ is usually fulfilled. In contrast to the low-energy experiments where the excitation energy is limited to $\sim$1 - 2 MeV, excitation energies as large as 5 - 15 MeV can be reached in high-energy measurements. Due to the large velocities and the resulting small collision times τ_{coll} , the excitation strength parameters χ can be much lower at high-energies (cf. equation 2.16) than at low-energies, and therefore restricting the excitation process to single step excitations. In contrast, at low-energies also multi step excitations are possible. Figure 2.2 shows schematically the different possible excitation schemes for single and multi step excitations. In the case of single step excitations the final states $|f_1\rangle$ and $|f_2\rangle$ can only be populated directly in the Coulomb excitation process. For multiple step excitations the final state $|f_1\rangle$ can also be populated by virtual excitations through the intermediate state $|f_2\rangle$. In the Coulomb excitation codes used in the analysis of the present low-energy experiments, multiple step excitations are included since all coupled channels for the different ways of the excitation of a particular nuclear state are considered.

Due to the beam energies below the Coulomb barrier, nuclear contributions to the excitations can be excluded in low-energy measurements. In contrast, at high energies the excitations can also be caused by nuclear excitations or interference of Coulomb and nuclear

forces. Another issue at high-energy measurements is the possible occurrence of feeding from higher-lying states due to the large excitation energies. These effects can influence the deduced results obtained by high-energy Coulomb excitation experiments (see also section 7.1.2).

2.6 Angular distributions

The nuclear states which are populated by Coulomb excitation decay mainly by emission of γ-rays. As in the excitation process the magnetic substates of the excited nuclei are not populated equally, the de-excitation γ-rays have a non-isotropic distribution. The decay by emission of conversion electrons or particles is also possible but strongly suppressed compared to the γ-ray emission probability. A detailed derivation of the γ-ray angular distribution following the Coulomb excitation process can be found e.g. in [26, 27] with final results presented here.

The γ-ray angular distribution is presented for a process where the final state $|f\rangle$ is populated via Coulomb excitation of the initial state $|i\rangle$, and de-excites via γ-emission to the state $|ff\rangle$ which can be identical to $|i\rangle$. In the Coulomb excitation experiments performed in the present work the scattered particles are detected in a ring counter which is symmetric around the beam axis. In this case the γ-ray angular distribution of the de-excitation photons is independent of the azimuth angle ϕ_γ and is given by

$$\begin{aligned} W(\Theta_\gamma) &= \sum_{k\,even, M_i, M_f, L, L'} |a_{i\to f}|^2 \begin{pmatrix} I_f & I_f & k \\ M_f & -M_f & 0 \end{pmatrix} (-1)^{M_f} \\ &\quad \times F_k(L, L', I_{ff}, I_f)\, \sqrt{2k+1}\, P_k(\cos(\Theta_\gamma))\, \delta_L \delta_{L'} \ , \end{aligned} \tag{2.20}$$

where Θ_γ is the angle between the direction of the incident beam and the γ quantum in the rest system of the γ-emitting nuclei, $a_{i\to f}$ is the transition amplitude and $\left(\begin{smallmatrix} I_f & I_f & k \\ M_f & -M_f & 0 \end{smallmatrix}\right)$ the 3j-symbol. In equation 2.20 $F_k(L, L', I_{ff}, I_f)$ are the $\gamma-\gamma$ correlation functions, $P_k(\cos(\Theta_\gamma))$ are the Legendre polynomials and δ_L^2 is the intensity of the 2^L-pole radiation in the γ transition $I_f \to I_{ff}$ (see appendix A.2 for the definitions).

The angular distribution of the emitted γ-rays can be generally written as a sum over even Legendre polynomials

$$W(\Theta_\gamma) = \sum_{k\,even} a_k P_k(\cos(\Theta_\gamma)) \ . \tag{2.21}$$

For the special case of a pure $E2$ transition the angular distribution simplifies to

$$W_{E2}(\Theta_\gamma) = 1 + a_2 P_2(\cos(\Theta_\gamma)) + a_4 P_4(\cos(\Theta_\gamma)) \ . \tag{2.22}$$

2.7 Deorientation effect

Due to hyperfine interactions between the atomic nucleus and the surrounding electron configurations the relative population of the magnetic substates of the interacting nuclear

levels may change. This phenomenon is known as the nuclear deorientation effect. It may cause an attenuation of the observed γ-ray angular distribution which can be accounted for by introducing time-dependent attenuation factors $G_k(t)$ which, in the case of a pure $E2$ transition, lead to the modified angular distribution

$$W_{E2}(\Theta_\gamma, t) = 1 + a_2 G_2(t) P_2(\cos(\Theta_\gamma)) + a_4 G_4(t) P_4(\cos(\Theta_\gamma)) \; . \tag{2.23}$$

The determination of the attenuation factors allows to extract additional information on nuclear quantities (e.g. g-factors) and/or hyperfine fields involved. In the coupled-channel code GOSIA [29] which was used for the determination of the γ-ray angular distributions following the Coulomb excitation process, the nuclear deorientation effects are taken into account.

2.8 Experimental method

The $B(E2; i \rightarrow f)$ values are determined in the present work by measuring the intensity of the γ-transition $f \rightarrow i$ from the populated state $|f\rangle$ to the initial state $|i\rangle$ in coincidence with scattered projectiles or recoiling target nuclei. In the actual setup the particle detector, which has a detection efficiency of 1, is symmetric around the beam axis. The number of γ-rays emitted in the decay of $f \rightarrow i$ into the solid angle element $d\Omega_\gamma$ is then given by

$$dN_\gamma(\Omega_\gamma) = N_\mathrm{b} \cdot n_\mathrm{t} \cdot \sigma_\mathrm{CE} \cdot b_\gamma^{f \rightarrow i} < W(\Theta_\gamma) > d\Omega_\gamma \; , \tag{2.24}$$

where N_b denotes the number of beam particles, n_t the number of target nuclei per unit area and $b_\gamma^{f \rightarrow i}$ is the γ-branching ratio. The Coulomb excitation cross section σ_CE and the angular correlation function $< W(\Theta_\gamma) >$ are given by

$$\sigma_\mathrm{CE} = \int \left(\frac{d\sigma}{d\Omega} \right)_\mathrm{CE} d\Omega \tag{2.25}$$

and

$$< W(\Theta_\gamma) > = \frac{\int \left(\frac{d\sigma}{d\Omega}\right)_\mathrm{CE} \cdot W(\Omega, \Omega_\gamma) \, d\Omega}{\sigma_\mathrm{CE}} \; , \tag{2.26}$$

where the integrals are taken over all cm-angles covered by the particle detector. Note that $\Omega_\gamma = (\Theta_\gamma, \phi_\gamma)$ as well as $< W(\Theta_\gamma) >$ and $dN_\gamma(\Omega_\gamma)$ are defined in a coordinate frame in which the γ-emitting nuclei are at rest. To apply equation 2.24 one therefore has to transform the measured γ-line intensities into the rest frame. While the solid angle transformation $\frac{d\Omega_{\gamma_\mathrm{lab}}}{d\Omega_\gamma}$ can be easily considered on an event-by-event basis during the Doppler shift correction (see section 4.1), the energy and $\Omega_{\gamma_\mathrm{lab}} = (\Theta_{\gamma_\mathrm{lab}}, \phi_{\gamma_\mathrm{lab}})$ dependent efficiency of the γ-detector setup is more cumbersome to take into account. If we assume, for the time being, an isotropic angular correlation function $< W(\Theta_\gamma) > = 1$, the γ-line intensity N_γ deduced from the properly Doppler shifted (and solid angle) corrected γ-spectrum is connected to the Coulomb excitation cross section σ_CE by

$$N_\gamma = N_\mathrm{b} \cdot n_\mathrm{t} \cdot \sigma_\mathrm{CE} \cdot b_\gamma^{f \rightarrow i} \cdot \epsilon_\gamma(< E_\gamma >) \; , \tag{2.27}$$

where $\epsilon_\gamma(<E_\gamma>)$ is the total full energy peak efficiency of the γ-setup

$$\epsilon_\gamma(<E_\gamma>) = \int_{4\pi} \epsilon_\gamma(<E_\gamma>, \Omega_{\gamma_{\rm lab}})\, d\Omega_{\gamma_{\rm lab}} \tag{2.28}$$

and $<E_\gamma>$ the observed average γ-ray energy of the transition in the lab-system; for the MINIBALL setup $<E_\gamma>$ is to a good approximation equal to the transition energy in the rest frame.

Since the angular correlation functions $<W(\Theta_\gamma)>$, averaged over a large Ω range, are only moderately unisotropic and the solid angle covered by the MINIBALL array is large, the effect of the angular correlation on N_γ can be to a good approximation taken into account by replacing equation 2.27 by

$$N_\gamma = N_{\rm b} \cdot n_{\rm t} \cdot \sigma_{\rm CE} \cdot b_\gamma^{f\rightarrow i} \cdot \epsilon_\gamma(<E_\gamma>) \cdot W_\gamma \tag{2.29}$$

with

$$W_\gamma = \frac{\int_{4\pi} <W(\Theta_\gamma)> \cdot \epsilon_\gamma(<E_\gamma>, \Omega_{\gamma_{\rm lab}}(\Omega_\gamma))\, d\Omega_\gamma}{\epsilon_\gamma(<E_\gamma>)} \tag{2.30}$$

using an approximate relation to account for the Doppler shift of the γ-angles $\Theta_{\gamma_{\rm lab}}$,$\phi_{\gamma_{\rm lab}} \rightarrow \Theta_\gamma$,$\phi_\gamma$ (see section 4.5). The Coulomb excitation cross section $\sigma_{\rm CE}$ can therefore be deduced from N_γ by inverting equation 2.29.

In the Coulomb excitation experiments presented in this work both projectile and target excitations can occur. Equation 2.29, which describes the relation between the number of counts in the full energy peak of the γ-line in the properly Doppler shift corrected γ-spectrum and the Coulomb excitation cross section, is valid for projectile and target excitations. As the factor $N_b \cdot n_t$ is common to both projectile and target equations the following relation between the projectile $\sigma^p_{\rm CE}$ and target cross section $\sigma^t_{\rm CE}$ holds:

$$\sigma^p_{\rm CE} = \frac{\epsilon^t_\gamma}{\epsilon^p_\gamma} \cdot \frac{b^{\rm t}_\gamma}{b^{\rm p}_\gamma} \cdot \frac{W^t_\gamma}{W^p_\gamma} \cdot \frac{N^p_\gamma}{N^t_\gamma} \cdot \sigma^t_{\rm CE}\ , \tag{2.31}$$

where $\epsilon^{p,t}_\gamma$, $W^{p,t}_\gamma$ and $N^{p,t}_\gamma$ can be either calculated or extracted from the experiment. Equation 2.31 therefore allows to determine the Coulomb excitation cross section of the projectile (target) relative to the Coulomb excitation cross section of the target (projectile) if the branching ratios $b^{p,t}_\gamma$ are known.

In the analysis of the Coulomb excitation experiments the cross sections are calculated with the coupled-channel codes CLX [28] or GOSIA [29]. To extract e.g. the $B(E2)\uparrow$ value for the projectile, $\sigma^p_{\rm CE}$ is deduced by means of equation 2.31 from the ratio of the measured γ-intensities using the known target matrix elements to calculate $\sigma^t_{\rm CE}$. The projectile cross section is then calculated and the $B(E2)\uparrow$ value is varied until equation 2.31 is fulfilled.

Chapter 3

The Experimental setup

In the following chapter the experimental setup for the Coulomb excitation experiments is described including the ISOLDE facility, the REX-ISOLDE accelerator, the MINIBALL gamma spectrometer as well as additional auxiliary detectors.

3.1 The ISOLDE facility

3.1.1 Production of radioactive ion beams

For the production of radioactive ion beams there are in principle two main production methods: in-flight projectile fragmentation and the Isotope Separation On-Line (ISOL) technique.

In the projectile fragmentation process the primary beam impinges on a light production target where a fraction of the beam particles collide with the target nuclei which leads to fragmentation of the primary ions. By applying a combination of electric and magnetic fields the secondary beam is produced by selecting only the wanted ions and suppressing the contaminants. The energy range of the produced secondary beams at projectile fragmentation facilities ranges from several tens of MeV/u (GANIL in France, MSU in USA, RIKEN in Japan) up to 1 GeV/u (GSI).

In the ISOL approach a high-energy light-ion beam is stopped in a thick production target where the radioactive nuclides are produced by spallation, fission or fragmentation of the target nuclei. These fragments then diffuse out of the target, are ionized by an ion source and subsequently accelerated by a post accelerator. The advantage of the ISOL technique compared to the projectile fragmentation is the good beam quality with small beam spot sizes of the secondary radioactive beams. However, due to the rather slow diffusion process out of the target the ISOL technique can only be applied to nuclei with half-lifes of more than 10 ms whereas the in-flight projectile fragmentation allows to investigate ions with half-lifes of only a few μs.

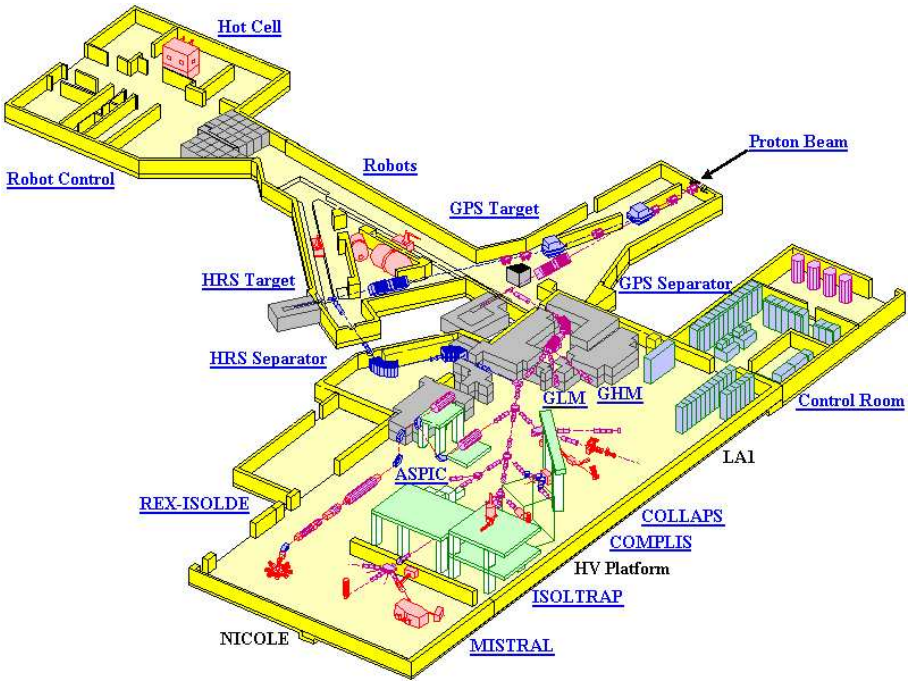

Figure 3.1: Schematical layout of the ISOLDE facility (from [34]).

3.1.2 The ISOLDE facility at CERN

The low-energy Coulomb excitation experiments described in the present work were performed at the ISOLDE facility [23] at CERN. A schematical view of the layout of ISOLDE is shown in figure 3.1.

At ISOLDE the radioactive nuclides are produced in spallation, fragmentation or fission reactions by colliding protons with energies of 1.0 - 1.4 GeV with thick high-temperature targets. For the production of neutron-rich Mg isotopes uranium carbide targets are used. The protons are provided by the CERN PS Booster (PSB) which is a stack of four synchrotrons located on top of each other. The PSB is operated in a so called supercycle with typically 12 pulses and a time distance between consecutive pulses of 1.2 s. The maximum proton beam intensity is 3.2×10^{13} p/pulse. As the PSB is also used by other CERN experiments, not each of the 12 supercycle proton pulses is obligatory available for experiments in the ISOLDE hall resulting in time distances of n·1.2 s for the proton pulses reaching the ISOLDE target.

After the production of the different radioactive nuclei by the bombardment of the ISOLDE targets with the proton beam, the isotopes diffuse out of the target and are subsequently ionized. For the ionization of the neutron-rich Mg isotopes the ISOLDE RILIS (Resonant Ionization Laser Ion Source) [35] was used. The RILIS uses the principle of photo-ionization where excitation and ionization of the atoms can be induced by a resonant interaction with several pulsed laser beams which are tuned to consecutive transitions

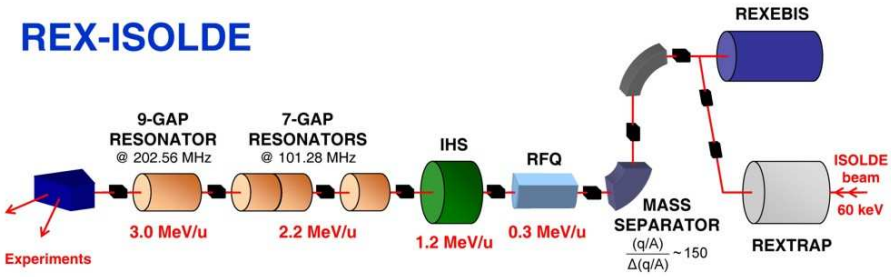

Figure 3.2: Schematical view of the REX-ISOLDE post-accelerator (from [34]).

between atomic states. The probability for the photo-ionization per laser pulse can reach values of up to 10 %. Due to the chemical selectivity of the photo-ionization the isobaric contamination due to surface ionization is suppressed to a large extent. After the ionization of the nuclei the 1^+ ions are extracted and accelerated to 60 keV by an electric field and then guided to the isotope separators.

At the ISOLDE facility there are two different target stations each of them equipped with its own isotope separator. The General Purpose Separator (GPS) and the High Resolution Separator (HRS) can separate different nuclei with a mass resolving power of $\frac{M}{\Delta M} = 2400$ and about 5000, respectively. The beam distribution system of the ISOLDE facility allows to supply almost all experiments located in the ISOLDE hall with ions from either separator.

3.2 The REX-ISOLDE post-accelerator

The **R**adioactive beam **EX**periment (REX) [22, 36, 37] at ISOLDE was initiated as a pilot experiment to demonstrate a new concept for the post-acceleration of radioactive isotopes: the ions are first accumulated, cooled and bunched in a Penning trap (REX-TRAP), then converted to highly charged ions in an electron beam ion source (REX-EBIS) and finally accelerated to energies of up to 3.0 MeV/u in a short linear accelerator (REX-LINAC). Figure 3.2 shows a schematic view of the REX-ISOLDE post-accelerator including TRAP and EBIS.

3.2.1 The Charge Breeding System

The charge breeding system of REX consists of the REX-TRAP, the REX-EBIS and an achromatic A/q-separator. The 60 keV 1^+ ions delivered by ISOLDE are first retarded by the REX-TRAP HV potential of nearly 60 kV to energies of only some eV allowing for the continuous injection of the ions into the trap. The final deceleration of the ions is then achieved in the Ar buffer gas of the trap (with typical gas pressures of about 10^{-3} mbar) where the nuclei are then accumulated and bunched. To improve the transverse emittance

of the extracted beam sideband cooling techniques [38] are employed in addition to the buffer gas cooling. After an accumulation and cooling time of typically 20 ms the ions are extracted from the trap in short bunches, re-accelerated to 60 kV and then injected into the REX-EBIS. The transmission through the REX-TRAP depends on the number of accumulated ions: for intensities of less than 10^5 ions per bunch efficiencies of up to 45 % can be reached, whereas the transmission decreases to about 10 % for 10^7 ions per bunch due to space charge effects.

The REX Electron Beam Ion Source (REX-EBIS) uses monoenergetic electrons with an energy of 5 keV to produce highly charged ions by bombardment of the ions with the electrons. As the REX-EBIS requires a vacuum of better than 10^{-10} mbar the transfer line between the trap and the EBIS is equipped with several differential pumping stages. In the REX-EBIS current densities of about 150 A/cm^2 are reached by compressing the 0.2 A electron beam by the 2 T magnetic field created by a superconducting solenoid. For an operation at 50 Hz (which corresponds to the accumulation and cooling time of the REX-TRAP of 20 ms) the breeding time of the EBIS can be varied between 5 and 19 ms. By varying the breeding time the charge state distribution of the produced ions can be changed which allows to optimize certain A/q-values. Thus it is possible to select the optimal charge state of the wanted ions with $A/q < 4.5$ required by the REX-LINAC. The ion beam extracted from the EBIS has a typical bunch width of $\sim$100 μs at a repetition rate of 50 Hz. The maximum breeding efficiency of the REX-EBIS is about 30 % since only one specific charge state from the total charge state distribution is selected by the subsequent A/q-selector. As the number of positively charged ions that can be stored in the REX-EBIS is about 2×10^{10} per breeding cycle, the EBIS is not limiting the intensity of the REX-ISOLDE post-accelerator.

As the number of bred stable residual gas ions (e.g. C, N, O, Ar and Ne) can be several orders of magnitude higher than that of the wanted radioactive nuclei a mass separation of the beam extracted from the EBIS has to be performed. This is accomplished by an S-shaped separator with a mass resolution of $(A/q)/\Delta(A/q) \approx 100$ - 150 and a transmission of about 75 - 90 %. After passing the A/q-selector the highly charged radioactive ions are injected into the REX-LINAC.

3.2.2 The REX-LINAC

The REX-LINAC post-accelerator consists since 2004 of four different types of resonant structures to meet the requirements of the experiments. The 5 keV/u ions extracted from the EBIS are accelerated to intermediate energies of 1.2 MeV/u by the RFQ and the IH-structure. Subsequently, acceleration or deceleration by the 7-gap resonators to energies between 0.8 MeV/u and 2.25 MeV/u can take place. This energy of 2.25 MeV/u was the maximum beam energy of the REX accelerator from 2001 to 2003. All three structures operate at 101.28 MHz (which is half the frequency of the CERN proton LINAC) and with a duty cycle of 10 %. In 2004 an additional 9-gap IH structure (operating at 202.56 MHz) was installed allowing for a maximum beam energy of 3.0 MeV/u. In figure 3.3 the technical layout of the REX-LINAC is shown. Since the radioactive ions are charge bred to a high

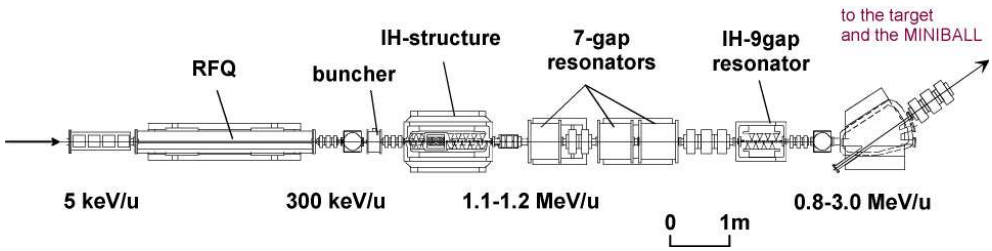

Figure 3.3: Schematical layout of the REX-LINAC. The total length of the accelerator is only 12 m (from [34]).

charge state before acceleration, the linear acceleration is very compact with a total length of only 12 m.

The total transmission through the REX-LINAC is in the order of 80 %. Together with the transmission efficiencies of the REX-TRAP, the REX-EBIS and the A/q-selector an overall efficiency of REX-ISOLDE of $\approx 5\,\%$ is obtained. This overall efficiency is defined by the ratio of the number of ions reaching the target to the number of ions delivered by ISOLDE in front of the REX-TRAP. The energy spread of the REX beam is about 1.5 % at 2.25 MeV/u.

Figure 3.4 shows pictures of the REX-ISOLDE accelerator in 2002 (a) and 2004 (b). The pictures show the accelerating units of the REX-LINAC, a bending magnet which guides the ions in one of the two beam lines, and on the 65° beam line the MINIBALL γ-spectrometer. In the picture of 2004 (b) the open additional 9-gap IH structure can be seen right after the installation still without lead shielding. In addition, a lead wall (orange) can be seen in 2004 which shields the MINIBALL from X-rays originating from the REX accelerator.

3.3 The MINIBALL γ-spectrometer

In the present section the MINIBALL array [24] is introduced. By its large solid angle coverage with an overall full-energy peak efficiency of about 7 % at $E_\gamma = 1.3$ MeV (including cluster addback) and a good Doppler correction performance achieved by the electric segmentation of the Ge crystals and the use of pulse shape analysis (PSA), the MINIBALL spectrometer is tailored for the detection of low-multiplicity γ-cascades from the reactions with radioactive beams.

3.3.1 The MINIBALL HPGe detectors

The MINIBALL γ-spectrometer consists of 24 individually encapsulated HPGe[1] detectors which are electronically 6-fold segmented. In figure 3.5 a MINIBALL crystal is shown

[1] **H**igh **P**urity **Ge**rmanium

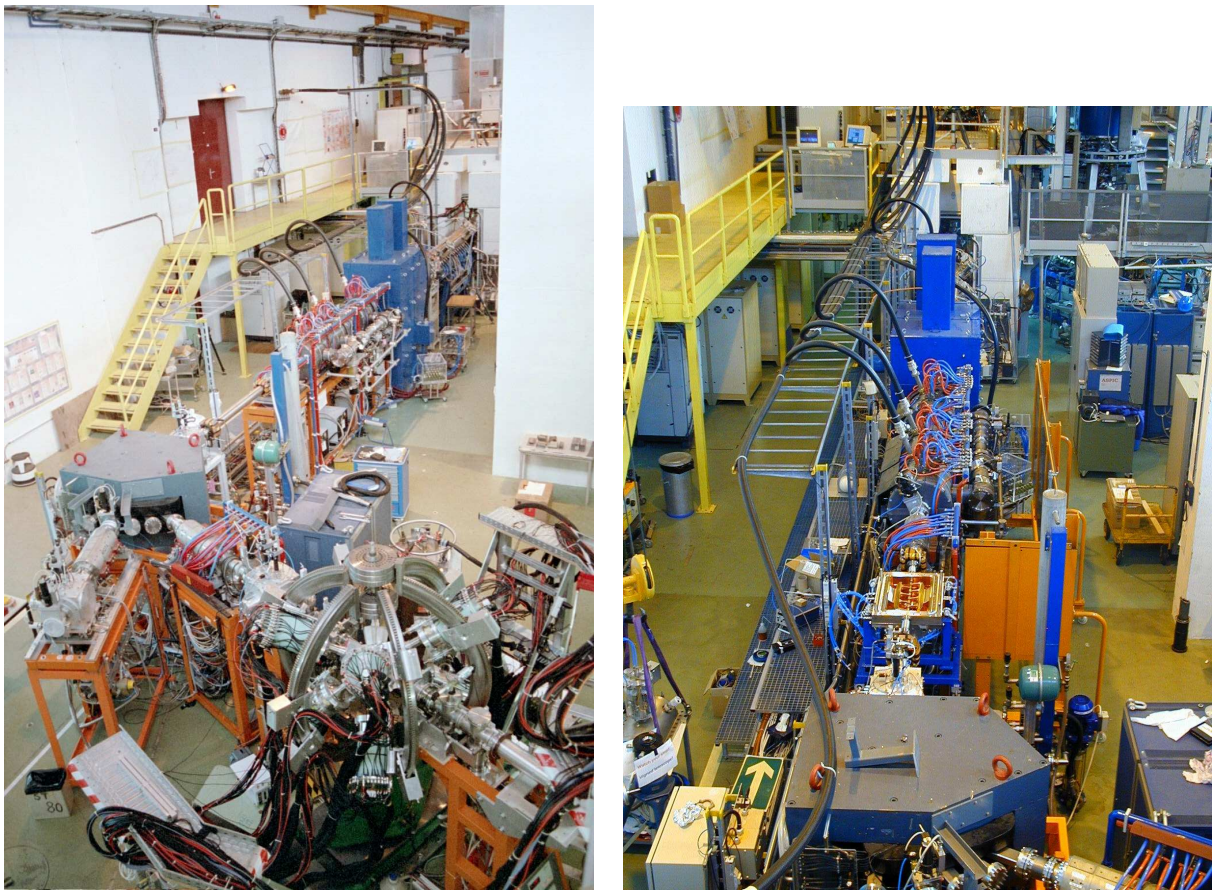

(a) (b)

Figure 3.4: The REX-ISOLDE accelerator in 2002 (a) and 2004 (b). Picture (b) shows the additional 9-gap IH structure which was installed in 2004 for the REX-ISOLDE energy upgrade to 3.0 MeV/u. In the foreground of (a) the MINIBALL γ-spectrometer surrounding the MINIBALL target can be seen.

schematically. The segmentation is accomplished by subdividing the outer contact as shown by the dashed lines in figure 3.5. The HPGe detectors are individually encapsulated (using 0.7 mm thick aluminum casings) and arranged in 8 triple cluster cryostats. In figure 3.6 a picture of a MINIBALL triple cluster is shown. This arrangement of the detectors in triple clusters allows to perform an addback procedure where the individual energies of the three detectors can be added up in case of a γ-ray depositing its energy in more than one detector. The use of the addback procedure results in an increased full energy peak (FEP) efficiency (see section 4.2.2).

Figure 3.7 shows a picture of the MINIBALL frame and a setup consisting of four of the eight MINIBALL triple clusters mounted. The possibility to move the triple clusters along the six arcs, to vary the distance to the target and to rotate the clusters around their axes allows to arrange the clusters in an optimal package with a maximum solid angle covered. As the target chamber has an outer radius of 8.5 cm the MINIBALL detectors can be placed at distances as close as 9 cm to the target position.

3.3.2 Digital electronics and Pulse Shape Analysis

When γ-rays pass through a Ge detector they lose their energy in interactions with the material by photo absorption, Compton-effect or pair production. The created fast electrons (and positrons) then deposit their energy by interacting with the detector material via impact ionization and bremsstrahlung which leads to the creation of a large number of electron-hole pairs in the closest vicinity of the γ-ray interaction point thus allowing to determine the position of the interaction in the crystal. By applying HV to the electrodes of the Ge detector the electrons (holes) drift to the positive (negative) contacts and induce a current signal. The integrated current, the charge, is proportional to the deposited energy which is given by the energy of the γ-ray only for full energy events (FEE).

The readout of the signals of the MINIBALL detectors is performed with digital electronics using XIA DGF-4C modules [41]. The current signals of the central core contact (at positive HV) and the six outer electrodes (at negative HV) are first amplified and integrated by the preamplifiers of the MINIBALL detectors and then fed in the DGF-4C card. The preamplifier charge signals are here digitized by a 12-bit flash ADC[2] with a sampling frequency of 40 MHz corresponding to a sample distance of 25 ns. The digitized charge pulses are then further processed in an FPGA[3] and a DSP[4] which also perform online in real-time the user specific pulse shape analysis (PSA) algorithms.

By the use of the pulse shape analysis which is performed in order to further increase the granularity of the MINIBALL detectors, the r and ϕ coordinates (see figure 3.5) of the main interaction (MI) of the γ-ray in the crystal can be determined on an event-by-event basis. These PSA algorithms are based on the determination of the MI point as an approximation for the first interaction (FI). This assumption was validated by simulations [39] where

[2] **A**nalog to **D**igital **C**onverter
[3] **F**ield **P**rogrammable **G**ate **A**rray
[4] **D**igital **S**ignal **P**rocessor

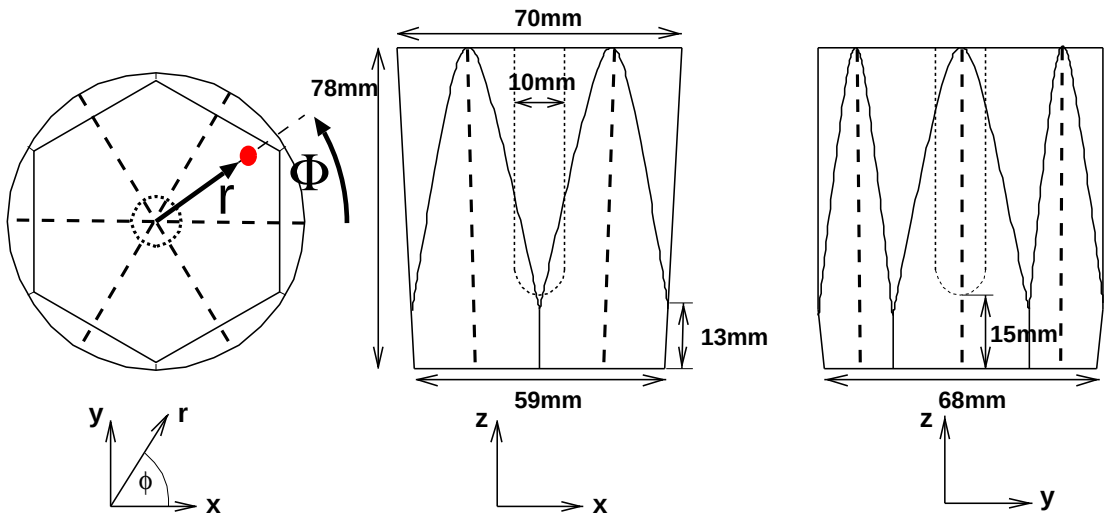

Figure 3.5: Schematical drawing of a MINIBALL HPGe crystal. The dashed lines indicate the electric segmentation of the detector (from [39]).

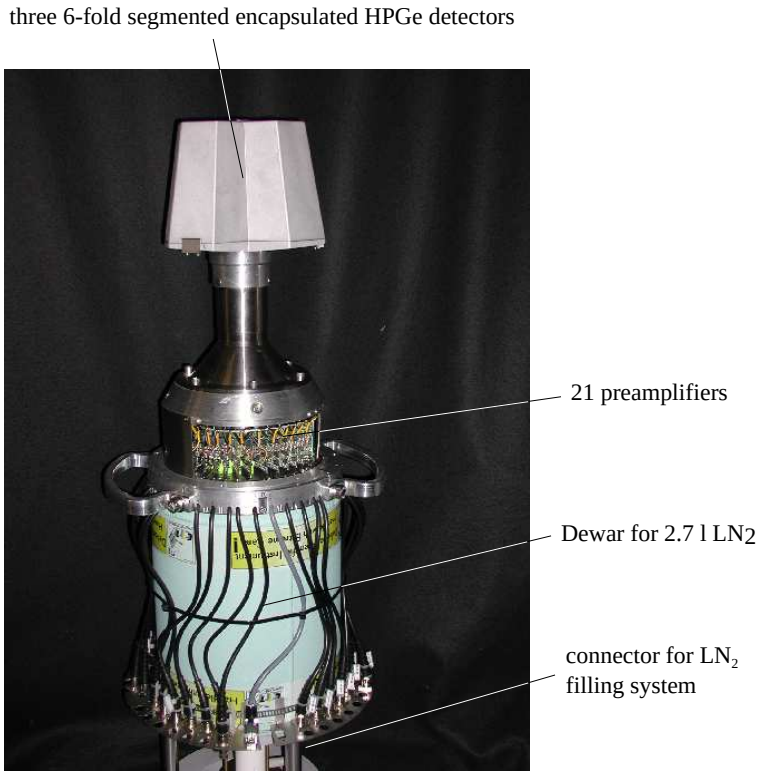

Figure 3.6: Picture of a MINIBALL triple cluster (from [40]).

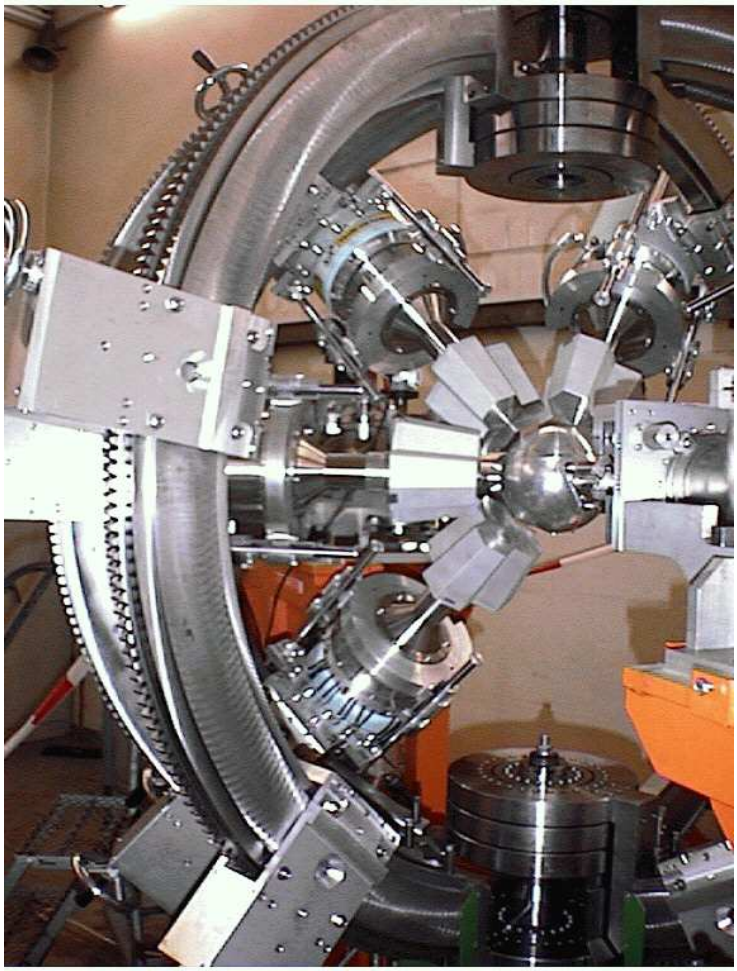

Figure 3.7: Picture of the MINIBALL frame with four (of the eight) triple clusters mounted.

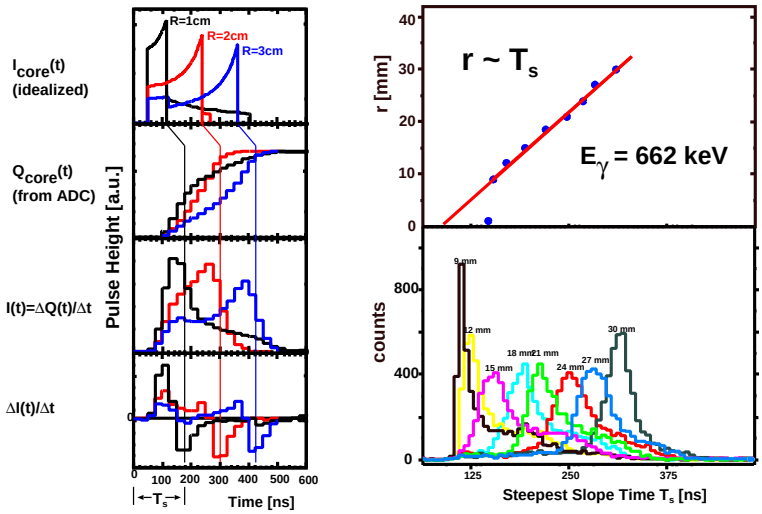

Figure 3.8: The steepest-slope method for the determination of the radius r which is proportional to the drift time of the electrons to the central contact. Left: From the second derivative of the charge pulse $\Delta I(t)/\Delta t$, the time T_s (when the electrons reach the core) can be determined. Right, lower panel: measured steepest-slope times T_s for which a MINIBALL detector was irradiated perpendicular to the surface with 662 keV γ-rays from a collimated source (only FEP events were analyzed). Right, top panel: calibration curve showing the linear dependence of the radius r on the steepest-slope times T_s (from [39, 43]).

it could be shown that the mean transversal distance of the MI from the original γ-ray direction is less than 5 mm for 350 keV γ-rays and decreases for smaller and higher energies.

The steepest-slope method for the determination of the radius r

For the determination of the radial distance r of the MI of the γ-ray the steepest-slope algorithm [42] is used for which the pulse shape of the central contact signal is analyzed. In figure 3.8 a summary of the steepest-slope method is shown. This algorithm is based on the fact that, when the electrons reach the central contact, the main contribution to the detector current signal I_core(t) disappears which leads to a strong drop of the signal at the steepest-slope time T_s (figure 3.8, left). From the second derivative of the charge pulse the time T_s and therefore also the radius r can be determined by

$$r = r_\mathrm{gain} \cdot T_s + r_\mathrm{offset} \ , \tag{3.1}$$

where r_gain and r_offset are the gain and offset values for the r determination which have to be determined experimentally. The radial resolution for a perpendicular irradiation was measured to be about 6 - 8 mm (FWHM) for radii above 12 mm. The steepest-slope method relies on the uniformity of the electron drift velocity in the Ge crystals [39].

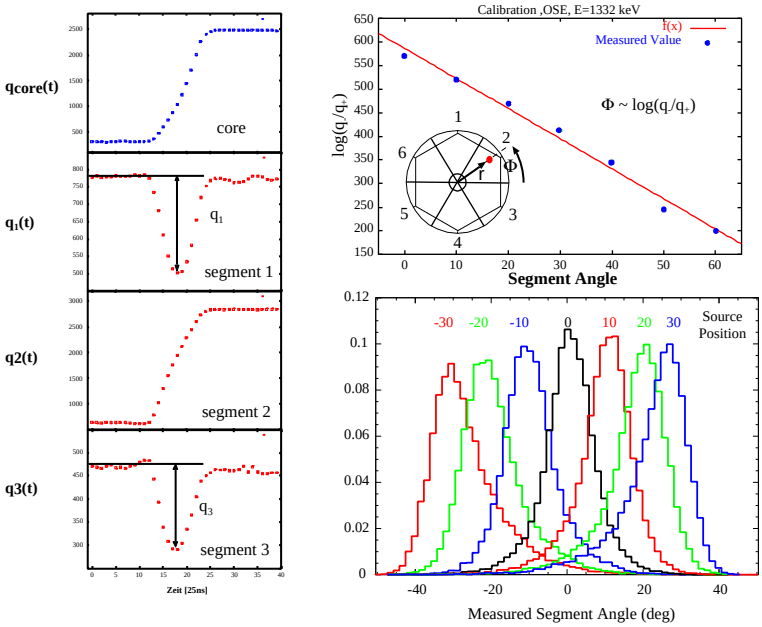

Figure 3.9: The induced charge method for the determination of the angle ϕ. Left: measured charge signals of a 1332 keV γ-ray (one segment event (OSE), full energy deposited in segment 2 (from [44])). In the two neighboring segments 1 and 3, the induced charge signals can be seen. Right, lower panel: measured values $\phi \sim \log\left(\frac{|q_-|}{|q_+|}\right)$ when irradiating a MINIBALL detector with a collimated 662 keV γ-source at various angles ϕ with a fixed radius r of 2.85 cm (from [39]). Right, top panel: calibration curve obtained for 1332 keV γ-rays showing the linear dependence of ϕ from $\log\left(\frac{|q_-|}{|q_+|}\right)$ (from [44]).

The induced charge method for the determination of the angle ϕ

In figure 3.9 a summary of the induced charge method for the determination of the azimuthal angle ϕ is shown. The induced charge method uses pulse form analyses of the two neighboring segments of the hit segment (n) containing the largest energy fraction (segment 2 in 3.9). It could be shown [39] that the inner segment angle ϕ is proportional to $\log\left(\frac{|q_-|}{|q_+|}\right)$ and given by

$$\phi = \phi_{\text{gain}} \cdot \log\left(\frac{|q_-|}{|q_+|}\right) + \phi_{\text{offset}} \ , \tag{3.2}$$

where q_- and q_+ are the heights of the induced charge signals (caused by the drifting of the electrons and holes in segment n) in the two neighboring segments $n-1$ (segment 1 in figure 3.9) and $n+1$ (segment 3 in figure 3.9). The parameters ϕ_{gain} and ϕ_{offset} have to be determined from experiments. With this algorithm for the determination of ϕ an angular resolution of 14° FWHM (for a fixed radius of 2.85 cm) was measured [39].

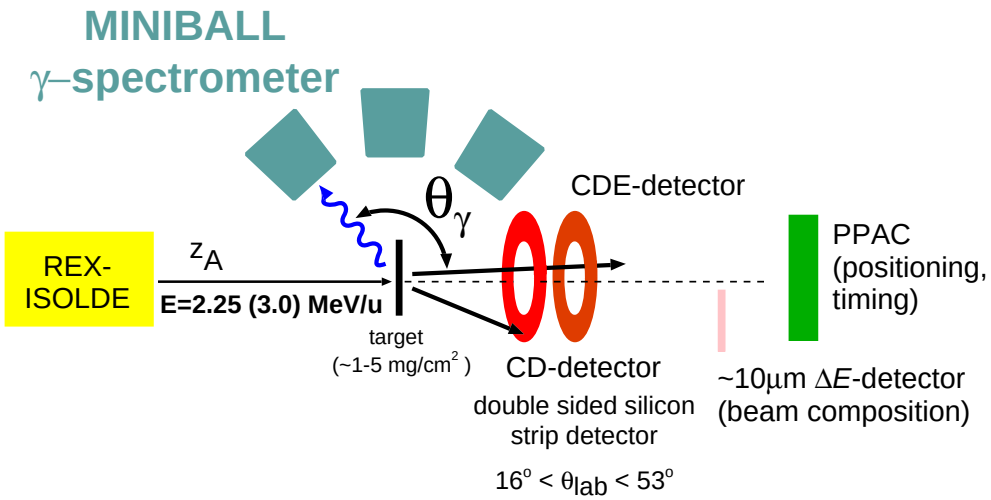

Figure 3.10: Schematical view of the MINIBALL setup at REX-ISOLDE.

The described PSA algorithms that are implemented [25] on the FPGA and DSP of the XIA DGF-4C cards allow to calculate in real time the necessary PSA parameters like the starting times of the signals, the steepest slope times and the induced charges as well as the energies of the core and the segments of the MINIBALL detectors. The parameters are stored for the later off-line analyses (see section 4.2.4 for the achieved energy resolution after Doppler correction using the PSA information).

3.4 The MINIBALL setup at REX-ISOLDE

Figure 3.10 shows a schematic view of the MINIBALL setup for the Coulomb excitation and transfer reaction experiments at the REX-ISOLDE facility at CERN.

The stable or radioactive nuclei provided by REX-ISOLDE with a maximum beam energy of 3.0 MeV/u impinge on a thin (1 - 5 $\frac{\text{mg}}{\text{cm}^2}$) target. In the subsequent reactions both projectile and target nuclei can be excited. The de-excitation γ-rays are detected in the MINIBALL array which is surrounding the target chamber. A $\Delta E - E$ telescope (see section 3.4.1) is used to identify the reaction products and to measure their energy and direction of flight. Under 0° a Parallel Plate Avalanche Counter (PPAC) [45] is used to monitor the beam. The PPAC which can be used up to count rates of 10^9 particles per second has a spatial resolution of 1.6 mm. As the beam is not stopped in the PPAC, little additional γ-ray background from β-decay is produced near the MINIBALL clusters which could affect the measurements. For the determination of the beam composition two 10 μm thick ΔE-detectors (A = 1 cm^2 per detector) were installed in 2004 at a distance of about 15 cm from the MINIBALL target and with an angle of $\Theta \sim 5°$ with respect to the beam direction. They allowed to monitor and identify continuously possible beam contaminants during the experimental campaigns.

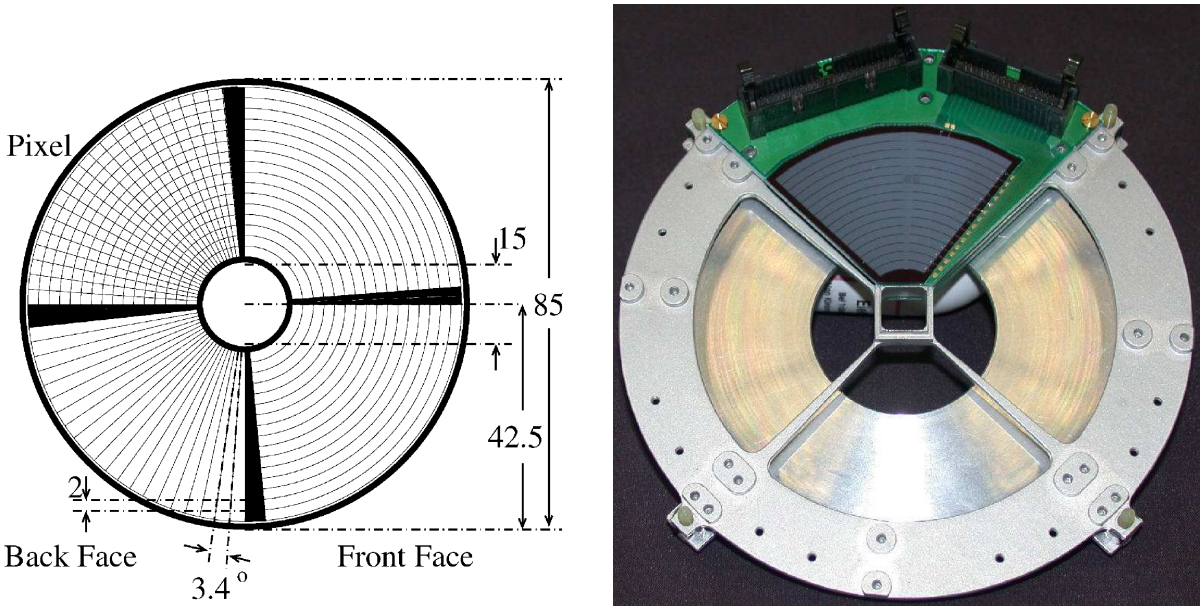

(a) (b)

Figure 3.11: (a) Schematic structure of the CD-detector with 16 annular strips (front side) and 24 sector strips (back side) per quadrant (from [46]). (b) Picture of one of the CD sectors (showing the front side with the annular strips) mounted on a holder (from [34]).

3.4.1 The $\Delta E - E$ telescope

The $\Delta E - E$ telescope used in the target chamber consists of two parts: a double sided silicon strip detector serves as ΔE-detector and an unsegmented silicon detector of the same type is used as E-detector.

The segmented CD-detector [46] consists of four independent quadrants. In figure 3.11 (a) the schematic structure of the CD-detector is shown. Each of the quadrants consists of 16 annular strips (front side) with a width of 1.9 mm and a 2.0 mm pitch and 24 sector strips (back side) with a 3.4° pitch which results in a total of 160 discrete detector elements and 1536 quasi-pixels formed by the overlap of front and rear strips (see figure 3.11 (a), upper left sector). The CD sectors used in the MINIBALL target chamber had thicknesses between 476 μm and 481 μm. The distance between the CD and the target was 30.5 mm resulting in a Θ forward angle coverage from 16.4° to 53.3°. Figure 3.11 (b) shows a picture of one of the CD sectors mounted on a holder. The front side with the 16 annular strips as well as two connectors for the readout of the front and back strips can be seen.

As E-detectors of the $\Delta E - E$ telescope single sided unsegmented Si detectors (CDE) were used being of the same type as the double sided CD-detector. The CDE-detector with its four quadrants and Si wafer thicknesses between 474 μm and 509 μm was installed directly behind the CD in beam direction.

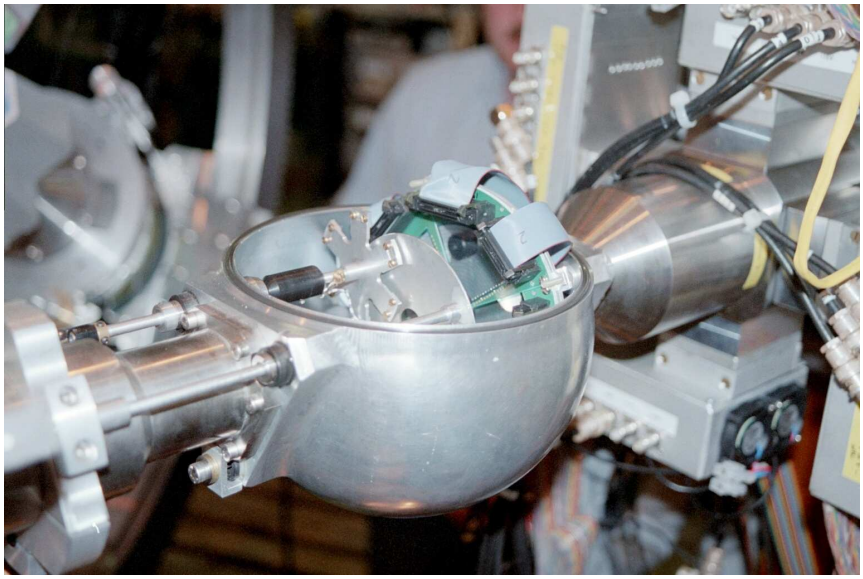

Figure 3.12: Picture of the open MINIBALL target chamber. The beam particles enter the chamber from the left. The target wheel, the CD protection plate and the CD-detector with cabling can be seen.

In figure 3.12 a picture of the open MINIBALL target chamber during the 2002 campaign is shown. The target wheel with its six target positions can be seen allowing to change the targets during the experiments without breaking the vacuum of the beam line and the target chamber. One of the four CD quadrants with two flat cables connected for the readout of the strips is visible. A retractable protection plate in front of the CD is also shown.

In the transfer experiments the use of the $\Delta E - E$ telescope allows to identify the light reaction products (protons, deuterons, tritons) in characteristic $\Delta E - E$ plots (see figure 4.5) due to their specific energy loss in the CD-detector. For the Coulomb excitation experiments the CDE-detector is not needed as the heavy ejectiles and recoil nuclei are stopped in the CD-detector.

3.5 Readout electronics and Data acquisition

The electronics setup of the MINIBALL experiments consisted of a multitude of different units to record all the necessary information for the later offline analysis. A detailed overview of the MINIBALL electronics for the experiments performed in the ISOLDE hall at CERN can be found in [47]; only the most important aspects are discussed here.

As already mentioned in section 3.3.2 the MINIBALL array is readout using the digital XIA DGF4-C modules. For the readout of the CD- and the CDE-detectors, CAEN V785 modules [48] are used. For the timing correlation of the gamma and particle events, an OR

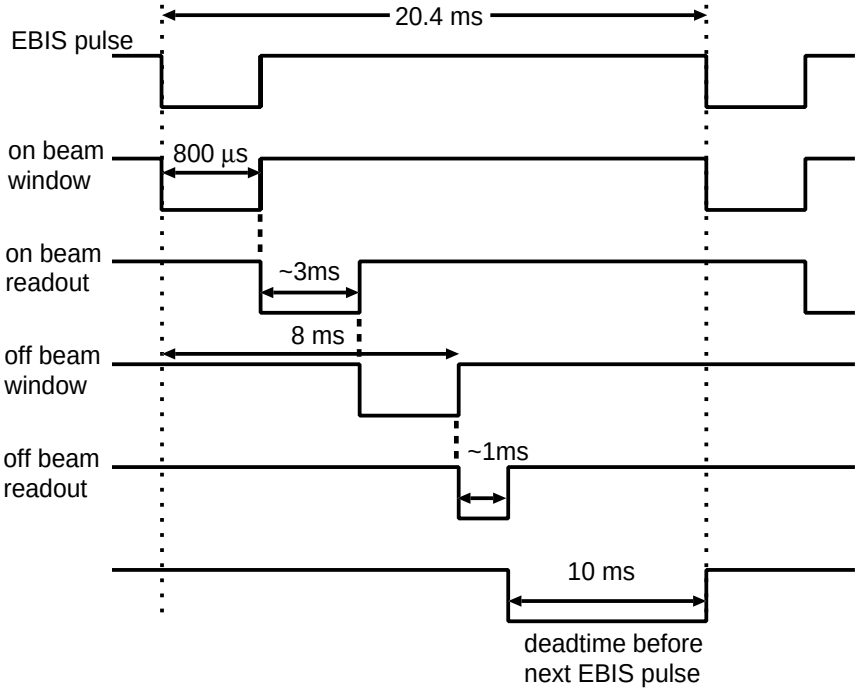

Figure 3.13: Typical gate widths for the trigger logic. During each EBIS cycle, the readout of one ("on beam") or two events ("on beam" and "off beam") is performed.

of all channels of one CD quadrant is fed into an additional DGF module which runs on the same 40 MHz clock as the MINIBALL DGFs. As this is done for all four quadrants, the CD-detector is regarded in the readout as four independent detectors. It is therefore possible to perform an event building and correlate the particle and γ times in the offline analysis. In the event building process all particles and γ-rays within a certain time window are grouped in one physical event. For the analysis of the current experiments a typical time window of 4 μs was chosen (see figure 5.1).

Readout timing

In the setup of the MINIBALL electronics the event readout is aligned to the regular EBIS pulses (see section 3.2.1) with a repetition rate of 49 Hz corresponding to pulse distances of about 20.4 ms. If a readout is initiated the data stored onboard the buffers of the XIA and CAEN modules are read out. While for the CAEN V785 modules, the maximum number of events that can be stored in the buffer is limited by hardware to 32, the maximum number of events for the XIA DGF4-C modules can be set by software (typical values of ≥ 32 were chosen).

In figure 3.13 the timestructure for the readout is shown. With the start of the EBIS pulse signals the on beam window is opened for a typical time of about 800 μs. With the closing of the on beam window a readout is forced which typically takes about 3 ms.

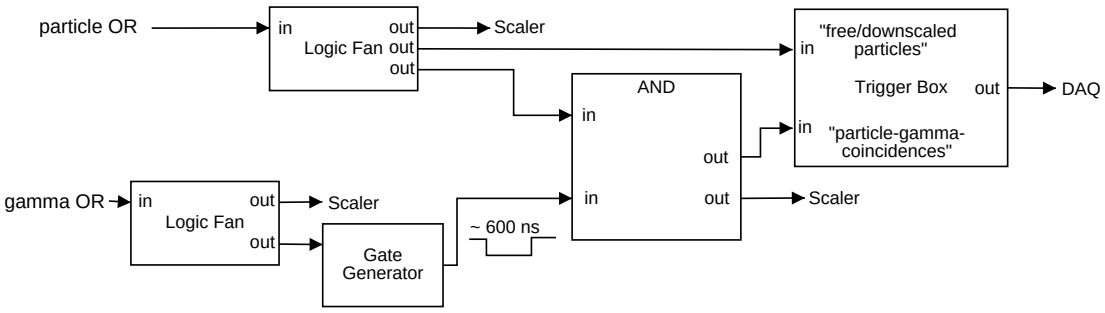

Figure 3.14: Electronics layout for the DAQ trigger generation. The "free/downscaled particles" and "particle-gamma-coincidences" triggers are indicated.

Afterwards the off beam window is opened which is closed again 8 ms after the start of the EBIS pulse. If a trigger is generated during the off beam window a second readout is performed. If additional triggers arrive within a period of 10 ms before the next EBIS pulse they are rejected in order to be ready to acquire data in the next on beam window.

Figure 3.14 shows the basic electronics layout for the creation of the DAQ triggers. With the gamma OR of all channels of the MINIBALL array the hardware coincidence window with a typical length of 600 ns is created (cf. figure 5.1). If a particle OR arrives within this window the "particle-gamma-coincidences" trigger is generated. The use of a trigger box allows to downscale the individual triggers, i.e. in particular the "free/downscaled particles" trigger in case of high beam intensities where the free particle triggers would strongly suppress the rare particle-γ-coincidences. The particle setup of figure 3.14 exists for all four quadrants of the CD with the same common gamma gate resulting in a total of 8 DAQ triggers.

For the CAEN V785 modules, the deadtime after each event (gate signal) is about 10 μs which is needed for the analog to digital conversion process. The deadtime per event for each of the 24 independently running HPGe detectors of the MINIBALL array also amounts to about 10 μs. Due to the method of the relative cross section measurement (see section 2.8) which was applied in the analysis of the Coulomb excitation experiments presented in this work, these deadtimes do *not* have to be considered.

Data Acquisition and Offline Analysis

The data acquisition is performed with the MARaBOU data acquisition system [49] consisting of a front-end system for data readout, event building and data transport and a back-end system for the run control, the online histogramming and the storage of the data. In addition to the online data presentation the MARaBOU system also allows to perform offline analyses.

For the analysis of the experiments described in this work, however, the offline analysis software of [40] based on the data acquisition system [50] used at the MPI-K by the nuclear physics group was further developed and adapted to the special requirements of

the MINIBALL experiments. In the offline analysis the raw MARaBOU data are first read in, then the different analysis steps are performed and the results are finally written to ROOT [51] files and subsequently analyzed. In the analysis process of the Coulomb excitation experiments, in addition to the analysis software itself, also the development of software for the calibration of the MINIBALL spectrometer and the CD-detectors and the optimization of the MINIBALL cluster positions (see next chapter) was carried out resulting in a software package for the analysis of MINIBALL experiments (see appendix E).

Chapter 4

Data analysis

The experiments on the neutron-rich Mg isotopes ^{30}Mg and ^{32}Mg presented in this work were performed during three experimental campaigns at the REX-ISOLDE facility: in July 2003 ("Exp_Jul03"), in October 2003 ("Exp_Oct03") and in September 2004 ("Exp_Sep04"). The procedures outlined in the following chapter (e.g. energy calibrations, efficiency determination, MINIBALL cluster position optimization, beam purity determination), which were developed during the course of the present thesis, were applied to the data from all three experimental campaigns.

4.1 Doppler correction

If an excited nucleus decays in-flight at a velocity of $\beta = \frac{v}{c} > 0$, the energy of the de-excitation γ-ray measured in the laboratory frame will be Doppler shifted. Due to the large projectile velocities of up to 8 % of the speed of light (corresponding to a beam energy of 3.0 MeV/u), these Doppler shifts can become quite large. To correct for the Doppler shift the original energy of the γ-ray E_γ in the rest frame of the emitting nucleus has to be calculated from the laboratory energy E_{lab} according to

$$E_\gamma = \gamma E_{\mathrm{lab}}(1 - \beta \cos(\Theta_{\mathrm{lab}})) \,, \tag{4.1}$$

where Θ_{lab} is the laboratory angle between the direction of the γ-ray and the direction of the emitting nucleus with velocity $\beta = \frac{v}{c}$ and the relativistic factor γ is given by

$$\gamma = \frac{1}{\sqrt{1-\beta^2}} \,. \tag{4.2}$$

In addition to the correction for the measured energies of the γ-rays, also the measured intensities have to be corrected. To obtain the γ-intensity in the rest frame of the γ-emitting nuclei from the measured laboratory intensity $\left(\frac{d\sigma}{d\Omega}\right)_{\mathrm{lab}}$, the correction

$$\left(\frac{d\sigma(\Theta_\gamma, \phi_\gamma)}{d\Omega_\gamma}\right)_{\mathrm{rest}} = \left(\frac{d\sigma(\Theta_{\gamma_{\mathrm{lab}}}, \phi_{\gamma_{\mathrm{lab}}})}{d\Omega_{\gamma_{\mathrm{lab}}}}\right) \cdot \frac{d\Omega_{\gamma_{\mathrm{lab}}}}{d\Omega_{\gamma_{\mathrm{rest}}}} \tag{4.3}$$

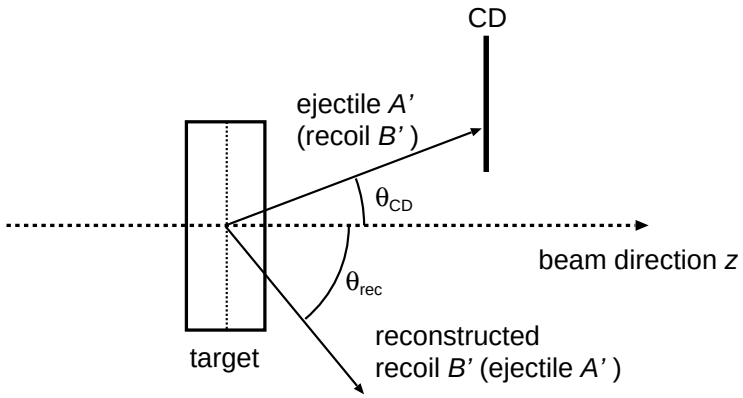

Figure 4.1: Schematic of the kinematical reconstruction. The measured energy and angle Θ_{CD} of the assumed ejectile A' (recoil B') detected in the CD Si counter allow to kinematically reconstruct the energy and angle Θ_{rec} of the recoil B' (ejectile A').

has to be applied with the solid angle correction factor $\frac{d\Omega_{\gamma_{\mathrm{lab}}}}{d\Omega_{\gamma_{\mathrm{rest}}}}$ [1] given by

$$\frac{d\Omega_{\gamma_{\mathrm{lab}}}}{d\Omega_{\gamma_{\mathrm{rest}}}} = \left(\frac{E_\gamma}{E_{\mathrm{lab}}}\right)^2 = \left(\gamma(1-\beta\cos(\Theta_{\mathrm{lab}}))\right)^2 . \tag{4.4}$$

In all following γ-spectra indicated as "Doppler corrected" the energy correction is performed according to equation 4.1 and the solid angle correction according to equation 4.3 on an event-by-event basis.

By assuming the γ-rays being emitted from the ejectiles or recoils, the γ-rays can be Doppler corrected for both of the nuclei resulting in two solutions and thus two differently corrected γ-spectra. In order to perform the Doppler correction, besides the direction of flight of the emitted γ-ray, the direction of the emitting nucleus and its β (and γ) value have to be known. The direction of the γ-ray in the laboratory system is obtained from the angles $\Theta_{\gamma_{\mathrm{lab}}}$ and $\phi_{\gamma_{\mathrm{lab}}}$ measured in the MINIBALL detectors. If, on the one hand, the emitting nucleus is detected in the CD, the β value and the angles Θ_{CD} and ϕ_{CD} can be determined directly from the measured energy and position in the Si counter. If, on the other hand, the emitting nucleus is the remaining collision partner, then its energy and direction of flight can be obtained from a kinematical reconstruction which is described in the following.

From the nucleus detected in the CD-detector the remaining nucleus of the collision can be reconstructed. In the given reaction $B(A,A')B'$, B is the stationary target and A is the projectile. The ejectile A' and the recoil B' are the particles after the reaction. In figure 4.1 the schematic of the reconstruction is shown. The reaction is assumed to take place at the target center. From the ejectile A' (recoil B') detected in the CD the recoil

[1] The index "rest" is given here to point out the difference between the laboratory system and the rest frame of the γ-emitting nuclei. The common notations for the polar, azimuth and solid angles in the rest frame in the present thesis are Θ_γ, ϕ_γ and Ω_γ, respectively.

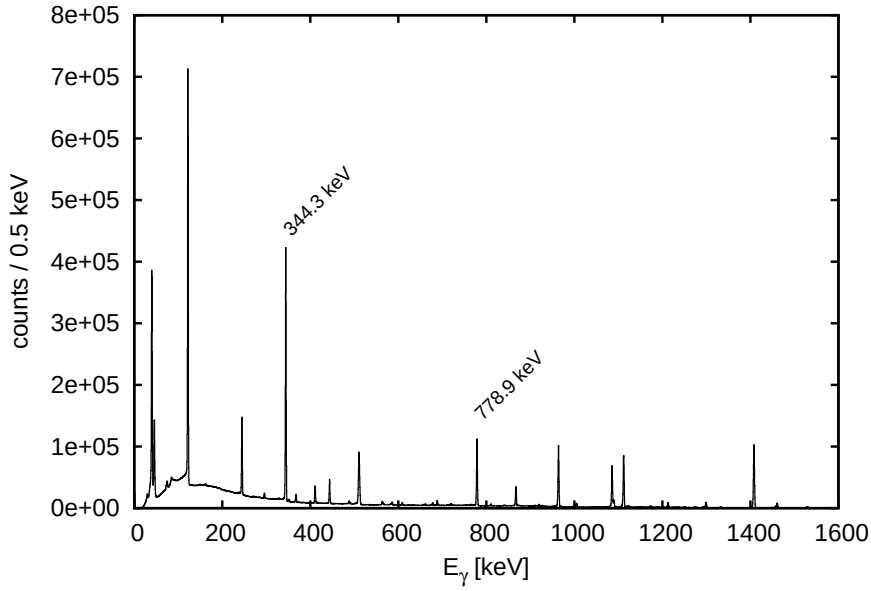

Figure 4.2: Sample γ-spectrum of a ^{152}Eu source. The sum spectrum of all cores of the 24 MINIBALL detectors is plotted including cluster addback. The two γ-lines at 344.3 keV and 778.9 keV which are used for the determination of the absolute efficiency are indicated.

B' (ejectile A') can be reconstructed where the energy losses of both particles in the target are considered. In the current kinematical reconstruction, both cases, i.e. with the ejectile and the recoil detected in the CD, are considered resulting in four hypothetical particles after the reconstruction: the assumed ejectile and recoil in the CD and the reconstructed recoil and ejectile. From the kinematics of the reaction the measured energy and angle in the CD-detector (see e.g. figure 6.2) allow to identify the reaction products and perform the Doppler correction assuming the γ-rays originating from a particular nucleus.

4.2 Calibration of the MINIBALL array

The work on the MINIBALL array that had to be performed during the offline analysis procedure included energy calibrations, efficiency determination, the optimization of the parameters for the pulse shape analysis (PSA) and the optimization of the positions of the MINIBALL clusters.

4.2.1 Energy calibration with ^{60}Co and ^{152}Eu

For the energy calibration of the channels of the MINIBALL array ^{60}Co and ^{152}Eu sources were used. Usually, online calibrations were performed before the main runs of the experiments with a ^{60}Co source, and after the experiments a ^{152}Eu source was used for the energy calibration. In figure 4.2 a sample γ-spectrum from a ^{152}Eu source is shown.

addback	E_γ [keV]	FWHM [keV]
no	1173.2	2.61
no	1332.5	2.75
yes	1173.2	2.73
yes	1332.5	2.88

Table 4.1: Obtained energy resolution for the 24 detectors of the MINIBALL array with and without cluster addback for Exp_Oct03.

The spectrum is a core spectrum of all 24 MINIBALL detectors of the MINIBALL array. To increase the efficiency of the array, cluster addback is performed, i.e. if energy is deposited in two or three detectors of a cluster then these energies are added to a cluster addback energy. For the cluster addback two conditions have to be fulfilled: the individual energies have to be above a certain threshold and the events have to be coincident, i.e. in a certain time window. In the analysis of the experiments presented in this work an addback threshold energy of 30 keV and a coincidence window of 600 ns were used. This time window was adjusted to contain coincident events where energy is deposited in more than one of the three detectors of a triple cluster.

In table 4.1 the energy resolution of the MINIBALL array for the two ^{60}Co γ-lines is given for Exp_Oct03. The combined energy resolution of all 24 MINIBALL detectors without cluster addback of 2.75 keV at 1332.5 keV should be compared to a value of 2.22 keV which was obtained for a single MINIBALL detector [24].

4.2.2 Efficiency determination at the Full energy peak

The total full energy peak (FEP) efficiency of the MINIBALL array was determined using the ^{152}Eu source. The relative efficiency curve was obtained using the intensities of the γ-lines and the absolute intensities given in table 4.2. The absolute efficiency was determined using the two coincident lines of the ^{152}Eu source at 344.3 keV and 778.9 keV. By requiring the γ at 778.9 keV in one of the triple clusters a value for the absolute efficiency at 344.3 keV was obtained from the number of gated 344.3 keV γ-rays. The relative efficiency curve was then scaled with the value of the absolute efficiency at 344.3 keV.

In figure 4.3 the obtained efficiency curves for Exp_Sep04 are plotted. The solid lines through the data points indicate fits to the data without (red) and with (green) cluster addback. The addback factor (blue) gives the ratio of the efficiency curves with to the one without addback. At an energy of 1 MeV the gain in efficiency by the cluster addback is about 14 %. For γ energies below $\sim$300 keV the efficiency with addback drops below the one without addback due to the fact that by adding random events the γ energies are shifted out of the full energy peak. However, the overall loss of about 5 % in the addback mode due to the random summing is outweighted by the still $\sim$15 % increase of the FEP efficiency at energies above 800 keV, i.e. in the energy range relevant for the decay of the first 2^+ states of ^{30}Mg (1482 keV) and ^{32}Mg (885 keV).

Source	Half-life	E_γ [keV]	I_γ [%]
^{60}Co	5.2714 y	1173.228 (3)	99.857 (22)
		1332.490 (6)	99.983 (6)
^{152}Eu	13.542 y	121.7817 (3)	28.37 (13)
		244.6975 (8)	7.53 (4)
		344.2785 (13)	26.57 (11)
		778.9045 (24)	12.97 (6)
		964.1	14.63 (6)
		1085.836 (9)	10.13 (5)
		1112.074 (4)	13.54 (6)
		1408.011 (4)	20.85 (9)

Table 4.2: Energies and intensities of used γ-ray calibration sources. For ^{152}Eu only the γ-lines used for the calibration and the efficiency determination are listed (data from [52]).

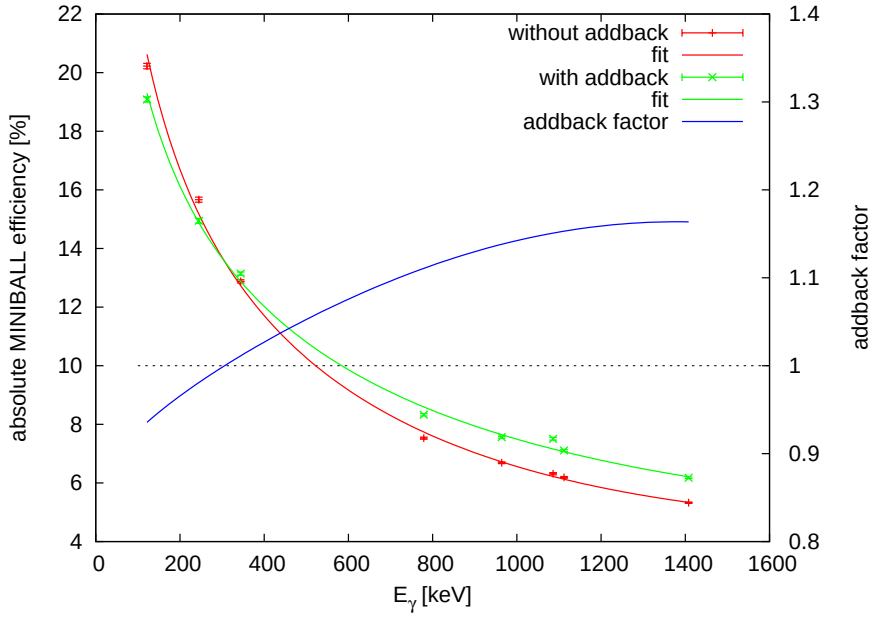

Figure 4.3: Comparison of absolute MINIBALL efficiency for Exp_Sep04 without (red) and with (green) cluster addback. The solid lines indicate fits to the data points. The addback factor which is the ratio of the efficiency with addback to that without addback is plotted in blue.

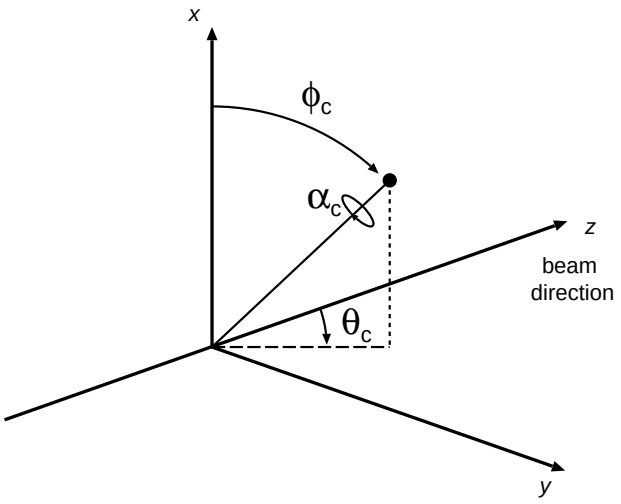

Figure 4.4: Definition of the MINIBALL cluster angles Θ_c, ϕ_c and α_c.

4.2.3 Cluster position optimization

As it was described in section 3.3, the eight triple clusters of the MINIBALL array are mounted on an adjustable frame (cf. picture 3.7). The position of the three individual Ge detectors of a cluster are determined by three angles: Θ_c, ϕ_c and α_c. In figure 4.4 the angles are indicated. Θ_c is the polar angle of the cluster axis with respect to the beam direction ($0° \leq \Theta \leq 180°$), ϕ_c is the angle around the beam axis ($0° \leq \phi \leq 360°$) and the angle α_c denotes the rotation angle of the cluster around its axis.

Two of the three cluster angles mentioned, namely Θ_c and α_c, have to be optimized for the following reasons: i) the value that can be read from a scale gives the Θ value of the arm on which the cluster is mounted and not of the cluster itself, and an exact value for the offset between the arm and the cluster is very difficult to determine; ii) the knowledge of the α_c angle is not very accurate (in 2003 no scale was available, in 2004 the calibration of the scale gave only raw α_c values).

The optimization of the Θ_c and α_c angles of the eight clusters was performed using the 1n-pickup reaction ^{2}H(^{22}Ne,^{23}Ne)p which populated the first $\frac{1}{2}^+$ state in ^{23}Ne at 1017 keV. In the experimental campaign Exp_Oct03 the stable ^{22}Ne residual gas beam from the EBIS source impinged with an energy of 2.25 MeV/u and an intensity of about 1×10^6 particles per second on a deuterated polyethylene (PE) target with a thickness of 10 μm.

In figure 4.5 the energy loss ΔE of the light reaction products in the CD-detector is plotted versus the total energy E_{total} measured in the $\Delta E - E$ telescope. For the region "A" the particles are stopped in the ΔE-detector. For proton energies of $\gtrsim 8$ MeV the protons pass through the ΔE-detector and are stopped in the E-detector ("B"), whereas for even higher proton energies ($\gtrsim 12$ MeV) the protons travel through both detectors and only the energy loss is measured ("C"). The deuteron energy has to exceed ~ 11 MeV in order to pass through the ΔE-detector.

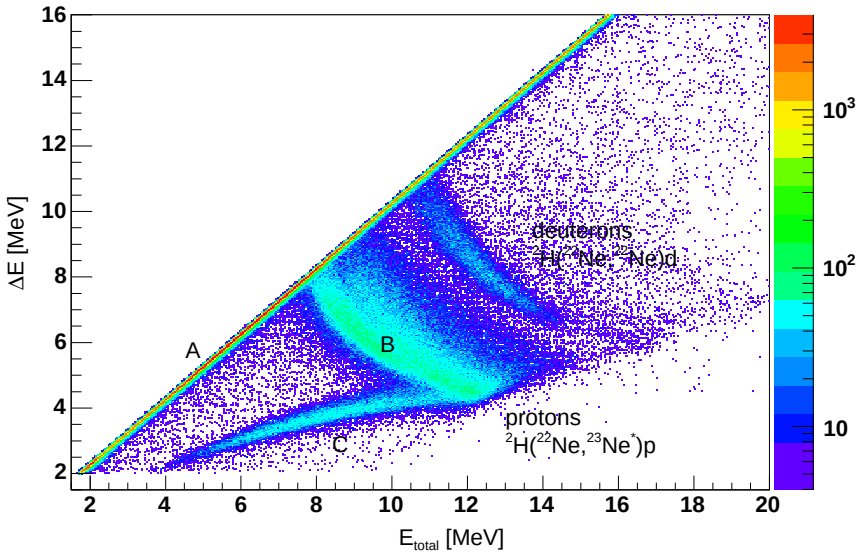

Figure 4.5: Energy loss ΔE vs. total energy E_{total} for ^{22}Ne at 2.25 MeV/u on a 10μm PE target. The protons from the 1n-pickup reaction as well as the elastically scattered deuterons can be identified.

For the MINIBALL cluster position determination, protons from region "B" were selected and the Doppler correction of the 1017 keV γ-line was performed on the segment level with the kinematically reconstructed ^{23}Ne ejectiles. The optimization of the Θ_c angle was carried out by using the energy position of the 1017 keV γ-rays measured in the MINIBALL array. For each cluster the Θ_c angle was varied in the offline analysis in a certain range and the energy position of the 1017 keV γ-ray was checked. The angle Θ_c could thus be determined by requiring the smallest quadratic deviation of the measured energy to the nominal energy of 1017 keV. The α_c angles were optimized using the measured resolution of the 1017 keV γ-line. By varying the α_c angles and requiring the best resolution, the α_c angles of all clusters could be determined.

In figure 4.6 the MINIBALL triple cluster position optimization is shown for one sample cluster for Exp_Oct03. Starting point is a first optimization of the Θ_c angle of the cluster. By fitting the data points with a quadratic function in a certain range, the first optimized Θ_c value is obtained which deviates in the shown example (figure 4.6 (a)) by 3.4° from the nominal Θ_c value. With this improved value the first α_c optimization is performed; for the shown example a rather large deviation to the uncorrected value of 10.5° is found (figure 4.6 (b)). In the second iteration step of the optimization only minor deviations from the determined values of the first step are found (0.2° deviation both for the second Θ_c (figure 4.6 (c)) and α_c (figure 4.6 (d)) optimizations). The accuracy of the angle determination is about 1° for the Θ_c angle and about 2° - 3° for the α_c angle. The optimization procedure was carried out for all eight clusters of the MINIBALL array.

Figure 4.7 shows the resulting γ-spectra after the cluster position optimization for Exp_Oct03. The resolution of the 1017 keV γ-line of ^{23}Ne improves from 14.87 keV (no

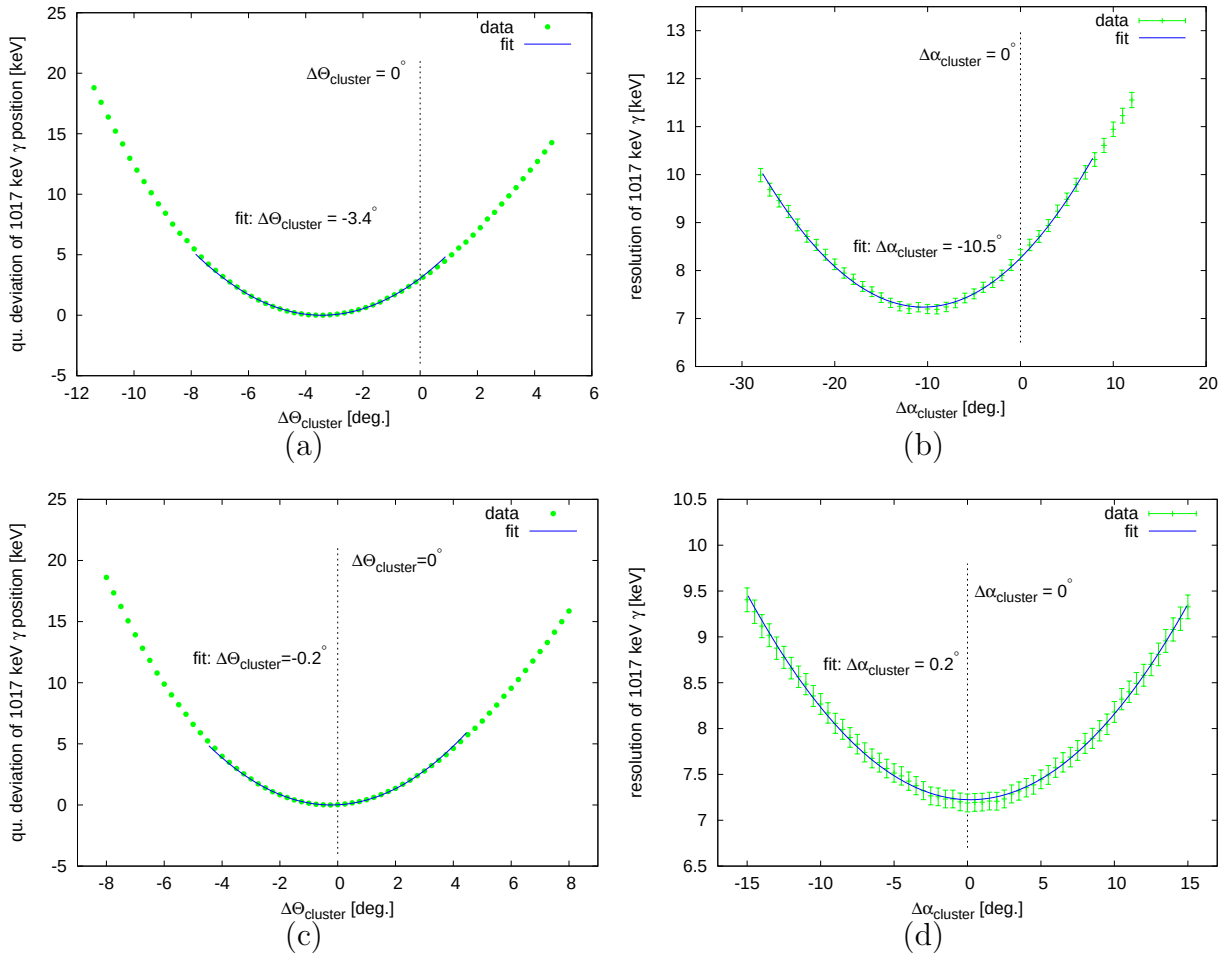

Figure 4.6: Cluster position optimization procedure for one sample cluster. By varying (in software) the Θ_c and α_c angles of the cluster the optimal angles could be obtained from the position (Θ_c) and the resolution (α_c) of the 1017 keV γ of ^{23}Ne: in the first optimization steps rather large deviations from the nominal values are observed ((a) & (b) for the Θ_c and α_c optimizations, respectively). In the second iteration only small corrections to the values deduced from the first iteration are found ((c) & (d)).

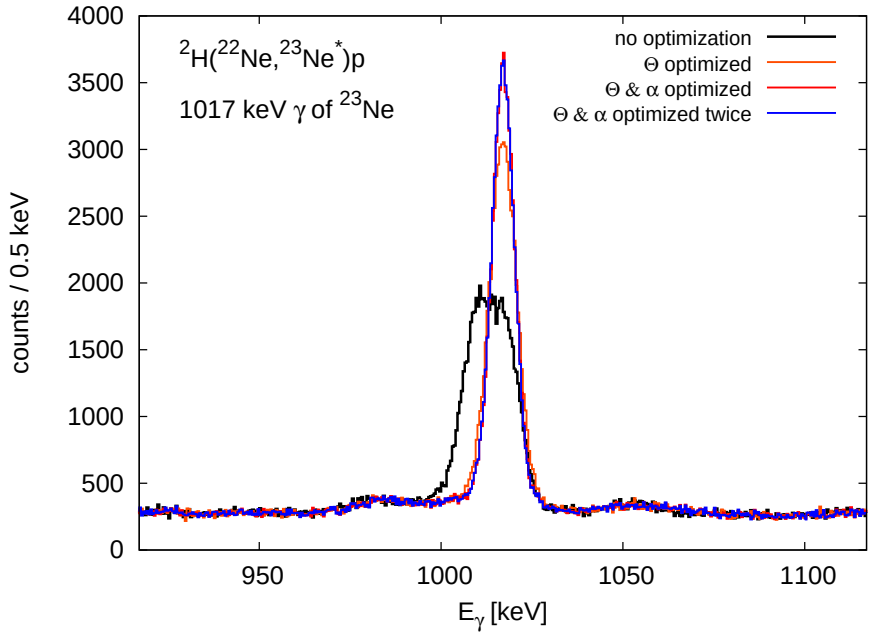

Figure 4.7: Result of the cluster position optimization for Exp_Oct03: by optimizing the angles Θ_c (orange) and α_c (red) the resolution of the 1017 keV γ-line of ^{23}Ne significantly improves compared to the non-optimized spectrum (black). The final resolution obtained is 7.68 keV (blue curve) after the second iteration step. After the optimization the measured position of the 1017 keV line also completely agrees with the nominal position.

optimization, black curve) over 9.32 keV (only Θ_c optimization, orange) to 7.69 keV (red curve) when both Θ_c and α_c optimizations are performed. The second iteration has only minor influence on the result as the resolution improves to 7.68 keV (blue curve). By optimizing the MINIBALL cluster positions a total gain in resolution of the 1017 keV line of almost a factor of 2 (from 14.87 keV to 7.68 keV for Exp_Oct03) is achieved.

4.2.4 PSA parameter optimization

The use of digital electronics for the readout of the MINIBALL array allows to perform pulse shape analysis algorithms which enable to determine the position of the detected γ-rays (see section 3.3.2 and figure 3.5). The parameters of these algorithms for the determination of the radius r and the azimuth angle ϕ are calibrated by optimizing the energy resolution of Doppler shifted and broadened de-excitation γ-rays like the 1017 keV line of ^{23}Ne. Figure 4.5 shows a comparison of the achieved energy resolutions for the 1017 keV γ for Exp_Oct03 where the Doppler correction is performed on core level, with the segment information and by using the position from the PSA with the formulas

$$\begin{aligned} r &= 0.094\frac{\text{mm}}{\text{ns}} \cdot T_s + 1.213\,\text{mm} \\ \phi &= 13.812^\circ \cdot \log\left(\frac{|q_-|}{|q_+|}\right) + 2.560^\circ + \phi_s\,, \end{aligned} \tag{4.5}$$

where for the ϕ determination, the segment angle ϕ_s has to be added to the inner segment angle to get the global detector ϕ value. Energy resolutions of the ^{23}Ne line of 13.9 keV and 7.7 keV are obtained when applying a Doppler correction on core and segment level, respectively. The use of the position information extracted from the PSA algorithms improves the resolution to 7.2 keV. A further improvement of the energy resolution would be possible by using individual PSA calibration parameters for each individual segment of the MINIBALL array. However, in the analysis of the current experiments, global PSA parameters as shown in equations 4.5 were used for all segments of the MINIBALL array.

4.3 Calibration of the CD-Si detectors

For the detection of the reaction products a $\Delta E - E$ telescope was installed in the MINIBALL target chamber (see section 3.4.1). The offline analysis of the Coulomb excitation experiments presented in this work included energy calibrations of both parts of the telescope as well as the determination of the exact rotation angle of the ΔE-detector.

4.3.1 Energy calibration

The energy calibration of the ΔE-detector was carried out using a triple α source of ^{239}Pu, ^{241}Am and ^{244}Cm. By identifying and fitting the three dominant α peaks of the mixed source, calibration factors for all 160 channels of the CD-detector could be determined.

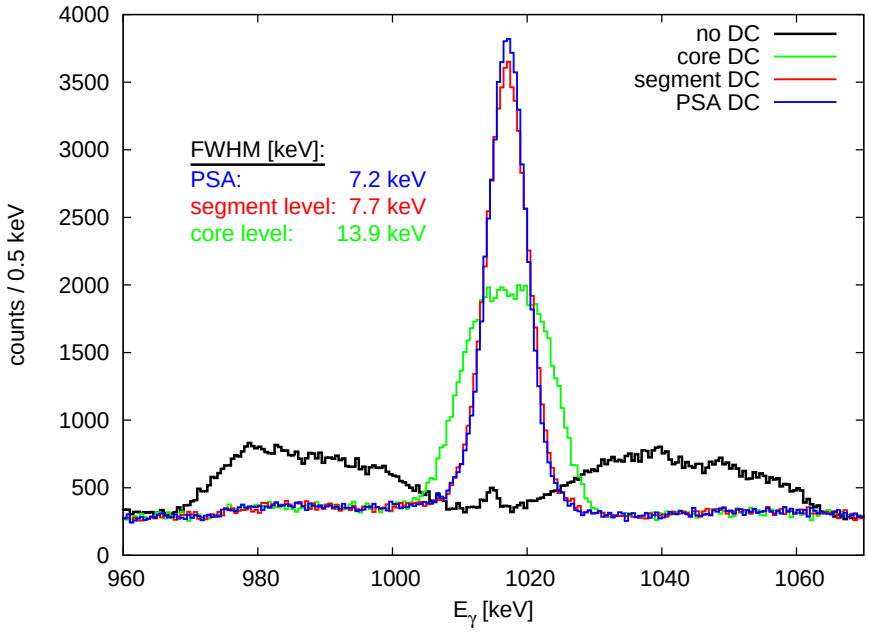

Figure 4.8: Comparison of ^{23}Ne 1017 keV γ-line Doppler correction on core, segment and PSA level: by using the information of the segments and the pulse shape analysis (PSA) an improvement in the FWHM resolution of the ^{23}Ne line from 13.9 keV to 7.2 keV is achieved. The uncorrected spectrum is also shown.

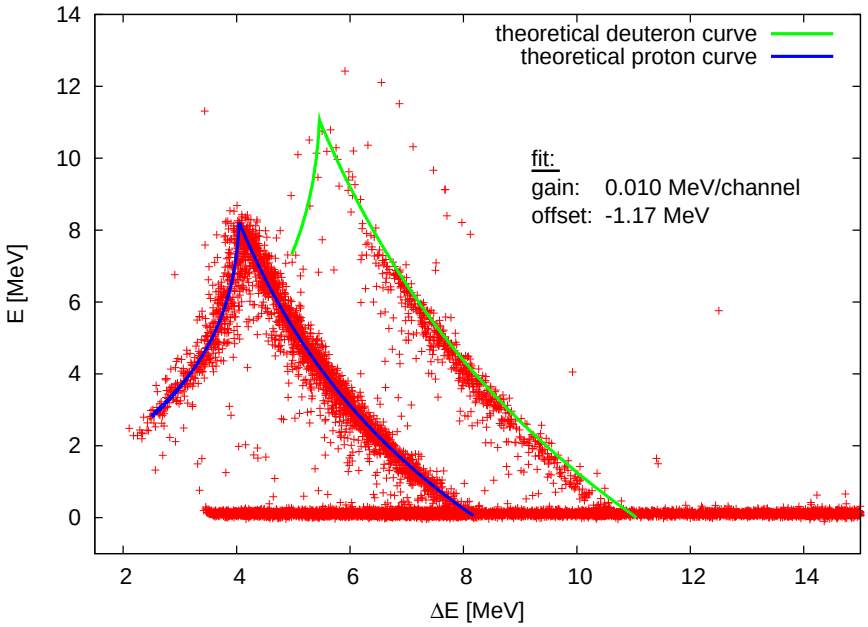

Figure 4.9: $E - \Delta E$-Plot showing the result of the CDE-calibration for one sample sector for Exp_Oct03. The data points after calibration and the theoretical energy loss curves for both protons and deuterons are plotted as well as the resulting calibration factors for the chosen sector.

The four sectors of the E-detector were calibrated using the energy loss of the protons from the 1n-pickup reaction ^{2}H(^{22}Ne,^{23}Ne*)p. To decrease the ΔE energy spread of the protons in region "B" only particles with a scattering angle of $19.5° \leq \Theta_{CD} \leq 20.1°$ in the ΔE-detector were selected (cf. figure 4.5).

From the thicknesses of the CDE sectors and the chosen scattering angle range the theoretical energy loss curve for protons was first determined. By varying the calibration constants (gain and offset) the data points were afterwards fitted to the theoretical proton curve. In figure 4.9 the result of the calibration is shown for one sample sector for Exp_Oct03. After the calibration the proton data points agree very well with the theoretical proton energy loss curve. As a test of the calibration also the theoretical curve for deuterons is plotted which is also in good agreement with the data.

4.3.2 CD azimuth angle optimization

To ensure a proper Doppler shift correction a position calibration of the CD-detector in the MINIBALL target chamber had to be performed. The MINIBALL coordinate system is defined such that the beam direction coincides with the z-axis, the x-axis is pointing upwards and therefore the y-axis is pointing "to the right" in beam direction (see figure 4.4). While the polar angle Θ_{CD} is well enough determined by the geometry, all CD-sectors are slightly rotated clockwise as can be seen in figure 3.12.

To determine the exact azimuth angle Φ_{CD} of the CD-detector, the ^{22}Ne de-excitation γ-line at 1274.5 keV from a Coulomb excitation experiment with ^{22}Ne is used. In Exp_Oct03, a ^{22}Ne beam with an energy of 2.25 MeV/u was incident on a 1.0 $\frac{\text{mg}}{\text{cm}^2}$ natural Ni target where the first excited 2^+ state in ^{22}Ne was populated. As a starting point of the optimization procedure it was assumed that the middle of the CD sector pointing "upwards" is aligned exactly in x-direction. By adding an offset-angle $\Delta\Phi_{CD}$ to the nominal Φ_{CD} values and by varying $\Delta\Phi_{CD}$ in the offline analysis, the offset angle $\Delta\Phi_{CD}$ could be determined by optimizing the energy resolution of the 1274.5 keV γ-ray.

In figure 4.10 the Doppler corrected ^{22}Ne line is shown for different offset angles $\Delta\Phi_{CD}$. The peaks at 1274.5 keV were fitted assuming a Gaussian peak shape and a linear background. The measured energy resolution improves for offset angles up to $+13°$ (left column of figure 4.10) whereas a further rotation again worsens the resolution (right column of figure 4.10).

The result of the optimization for Exp_Oct03 is illustrated in figure 4.11. To determine the rotation angle the CD offset values were varied from 0° to 20° in steps of 1° and the measured energy resolutions fitted. A value for the offset angle $\Delta\Phi_{CD}$ of $+12.6° \pm 2.5°$ was determined (see figure 4.11 (a)).

Figure 4.11 (b) shows a scatter plot of the detected ^{22}Ne ejectiles (when looking in beam direction) with the determined offset included. It can be seen from the intensity of the scattered particles that the beam was not fully centered in this particular experiment.

4.4 Determination of beam impurities

For Coulomb excitation experiments with radioactive beams a careful investigation of possible beam contaminations is essential. Contaminants will cause excitations of the target nuclei and therefore have to be determined precisely in order to be able to deduce the $B(E2)$ values of the projectiles relative to those of the target nuclei (cf. equation 2.31).

4.4.1 Sources for beam contaminations

At the REX-ISOLDE facility there are several sources for possible beam contaminants which will be discussed in the following. When tracking the radioactive ions on their way from the production to the MINIBALL target the first source for contamination are isobaric contaminants which are directly released from and ionized at the primary ISOLDE target. Due to the high selectivity of the ISOLDE RILIS laser ionization scheme (see section 3.1.2), possible isobaric contaminants originating from surface ionization are suppressed to a large extent as compared to the wanted radioactive ions. Isobaric contamination can also be produced by β-decay during the trapping and charge breeding processes by REX-ISOLDE. Finally, stable residual gas isotopes with similar A/q-values as the radioactive nuclei can be produced and released from the EBIS source and may pass the A/q-separator having only a moderate A/q-resolution (see section 3.2). In the following section different methods are discussed which allow to determine the amount of contaminations in the beam.

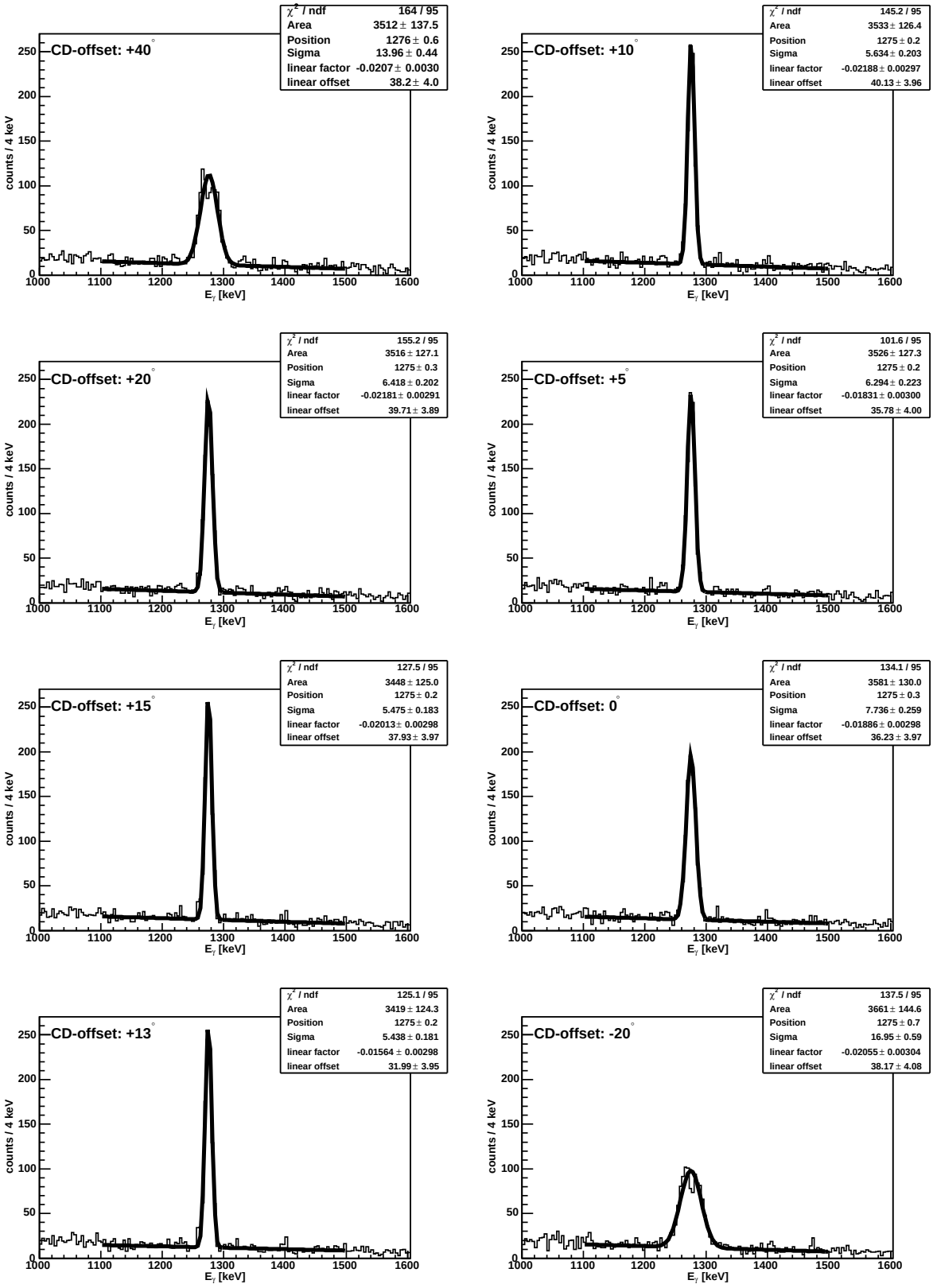

Figure 4.10: Doppler corrected ^{22}Ne 1274.5 keV line for different offset angles $\Delta\Phi_{\mathrm{CD}}$ of the CD-detector (for further explanations see text).

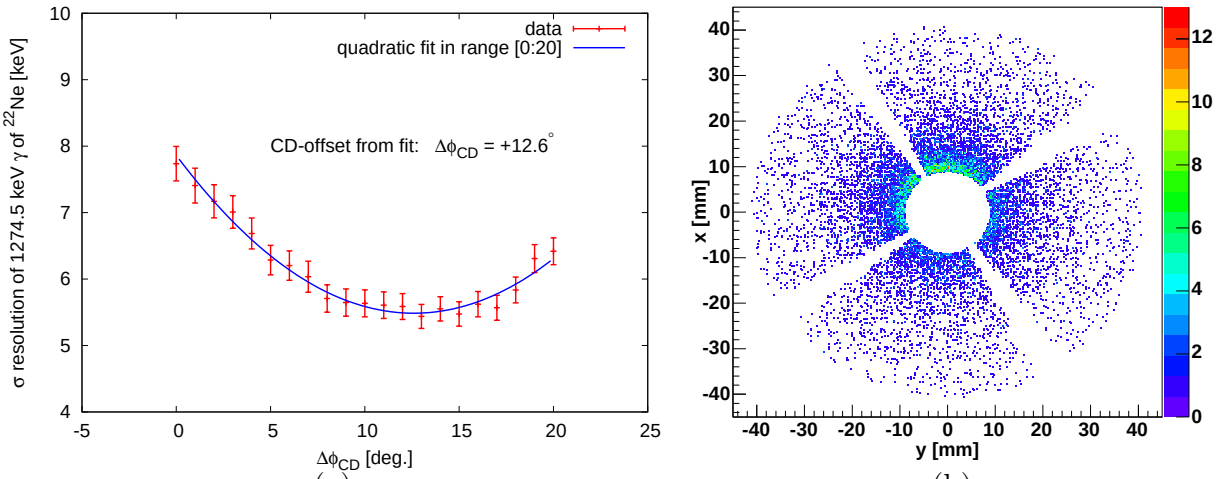

(a) (b)

Figure 4.11: Result of the CD azimuth angle optimization for Exp_Oct03: (a) measured energy resolutions of the 1274.5 keV γ-line as a function of the CD offset value. A final value of +12.6° was determined. (b) scatter plot for the ^{22}Ne ejectiles detected in the CD (looking in beam direction). The determined offset results in a clockwise rotation of the detector compared to a symmetric arrangement where the middle of the upper sector would point exactly in x-direction (cf. picture 3.12).

4.4.2 Methods for determination of beam purity

As in the current Coulomb excitation experiments the ejectile (recoil) energies are measured in the CD-detector which allow to distinguish beam contaminants with different mass numbers A, isobaric contaminations present the main concern. The total amount of isobaric contaminants is composed of fractions from the β-decay and from the ISOLDE source. The β-decay part can be calculated from the known breeding times and life times of the radioactive ions, whereas the fraction originating from the ISOLDE source has to be determined either by LASER on/off-measurements and/or by analyzing the time dependence of the beam intensity with respect to the proton ("T1") pulse impact on the ISOLDE target. The determination of the total beam contamination is also possible by analyzing the γ-intensities due to β-decay collected in the MINIBALL target chamber. A detailed analysis of the different beam components can be performed with a thin ΔE-detector which was installed in 2004 (see figure 3.10). The methods mentioned above will be explained below and examples given.

Breeding and life time analysis

The amount of isobaric contaminants due to the β-decay of the secondary beam can be deduced from the trapping and breeding times and the life times of the radioactive ions. The trapping time t_t in the REX-TRAP is given by the repetition frequency of the process

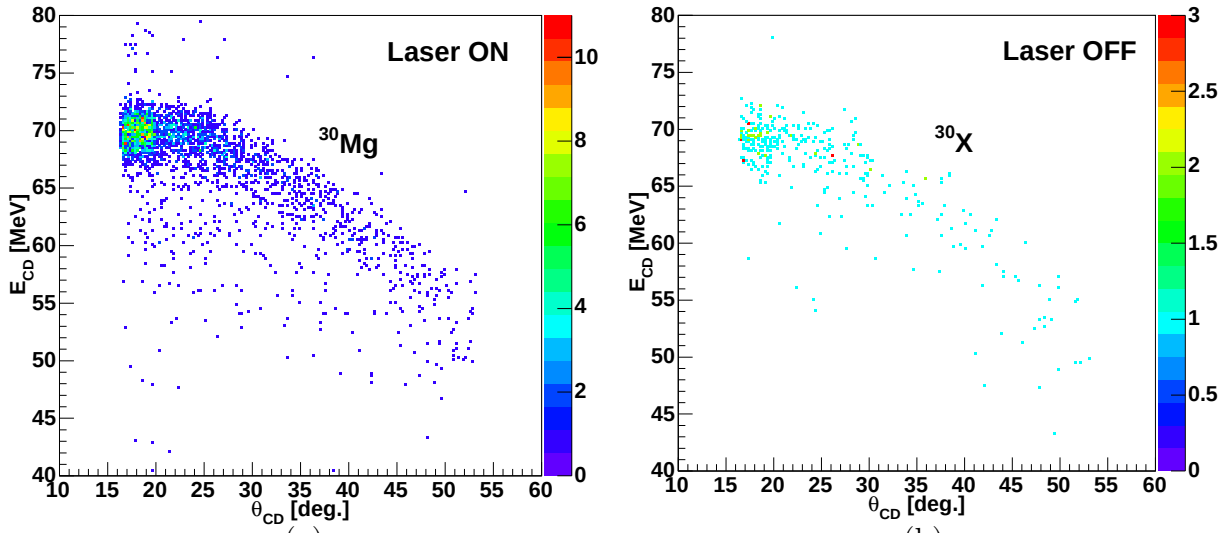

(a) (b)

Figure 4.12: CD-energy vs. Θ_{CD} for Laser on/off-measurements with a 2.69 MeV/u ^{30}Mg beam impinging on a 1.1 $\frac{\mathrm{mg}}{\mathrm{cm}^2}$ ^{107}Ag target for Exp_Sep04: elastically scattered $A = 30$ ions for events with "Laser ON" (a) and "Laser OFF" (b) ($0 \leq T_{\mathrm{p}} \leq 1.2$ s). From the ratio of the intensities the amount of isobaric contamination can be determined.

of 49 Hz to $t_{\mathrm{t}} \approx 20.4$ ms. For Exp_Sep04 the EBIS breeding time for ^{32}Mg was 16 (2) ms. The minimum time for trapping and breeding is therefore 16 ms for ^{32}Mg ions which enter the trap right *before* the transfer to the EBIS, and the maximum time is 36.4 ms for ions which enter the trap right *after* the transfer of the previous bunch to the EBIS. By integrating over this time span (16 ms to 36.4 ms) the amount of ^{32}Al and ^{32}Si can be determined with the aid of the known life times of ^{32}Mg ($t_{1/2} = 95\,(16)$ ms from [53]) and ^{32}Al ($t_{1/2} = 33\,(4)$ ms from [53]). The calculation results in the following amounts of isobaric contaminants in the ^{32}Mg beam for ^{32}Al and ^{32}Si: $N(^{32}\mathrm{Al}) = 13.1\,(21)\,\%$ and $N(^{32}\mathrm{Si}) = 4.26\,(88)\,\%$.

LASER on/off-measurements

To determine the amount of isobaric contaminants originating from the ISOLDE source, LASER on/off-measurements have been performed where the laser of the RILIS was periodically blocked mechanically. In figure 4.12 the measured CD-energy is plotted versus the Θ_{CD} angle where the 2.69 MeV/u ^{30}Mg beam was incident on a 1.1 $\frac{\mathrm{mg}}{\mathrm{cm}^2}$ ^{107}Ag target. The plots only contain events with times T_{p} since the last T1 proton pulse of less than 1.2 s, i.e. $0 \leq T_{\mathrm{p}} \leq 1.2$ s, as this time window is also used in the analysis of this ^{30}Mg Coulomb excitation experiment (see section 6.2).

If the laser is active, the ^{30}Mg ions as well as possible isobaric contaminants are detected in the CD-detector (a) whereas in the case of "Laser OFF" (b) no ^{30}Mg is present and only

the isobaric contaminants ^{30}X are detected. These are expected to consist mainly of ^{30}Al as other possible isobars are difficult to surface ionize and thus have negligible yields. For Exp_Sep04, the analysis of the LASER on/off-measurements resulted in a ^{30}Al fraction in the beam of $N(^{30}\mathrm{Al}) = 12.73\,(71)\,\%$.

Release curve analysis

Another method to determine the isobaric contamination originating from the ISOLDE source utilizes the timing information of the proton ("T1") pulse impinging on the primary ISOLDE target. In figure 4.13 the time T_p since the last proton impact is shown for the particles detected in the CD for the ^{30}Mg beam of Exp_Oct03. As it was explained in

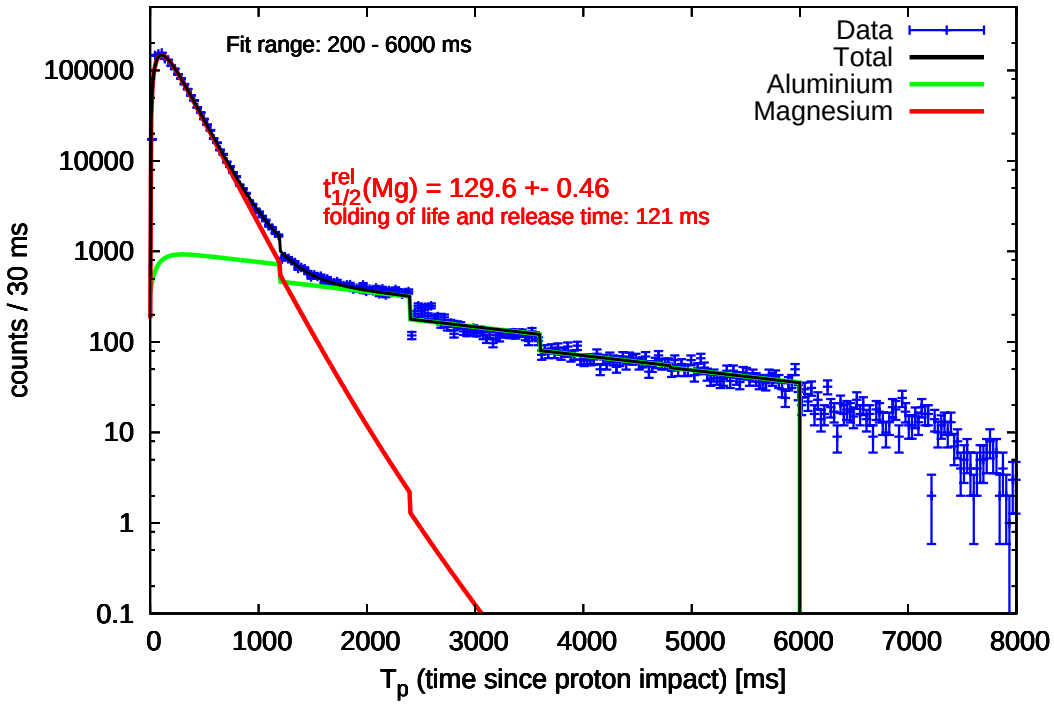

Figure 4.13: Time difference T_p to last proton pulse for CD events in the ^{30}Mg run of Exp_Oct03: by fitting the release curves the relative amount of ^{30}Al in the beam can be determined as a function of T_p.

section 3.1.2, the minimum time distance of T1 pulses impinging on the primary target is 1.2 s. This explains the steps in figure 4.13 occurring each 1.2 s. It is known [54] that Mg undergoes a fast release from the ISOLDE target whereas a slow release is characteristic for Al. By fitting exponential release curves for ^{30}Mg and ^{30}Al to the data, an average value for the fraction of ^{30}Al in the beam of $N(^{30}\mathrm{Al}) = 2.01\,(7)\,\%$ is obtained restricting the analysis to the first 1.2 s after the T1 pulse. The release time of 129.6 (46) ms determined for ^{30}Mg is in good agreement with the value of 121 ms which is obtained when folding

the half-life of ^{30}Mg ($t_{1/2}(^{30}\mathrm{Mg}) = 335\,(17)$ ms from [53]) with the release time of 190 ms from [54].

Analysis of β-decay

The total amount of isobaric contamination can also be obtained by investigating the γ-intensities originating from β-decay of the radioactive isotopes. The procedure is explained in the following for ^{30}Mg. The β-decay of ^{30}Mg results to $73\,(10)\,\%$ in a ^{30}Al γ-ray with an energy of 443.6 keV. The branching ratio for the decay of ^{30}Al by the 1263.2 keV γ of ^{30}Si is $40\,(1)\,\%$ (both branching ratios taken from [53]). To deduce a value for the ^{30}Al contamination in the beam the intensities of these two γ-lines have to be determined as well as the relative efficiencies of the MINIBALL array for these energies. It follows that the fraction of ^{30}Al is given by

$$\frac{N(^{30}\mathrm{Al})}{N(^{30}\mathrm{Mg}) + N(^{30}\mathrm{Al})} = \frac{\frac{\epsilon_\gamma^{\mathrm{Al}} N_\gamma^{\mathrm{Si}}}{\epsilon_\gamma^{\mathrm{Si}} \cdot b^{\mathrm{Si}}} - N_\gamma^{\mathrm{Al}}}{\frac{\epsilon_\gamma^{\mathrm{Al}} N_\gamma^{\mathrm{Si}}}{\epsilon_\gamma^{\mathrm{Si}} \cdot b^{\mathrm{Si}}} - N_\gamma^{\mathrm{Al}} + \frac{N_\gamma^{\mathrm{Al}}}{b^{\mathrm{Al}}}}\,, \tag{4.6}$$

where N_γ denotes the number of detected γ-rays in the MINIBALL, ϵ_γ are the efficiencies and the b values denote the branching ratios mentioned above. It turns out that for the relative efficiencies of equation 4.6, the γ-intensities measured in the MINIBALL array are sufficient. For the ^{30}Mg run of Exp_Sep04, the analysis of the β-decay results in a ^{30}Al fraction in the beam of $N(^{30}\mathrm{Al}) = 17.32\,(2.70)\,\%$ for the time window of $0 \leq T_\mathrm{p} \leq 1.2$ s.

Analysis of data from thin ΔE-detectors

In 2004 two 10 μm thin ΔE-detectors were installed in the MINIBALL setup (see figure 3.10) to determine and monitor the beam composition during the experimental campaigns (see also [55]). As the energy loss is proportional to the square of the charge Z of the detected nuclei ($-\frac{dE}{dx} \propto Z^2 \cdot f(\beta)$, where β is the particle velocity) and the velocity β is the same for all isobaric beam components, a measurement of the specific energy losses allows to determine the composition of the isobaric beam.

In figure 4.14 (a) the measured energy loss in one of the ΔE-detectors is plotted versus the time T_p since the last proton pulse for a 2.84 MeV/u ^{32}Mg beam impinging on a 4.4 $\frac{\mathrm{mg}}{\mathrm{cm}^2}$ ^{107}Ag target. Besides the ^{32}Mg and the ^{32}Al fractions also a stable ^{32}S beam component can be observed originating from the residual gas of the EBIS. As the ^{32}Mg and the ^{32}Al show the same fast release behavior it follows that the isobaric ^{32}Al is mainly due to β-decay during the trapping and breeding cycle and not from the ISOLDE target. The component of ^{32}Si originating from the β-decay of ^{32}Al is not visible as it is superimposed by the ^{32}S. This is due to the fact that for ^{32}Si the energy *loss* is measured while the ^{32}S component is stopped and therefore the *total* energy is absorbed in the ΔE-detector. When using a thinner ^{107}Ag target of 1.1 $\frac{\mathrm{mg}}{\mathrm{cm}^2}$, however, the ^{32}Si can be separated from the ^{32}S and therefore a value for the ^{32}Si amount in the beam could be extracted as well. In figure 4.14 (b) a fit to the different components of the beam is shown (from [55]).

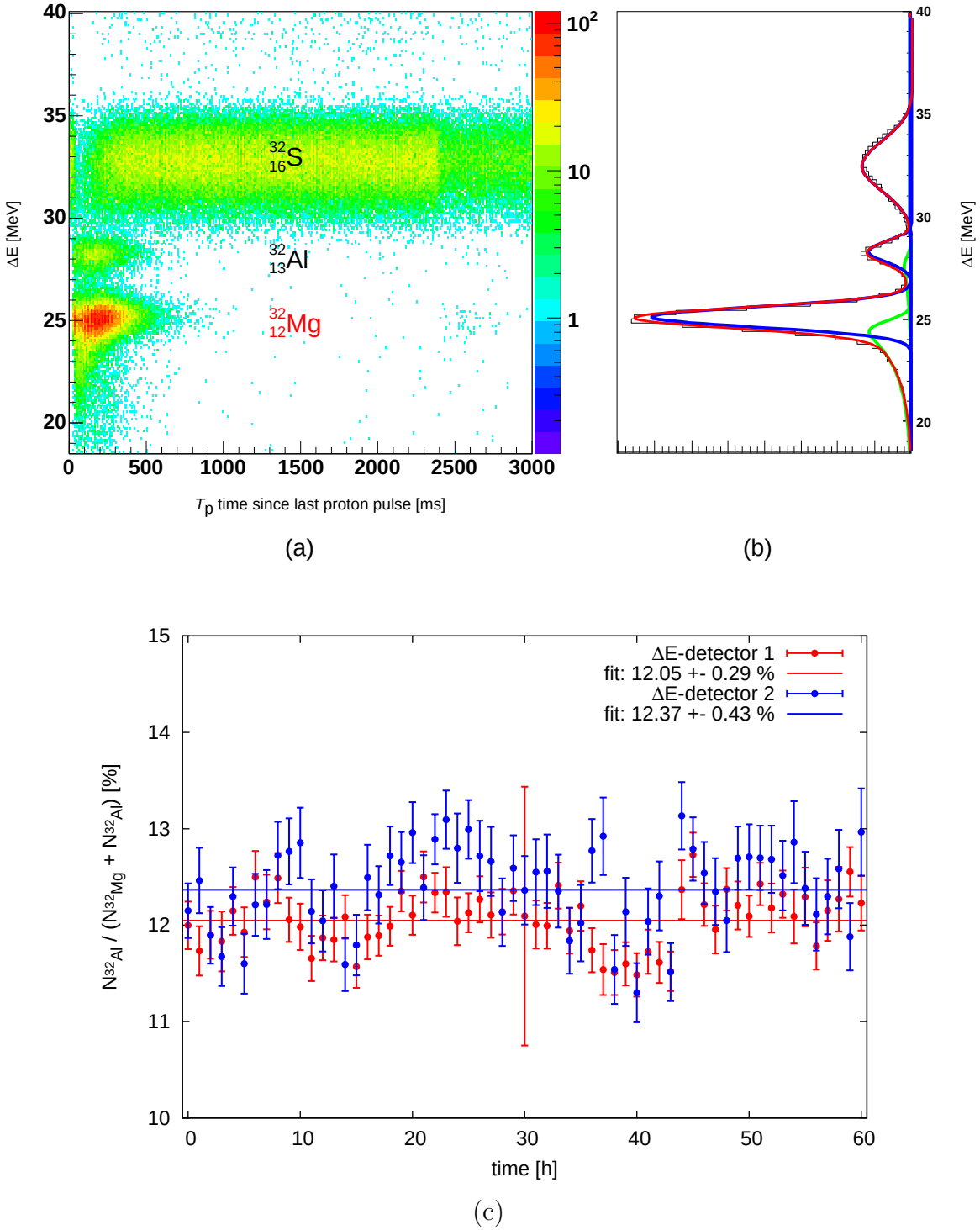

Figure 4.14: Analysis of data from the ΔE-detectors for a 2.84 MeV/u ^{32}Mg beam incident on a 4.4 $\frac{\text{mg}}{\text{cm}^2}$ ^{107}Ag target: (a) energy loss vs. time T_p since last proton pulse for one of the detectors. The ^{32}Mg can be seen as well as the isobaric ^{32}Al and the stable ^{32}S. (b) Projection of (a) onto the energy loss axis ΔE for $0 \leq T_\text{p} \leq 400$ ms (from [55]). (c) Ratio of ^{32}Al over ^{32}Mg plus ^{32}Al for the ^{32}Mg beam of Exp_Sep04 measured with both ΔE-detectors, restricting the analysis to $0 \leq T_\text{p} \leq 400$ ms. The ^{32}Al fraction could be continuously monitored over the whole measuring time of about 60 h (from [55]).

Figure 4.14 (c) shows the results obtained from the analysis of both ΔE-detectors where the fraction of ^{32}Al in the beam was monitored over the whole measuring time of about 60 h. The number $N(^{32}\mathrm{Al})$ of the isobaric ^{32}Al in the beam was obtained from the measured intensities in the ΔE-detectors where the different Rutherford cross section (which, according to equation 2.2, is proportional to the square of the projectile charge Z_p) for ^{32}Mg and ^{32}Al was considered, and an integration over the energy loss (which is also different for the two $A = 32$ isobars) in the target was performed (see also [55]). The beam composition was determined each hour and only events with T_p times of less than 400 ms were considered. As the ^{32}S can be separated almost completely from the ^{32}Mg by the different energies measured in the CD-detector (see section 6.3.2) and due to the ^{32}S suppression by the applied T_p time cut, only the ratio of ^{32}Al to ^{32}Al plus ^{32}Mg was investigated. From figure 4.14 (c) it can be seen that the ^{32}Al component is constant in time and that the values deduced from both detectors are in good agreement within the errors.

The methods explained above allowed to determine the beam impurities for the different measuring campaigns on a percentage level (for details see section 6).

4.5 Determination of Angular Correlation Factors

In the Coulomb excitation experiments presented in this work the $B(E2)\uparrow$ values of the projectiles are deduced with the help of the known target $B(E2)\uparrow$ values (see section 2.8). This requires the determination of the relative angular correlation factors $\frac{W_\gamma^t}{W_\gamma^p}$ of projectiles and targets for the experiments carried out (cf. formula 2.31).

In a first step the γ-energy and solid angle dependent MINIBALL FEP efficiency distributions $\epsilon(E_\gamma, \Theta_{\gamma_\mathrm{lab}})$ were determined from a GEANT4 [56] simulation of the MINIBALL setup [57]. Figure 4.15 shows the obtained efficiency distributions for five different γ-energies (324.8 keV, 432.2 keV, 885.3 keV, 1332.5 keV and 1482.1 keV) which are relevant for the present Coulomb excitation experiments. For each energy 5 million events were simulated. To account approximately for the fact, that, in the analysis of the Coulomb excitation experiments, besides the Doppler shift only the intensity transformation $\frac{d\Omega_{\gamma_\mathrm{lab}}}{d\Omega_{\gamma_\mathrm{rest}}}$ from the lab into the rest frame of the emitting nuclei is performed on an event-by-event basis (see section 4.1), but not of the detection angles $\Theta_{\gamma_\mathrm{lab}}$ and $\phi_{\gamma_\mathrm{lab}}$, the $\epsilon(E_\gamma, \Theta_{\gamma_\mathrm{lab}})$ distributions were transformed by shifting the $\Theta_{\gamma_\mathrm{lab}}$ scale according to [58]

$$\cos(\Theta_{\gamma_\mathrm{cm}}) = \frac{\cos(\Theta_{\gamma_\mathrm{lab}}) - <\beta>}{1 - <\beta> \cdot \cos(\Theta_{\gamma_\mathrm{lab}})} \tag{4.7}$$

with an average recoil velocity $<\beta>$. The resulting efficiency distributions were then fitted and normalized.

As a second step the de-excitation γ-ray angular distributions following the Coulomb excitation were determined using the coupled-channel code GOSIA [29]. The distributions were obtained by integrating the double-differential cross sections $d^2\sigma(\Theta_\mathrm{cm}, \phi_\mathrm{cm}; \Theta_\gamma)$ over

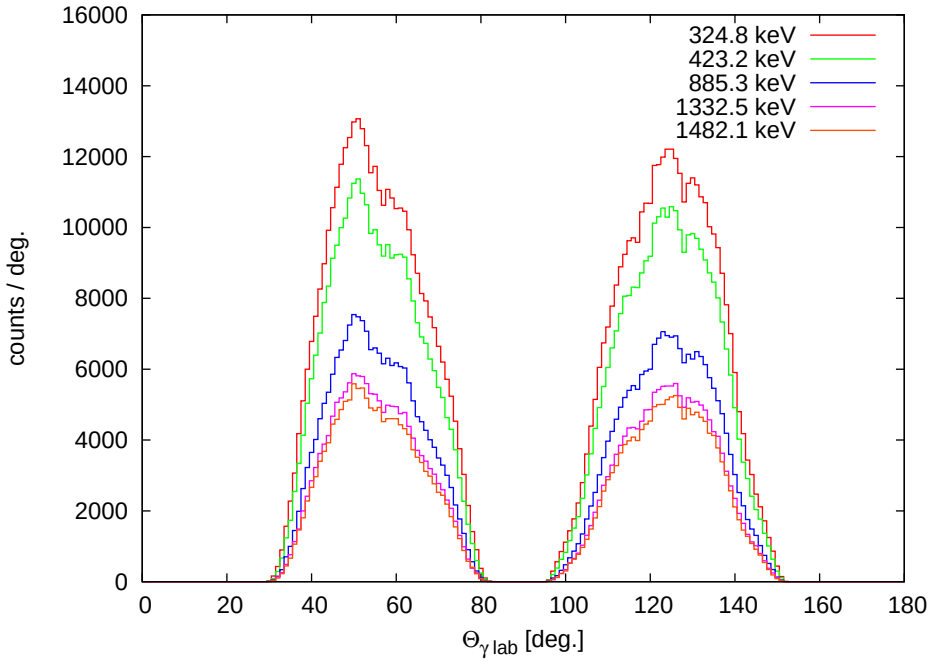

Figure 4.15: γ-ray efficiency distributions for five different γ-energies obtained from a GEANT4-simulation of the MINIBALL setup [57].

the corresponding scattering angles Θ_{cm} and ϕ_{cm}. As an example the c.m. angular distributions for the Coulomb excitation reaction of a ^{32}Mg (2.84 MeV/u) beam incident on a 4.4 $\frac{\mathrm{mg}}{\mathrm{cm}^2}$ ^{107}Ag target are shown in figure 4.16 where both projectile and target excitations occur: in ^{32}Mg the de-excitation γ-ray from the first 2^+ state at 885.3 keV to the 0^+ ground state, in ^{107}Ag the γ-rays from the first $\frac{5}{2}^-$ state at 423.2 keV and the first $\frac{3}{2}^-$ state at 324.8 keV to the $\frac{1}{2}^-$ ground state. Also shown is the approximate Θ_γ-range in the cm-system covered by the MINIBALL array. By folding the (normalized) angular distributions with the normalized efficiency distributions for both projectile and target de-excitation γ-rays, the relative angular correlation factors $\frac{W_\gamma^t}{W_\gamma^p}$ can be determined. In table 4.3 the correlation factors $\frac{W_\gamma^t}{W_\gamma^p}$ are listed for the Coulomb excitation experiments of Exp_Sep04. It can be seen that the deduced factors are small and result in increased projectile excitation cross sections and thus increased $B(E2)\uparrow$ values of only about 2 % (cf. formula 2.31). Note that the smallness of the relative angular correlation factors warrants the approximations made in their derivation.

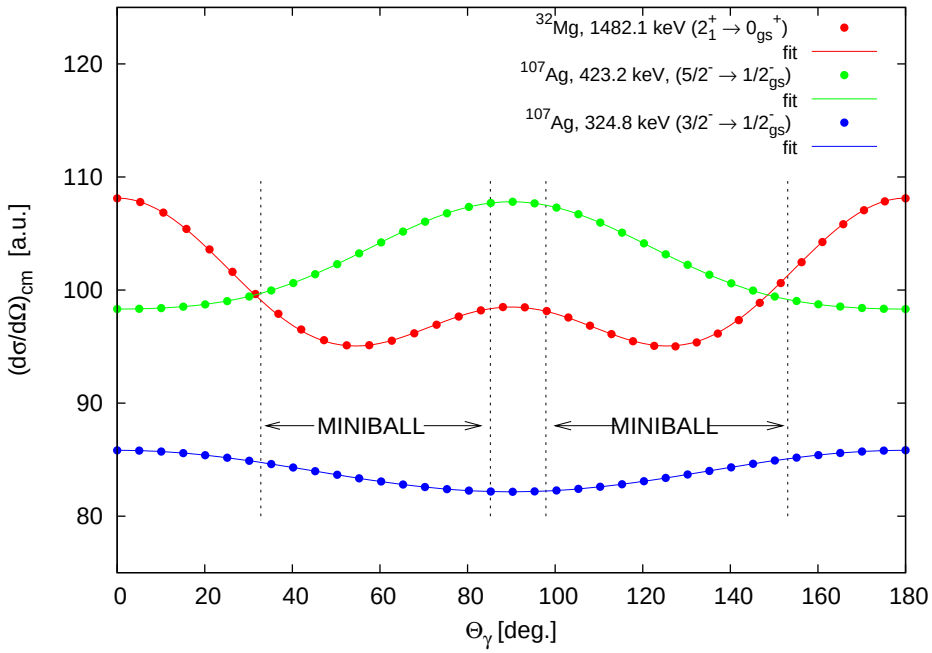

Figure 4.16: Angular distributions for de-excitation γ-rays of ^{32}Mg and ^{107}Ag in the cm-system. The distributions were fitted by Legendre polynomials. The Θ_γ-range covered by the MINIBALL array is also indicated.

beam (MeV/u)	γ-ray [keV]	target ($\frac{\text{mg}}{\text{cm}^2}$)	γ-ray [keV]	$\frac{W_\gamma^t}{W_\gamma^p}$
^{30}Mg (2.69)	1482.1 ($2_1^+ \rightarrow 0_{\text{gs}}^+$)	^{60}Ni (3.85)	1332.5 ($2_1^+ \rightarrow 0_{\text{gs}}^+$)	1.0011 (10)
^{30}Mg (2.69)	1482.1 ($2_1^+ \rightarrow 0_{\text{gs}}^+$)	^{107}Ag (4.4)	324.8 ($\frac{3}{2}_1^- \rightarrow \frac{1}{2}_{\text{gs}}^-$)	1.0095 (11)
^{30}Mg (2.69)	1482.1 ($2_1^+ \rightarrow 0_{\text{gs}}^+$)	^{107}Ag (4.4)	423.2 ($\frac{5}{2}_1^- \rightarrow \frac{1}{2}_{\text{gs}}^-$)	1.0077 (11)
^{32}Mg (2.84)	885.3 ($2_1^+ \rightarrow 0_{\text{gs}}^+$)	^{107}Ag (4.4)	324.8 ($\frac{3}{2}_1^- \rightarrow \frac{1}{2}_{\text{gs}}^-$)	1.0187 (12)
^{32}Mg (2.84)	885.3 ($2_1^+ \rightarrow 0_{\text{gs}}^+$)	^{107}Ag (4.4)	423.2 ($\frac{5}{2}_1^- \rightarrow \frac{1}{2}_{\text{gs}}^-$)	1.0176 (13)

Table 4.3: Relative angular correlation factors $\frac{W_\gamma^t}{W_\gamma^p}$ for the Coulomb excitation experiments of Exp_Sep04.

Chapter 5

Test measurements

In the present chapter the results of test measurements performed during the experimental campaigns Exp_Oct03 and Exp_Sep04 are presented. The experiments were performed with stable ^{22}Ne beams from the residual gas of the REX-EBIS. As the $B(E2)\uparrow$ value of ^{22}Ne is well known [59], the main aim of these measurements was to test the various steps in the analysis of the Coulomb excitation experiments.

5.1 Coulomb excitation of ^{22}Ne at 2.25 MeV/u

In the experimental campaign Exp_Oct03 a Coulomb excitation experiment with a stable ^{22}Ne was carried out to test the method of the relative determination of the projectile cross section as described in section 2.8. Due to the relative measurement this method is expected to be rather insensitive to systematic experimental uncertainties such as the dead time of the data acquisition system, potential uncertainties in the determination of the absolute beam intensities and uncertainties in the beam energy.

To Coulomb excite the first 2^+ state in ^{22}Ne at 1274.5 keV the 2.25 MeV/u ^{22}Ne residual gas beam from the REX-EBIS with an intensity of about 1×10^6 particles per second was incident on a 1.0 $\frac{\text{mg}}{\text{cm}^2}$ natural Ni target containing 68.08 % ^{58}Ni and 26.22 % ^{60}Ni, the rest are small amounts of ^{61,62,64}Ni. In the following sections the offline analysis steps leading to the determination of the $B(E2;\ 0^+_{\text{g.s.}} \rightarrow 2^+_1)$ value for ^{22}Ne are described in detail.

5.1.1 Event selection and determination of γ-intensities

The extraction of the projectile $B(E2)\uparrow$ value according to equation 2.31 requires a determination of the number of projectile and target γ-rays resulting from the de-excitation of the populated states. To select the coincident events and suppress background a time cut is applied in the offline analysis in addition to the hardware time window (see section 3.5). Figure 5.1 shows the time difference between γ-rays and particles. The constant background in the 4 μs time window for the event building (see section 3.5) from -2000 ns to 2000 ns consists of downscaled events. In the hardware coincidence window from about

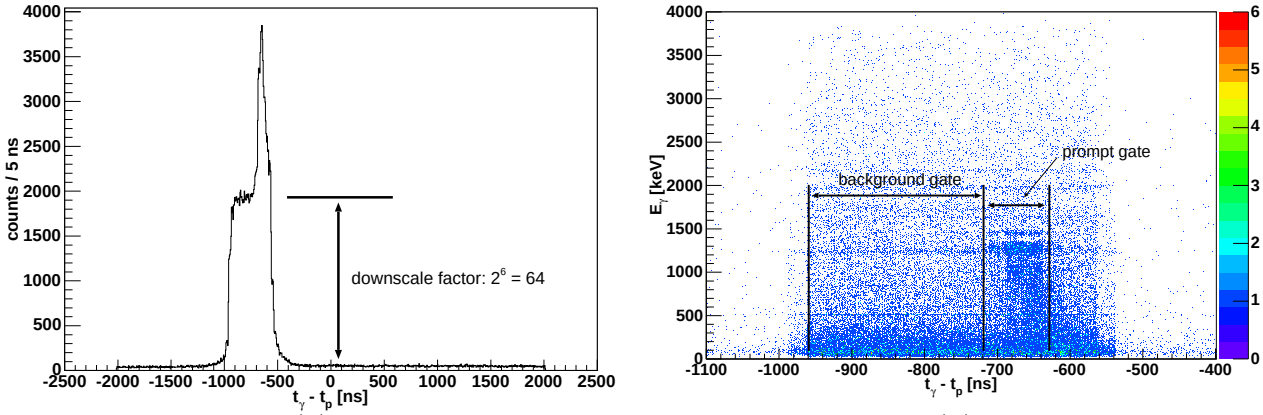

(a) (b)

Figure 5.1: Time difference of γ-rays and particles for the ^{22}Ne Coulomb excitation experiment of Exp_Oct03: (a) the hardware coincidence window (from about -1000 ns to -500 ns) and the peak with the true particle-γ-coincidences around -650 ns can be seen. (b) γ-ray energy vs. time difference (zoomed range) '$t_\gamma - t_p$': the energy dependence is due to the leading-edge-discriminator based time determination for the γ-rays. The relevant events with $E_\gamma \sim 1200$ - 1500 keV are well within the hardware time window.

-1000 ns to -500 ns the random background rises to a level of about 2000 counts since no downscaling is applied (the downscale factor in this case was $2^6 = 64$). The peak around -650 ns is due to true particle-γ-coincidences whereas all other counts are random coincidences. If the γ-ray energy is plotted versus the time difference '$t_\gamma - t_p$' with a particle required in the CD-detector (figure 5.1 (b)) it is obvious that for lower γ-energies the trigger signals arrive later and therefore larger values for '$t_\gamma - t_p$' are measured. The later γ trigger times result from the usage of the leading-edge-discriminator based timing information for the γ-rays. While some events at lower E_γ energies are lost, the interesting events in the energy range of about 1200 keV to 1500 keV are well within the gate. For the current experiment a coincidence time gate with a width of 90 ns (from -720 ns to -630 ns) and a background gate of 240 ns (from -960 ns to -720 ns) within the hardware coincidence window (see figure 5.1 (b)) was applied for the extraction of the γ-yields and the background subtraction, respectively.

In addition to the selection of particle-γ-coincidences, the analysis of Coulomb excitation experiments also requires a selection of the cm scattering angles. This is possible by using the scattering angle dependent energy measured in the CD-detector. In figure 5.2 the energy measured in the CD-detector is plotted versus the laboratory Θ_{CD} angle. The ^{22}Ne ejectiles from the Rutherford scattering on the Ni target can be identified as well as the recoiling nuclei.

In order to perform a "safe" Coulomb excitation experiment the safe distance Δ_s has to be large enough ($\Delta_s = 5.0$ - 6.5 fm, see section 2.4) to ensure the excitation process

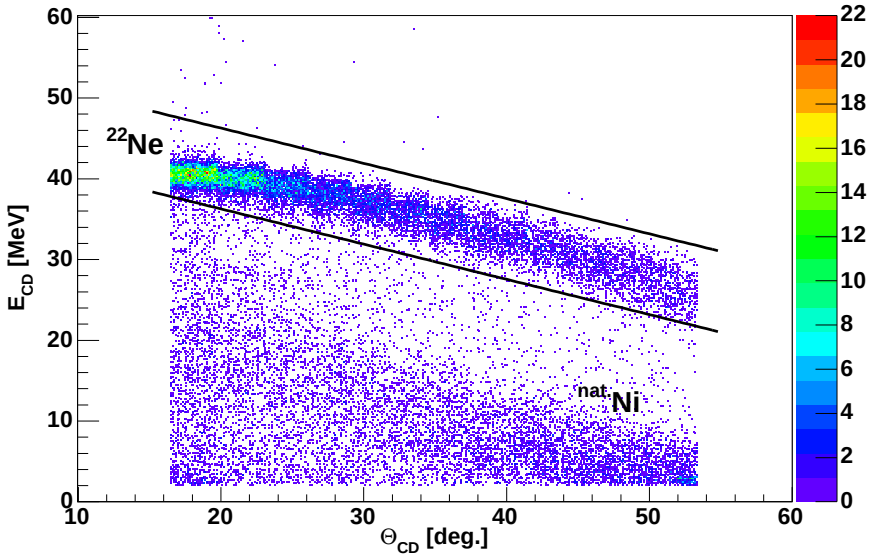

Figure 5.2: CD-energy vs. Θ_{CD}-angle (in the lab-system) for a 2.25 MeV/u ^{22}Ne beam impinging on a 1.0 $\frac{\mathrm{mg}}{\mathrm{cm}^2}$ natural Ni target. The ^{22}Ne ejectiles from the Rutherford scattering can be well separated from the recoiling Ni nuclei. The black lines indicate the cut for the selection of the ^{22}Ne nuclei.

being dominated by the electromagnetic interaction. Such Δ_s values can be obtained by restricting the cm-scattering angle to certain ranges.

For the Coulomb excitation of the 2.25 MeV/u ^{22}Ne on the natural Ni target the CD lab-range of 16.4° to 53.3° corresponds to cm-ranges of 22.6° to 71.0° and 22.4° to 70.4° when scattered from ^{58}Ni and ^{60}Ni, respectively. When transforming these ranges into safe distance ranges, Δ_s values of 7.8 fm $\leq \Delta_s \leq$ 26.8 fm and 7.7 fm $\leq \Delta_s \leq$ 26.7 fm are obtained for ^{58}Ni and ^{60}Ni, respectively. As the values are all $\geq$ 7.7 fm for all ^{22}Ne scattering angles, no additional constraining cut was applied.

The number of projectile and target γ-rays from the de-excitation after Coulomb excitation (CE) were determined by applying the time cuts mentioned above and the selection of the ^{22}Ne ejectiles in the CD-detector. Figure 5.3 shows the γ-spectra from which the intensities were extracted. The spectrum 5.3 (a) shows the uncorrected spectrum of all detected γ-rays. When the Doppler correction (DC) is performed for the detected ^{22}Ne ejectiles a peak at 1274.5 keV from the transition of the first 2^+ state to the 0^+ ground state shows up in the spectrum 5.3 (b) from which the intensity of the 1274.5 keV γ-line can be obtained. When Doppler correcting for the kinematically reconstructed (see section 4.1) Ni recoils two lines at 1332.5 keV and 1454.5 keV can be identified resulting from the $2_1^+ \rightarrow 0_{\mathrm{g.s.}}^+$ transitions in ^{60}Ni and ^{58}Ni, respectively (c). In addition, the $2_1^+ \rightarrow 0_{\mathrm{g.s.}}^+$ transition γ-line at 1172.9 keV from ^{62}Ni is observable. For a better determination of the γ-intensities of the two prominent Ni lines of ^{58}Ni and ^{60}Ni, the contribution from the ^{22}Ne γs was suppressed in spectrum (c). This was accomplished by cutting out all γ-rays that contribute to the ^{22}Ne line when the Doppler correction is applied for the ejectiles (5.3 (b)).

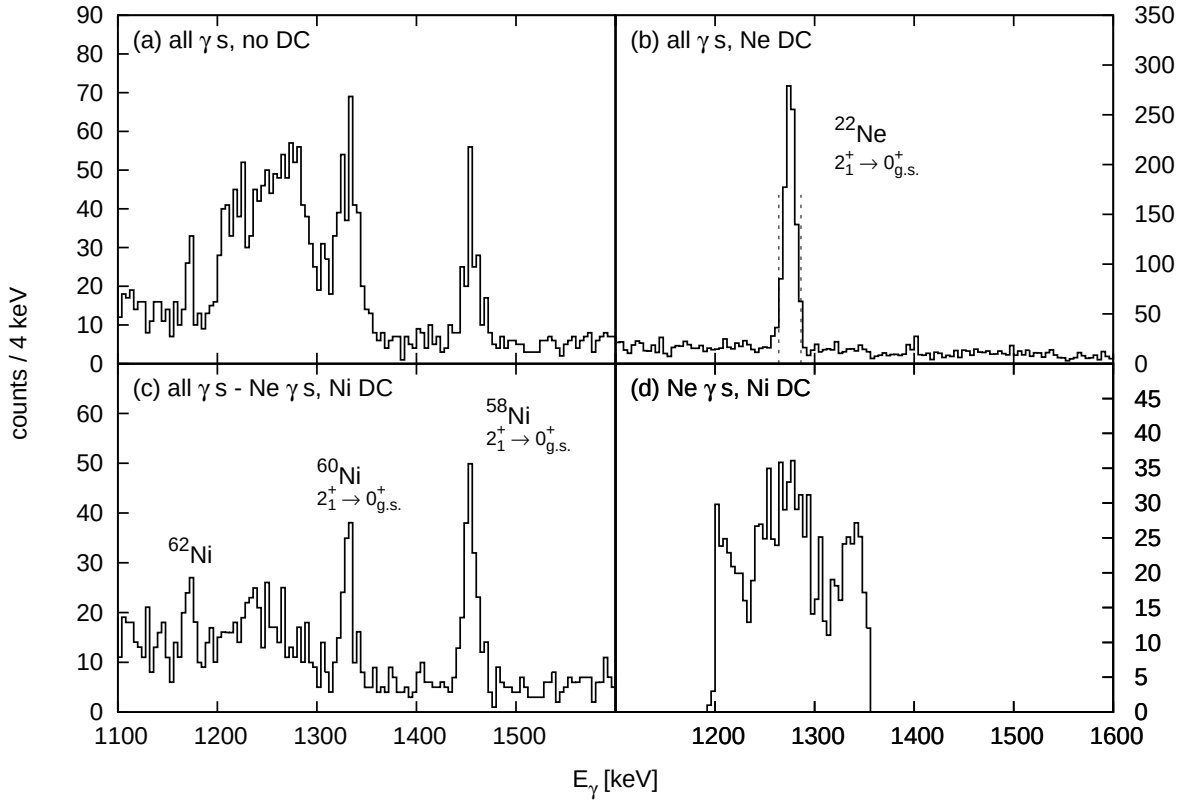

Figure 5.3: Energy spectra for the extraction of the projectile and target γ-ray yields. The uncorrected spectrum (a), the spectrum with the Doppler correction (DC) performed for the ^{22}Ne ejectiles (b) and for the target recoils (c) are shown. In (c) the ^{22}Ne contribution to the spectrum was suppressed by setting an anti-gate on the Ne line in spectrum (b) (see also the main text). In (d) the γ-events contained in the ^{22}Ne gate are Doppler corrected relating them to Ni events.

As the suppression of the ^{22}Ne γ-rays may influence the line intensities deduced for the Ni recoils, the procedure has to be checked carefully. Spectrum 5.3 (d) thus shows the ^{22}Ne γ-rays (gate width $\pm 2\,\sigma$) when the Doppler correction is performed for the Ni recoils. As these γ-rays do not overlap the ^{58}Ni peak at 1454.5 keV, the ^{58}Ni intensity deduced from spectrum 5.3 (c) is not affected. For ^{60}Ni the ^{22}Ne γ-rays do overlap the ^{60}Ni peak, but the intensity contribution can be estimated to be $\lesssim 2\,\%$ of the ^{60}Ni line intensity. Due to the low count rate the ^{62}Ni line is not considered in the extraction of the $B(E2)\uparrow$ value of ^{22}Ne. The intensities of the different γ-lines are determined by fitting the relevant spectra (see section 6.1.2 for the fitting procedure and sample fits).

5.1.2 Extraction of the $B(E2)\uparrow$ value

To determine the $B(E2)\uparrow$ value of ^{22}Ne according to equation 2.31 the theoretical Coulomb excitation cross sections are calculated with the coupled-channel code CLX [28]. For the calculation of cross sections with CLX the input of the reduced matrix elements relevant for the transitions is required.

For the Ni isotopes the reduced matrix elements for the $2_1^+ \rightarrow 0_{\text{g.s.}}^+$ transitions are those corresponding to the known lifetimes of the first 2^+ states: $t_{1/2} = 0.667\,(28)$ ps for ^{58}Ni [60] and $t_{1/2} = 0.713\,(11)$ ps for ^{60}Ni [61]. The electric quadrupole moments for both the Ni nuclei and ^{22}Ne were taken from [62]. The $B(E2)\uparrow$ value for ^{22}Ne was then determined by varying it until the experimental cross section of equation 2.31 was reproduced. When taking the weighted average of the two ^{22}Ne $B(E2)\uparrow$ values determined relative to ^{58}Ni and ^{60}Ni, a final $B(E2;\ 0_{\text{g.s.}}^+ \rightarrow 2_1^+)$ value for ^{22}Ne of 243 (26) $e^2\text{fm}^4$ is determined (see table 5.1). In the quoted error the statistical error as well as the errors of the $E2$ matrix elements for the Ni isotopes are included. A comparison of the deduced value of 243 (26) $e^2\text{fm}^4$ and the literature value of 230 (10) $e^2\text{fm}^4$ [59] shows a very good agreement within errors giving confidence into the applied procedures.

In a recent publication [63] the life times for the first 2^+ states in ^{58}Ni and ^{60}Ni were reported to be about 30 % higher than the literature values used in the above analysis. Due to the very good agreement of the deduced ^{22}Ne $B(E2)\uparrow$ with the literature value, and because these new values are in contradiction to all previously determined values, the new lifetimes thus were neglected in the current analysis.

5.2 Coulomb excitation of ^{22}Ne at 2.86 MeV/u

Also during the later experimental campaign Exp_Sep04 a test measurement was carried out with a stable ^{22}Ne beam from the residual gas of the EBIS source. The aim of this experiment was to serve as a test for the ^{107}Ag $B(E2)\uparrow$ values as a ^{107}Ag target was employed in the ^{32}Mg Coulomb excitation experiment.

In the experiment the 2.86 MeV/u ^{22}Ne beam with an intensity of about 9×10^6 particles per second was impinging on a 1.1 $\frac{\text{mg}}{\text{cm}^2}$ ^{107}Ag target (98.54 % ^{107}Ag, 1.46 % ^{109}Ag).

5.2.1 Extraction of the $B(E2)\uparrow$ value

For the determination of the $B(E2)\uparrow$ value of ^{22}Ne the scattered ejectiles were selected according to the measured energy in the CD-detector. In figure 5.4 the CD-energy is plotted versus the Θ_{CD}-angle. The scattered ^{22}Ne beam is clearly visible. Compared to the 1.0 $\frac{\mathrm{mg}}{\mathrm{cm}^2}$ natural Ni target (see figure 5.2), however, no recoiling target nuclei are detected since most recoils get stuck in the target due to their lower recoil velocity and higher energy loss due to the higher Z. As the Θ_{CD}-range for the given reaction corresponds to safe distances Δ_s of 10.3 fm $\leq \Delta_s \leq$ 35.6 fm for the ^{22}Ne ejectiles detected in the CD, no Θ-cut has to be applied to ensure a "safe" Coulomb excitation process.

In figure 5.5 the obtained γ-spectra are shown. The well known γ-line at 1274.5 keV from the $2_1^+ \rightarrow 0_{\mathrm{g.s.}}^+$ transition in ^{22}Ne is observable when Doppler correcting the spectrum for the ejectiles detected in the CD. A correction for the reconstructed ^{107}Ag recoils results in the appearance of two lines at 324.8 keV and 423.2 keV resulting from the de-excitation of the first $\frac{3}{2}^-$ and $\frac{5}{2}^-$ states to the $\frac{1}{2}^-$ ground state in ^{107}Ag, respectively. As the excited ^{107}Ag nuclei decay either at rest or at very low recoil velocities, the spectrum with the Doppler correction performed for ^{107}Ag is basically identical to the uncorrected spectrum (note that in both spectra random coincidences have been subtracted).

For the determination of the ^{22}Ne $B(E2)\uparrow$ value the $E2$ matrix elements for ^{107}Ag were calculated from $B(E2)\uparrow$ values extracted from previous Coulomb excitation experiments [64]: 0.212 (12) $e^2\mathrm{b}^2$ for the $\frac{1}{2}^-_{\mathrm{g.s.}} \rightarrow \frac{3}{2}^-_1$ transition and 0.308 (14) $e^2\mathrm{b}^2$ for the $\frac{1}{2}^-_{\mathrm{g.s.}} \rightarrow \frac{5}{2}^-_1$ transition. The quadrupole moments of the two excited states were determined from the above $B(E2)\uparrow$ values according to the rotational model (see appendix B) assuming a prolate deformation.

In figure 5.6 the low-energy part of the level scheme of ^{107}Ag is shown. The multipolarities corresponding to the two $E2$ matrix elements quoted above are marked by stars ("E2*"). The other matrix elements which were used in the calculation of the theoretical cross sections and the angular correlation factors (see section 4.5) were taken from [53]. In the determination of the γ-yields of the two ^{107}Ag transitions a correction for the transition from the 423.2 keV to the 324.8 keV state was included as well as a correction for internal conversion for the two Ag lines.

The analysis results in a final ^{22}Ne $B(E2;\ 0_{\mathrm{g.s.}}^+ \rightarrow 2_1^+)$ value of 220 (16) $e^2\mathrm{fm}^4$ which is the weighted average of the two values deduced relative to the ground state transitions from the 324.8 keV and 423.2 keV states in ^{107}Ag. The obtained value is again in very good agreement with the literature value of 230 (10) $e^2\mathrm{fm}^4$. In table 5.1 the obtained ^{22}Ne $B(E2)\uparrow$ values from the two test measurements are listed.

5.2.2 Differential cross section measurement

In order to check the experimental differential cross section and compare it with theoretical predictions, a scattering angle dependent determination of the ^{22}Ne $B(E2)\uparrow$ value and cross section was performed. The laboratory angle Θ_{CD} covered by the CD-detector was divided

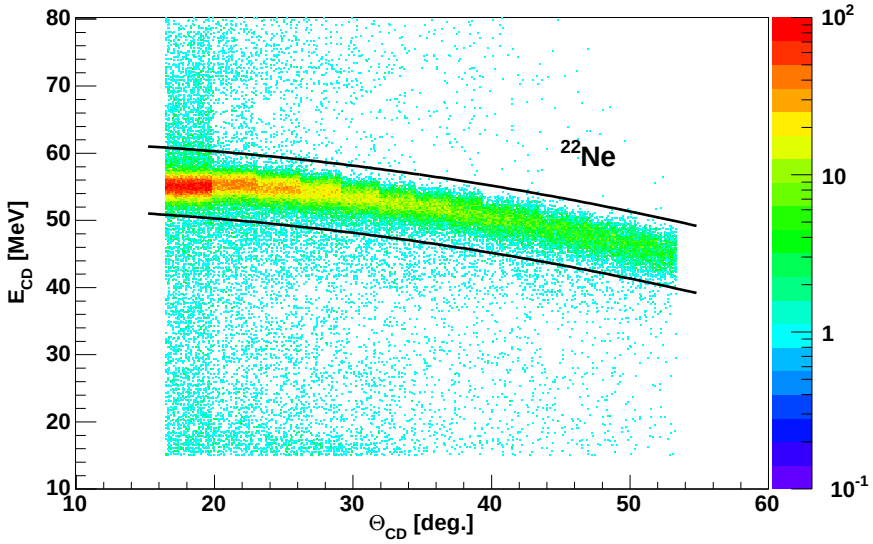

Figure 5.4: CD-energy vs. Θ_{CD} for a 2.86 MeV/u ^{22}Ne beam impinging on a 1.1 $\frac{mg}{cm^2}$ ^{107}Ag target. The ^{22}Ne ejectiles from the Rutherford scattering can be well identified. The selection of the ^{22}Ne ions is indicated by the black lines.

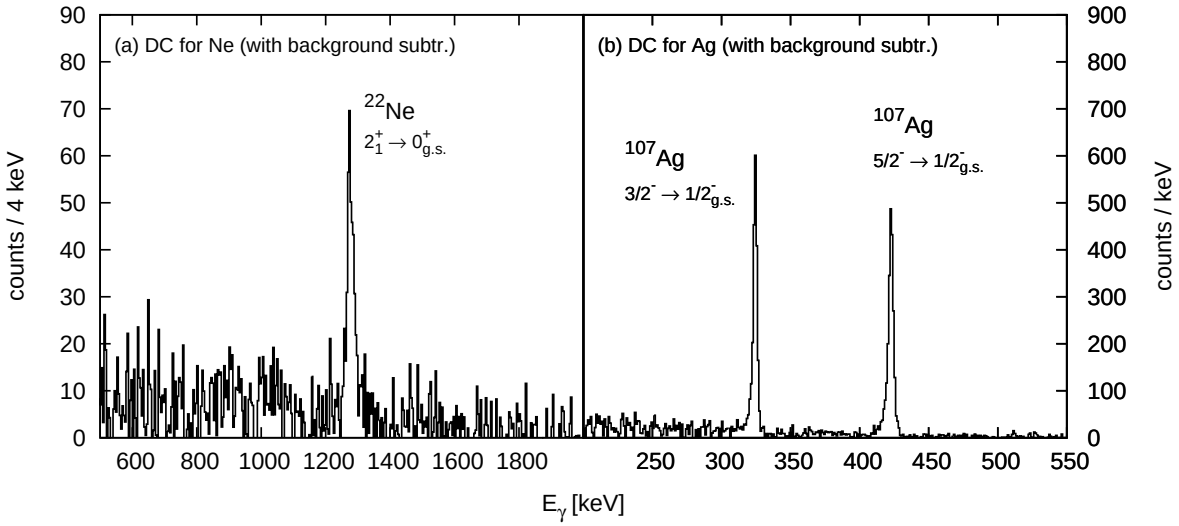

Figure 5.5: Random subtracted γ-spectra obtained with a 2.86 MeV/u ^{22}Ne beam incident on a 1.1 $\frac{mg}{cm^2}$ ^{107}Ag target with a gate on ^{22}Ne nuclei detected in the CD: when performing the Doppler correction for the detected ^{22}Ne ejectiles (a) and the reconstructed ^{107}Ag recoils (b) the γ-lines originating from the de-excitation of the excited projectile and target states show up in the spectra.

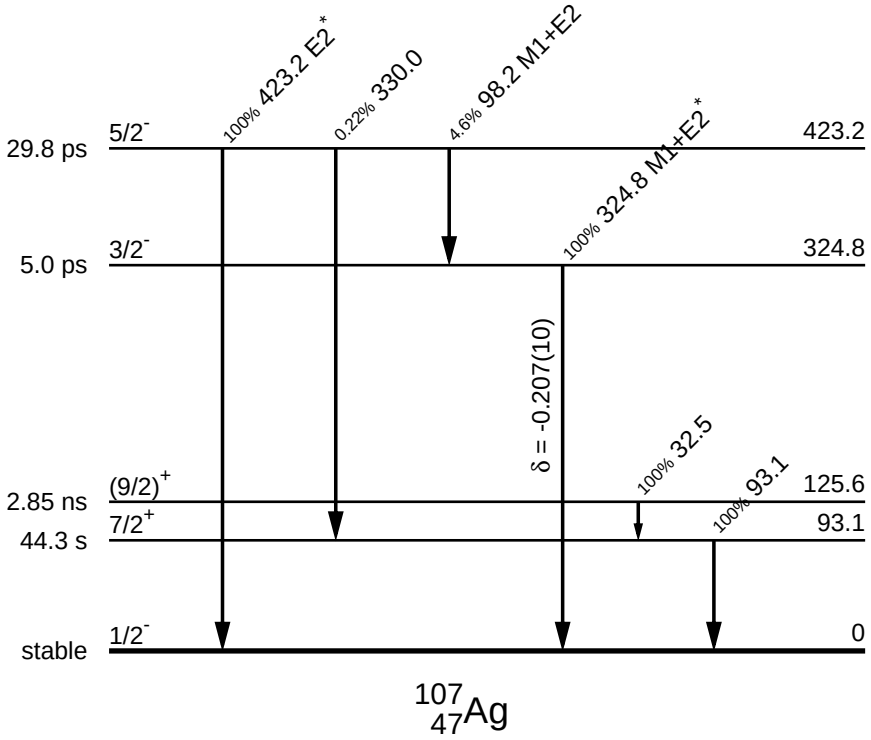

Figure 5.6: Low-energy part of the ^{107}Ag level scheme: the level energies in keV (right-hand side) as well as the spin-parity values and the half lifes (left-hand side) are shown. For the transitions the relative intensity (normalized to 100 % for the most intense transition from the given level), the γ-ray transition energy and the multipolarities are displayed [53].

beam en. [MeV/u]	target, thick. [$\frac{\text{mg}}{\text{cm}^2}$]	abun-dance	normalization transition	$B(E2)\uparrow$ [e^2fm^4]	total error [e^2fm^4]
2.25	$^{\text{nat.}}$Ni, 1.0	^{58}Ni: 68.08 %	^{58}Ni, $0^+_{\text{g.s.}} \rightarrow 2^+_1$	235.1	28.1
”	”	^{60}Ni: 26.22 %	^{60}Ni, $0^+_{\text{g.s.}} \rightarrow 2^+_1$	295.9	74.8
			weighted average	242.5	26.4
2.86	^{107}Ag, 1.1	^{107}Ag: 98.54 %	^{107}Ag, $\frac{1}{2}^-_{\text{g.s.}} \rightarrow \frac{3}{2}^-_1$	217.0	22.7
”	”	”	^{107}Ag, $\frac{1}{2}^-_{\text{g.s.}} \rightarrow \frac{5}{2}^-_1$	222.5	21.4
			weighted average	219.9	15.6

Table 5.1: Summary of determined ^{22}Ne $B(E2)\uparrow$ values from the test measurements on a natural Ni and an enriched ^{107}Ag target.

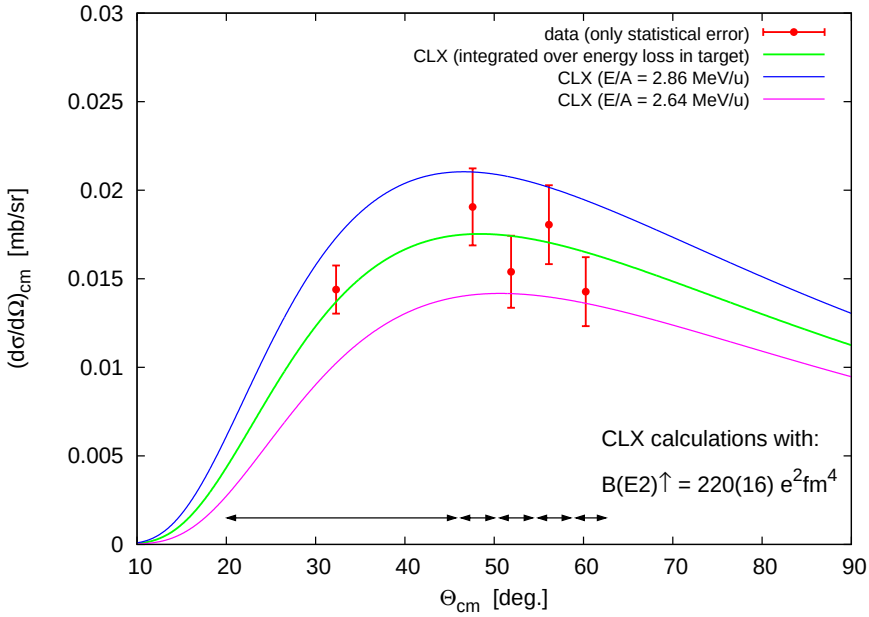

Figure 5.7: Differential cross section $\left(\frac{d\sigma}{d\Omega}\right)_{\mathrm{cm}}$ for the Coulomb excitation of 2.86 MeV/u ^{22}Ne projectiles on the ^{107}Ag target: the different theoretical predictions correspond to calculations where an integration of the energy loss in the target was performed (green line), with the initial projectile energy (2.86 MeV/u) and with energy loss over the full target assumed (2.64 MeV/u). The different Θ_{cm}-bins are indicated by the arrows.

in five sub-ranges and the differential cross section $\left(\frac{d\sigma}{d\Omega}\right)_{\mathrm{cm}}$ in the cm-system was determined for the population of the first 2^+ state of ^{22}Ne as a function of Θ_{cm}.

In figure 5.7 the measured differential cross section is compared to different CLX calculations assuming a ^{22}Ne $B(E2)\uparrow$ value of 220 (16) $e^2\mathrm{fm}^4$. The calculations were performed at different projectile energies corresponding to excitations at different target depths. Calculations at projectile energies of 2.86 MeV/u (beam energy) and 2.64 MeV/u (beam energy at the end of the target) are shown as well as a calculation where the cross section was integrated over the energy loss in the target. It follows from figure 5.7 that the experimental cross section is in good agreement with the target integration calculation (green line).

5.2.3 Calibration of ^{107}Ag $E2$ matrix elements

As discussed in section 5.2.1, the extracted $B(E2)\uparrow$ value for ^{22}Ne is consistent with the literature value of 230 (10) $e^2\mathrm{fm}^4$ which is known with a precision of less than 5 %. The present ^{22}Ne Coulomb excitation experiment can therefore also be regarded as a measurement of the two ^{107}Ag $E2$ matrix elements. Therefore the analysis was repeated assuming the literature $B(E2)\uparrow$ value for ^{22}Ne and adjusting the $B(E2)\uparrow$ values for the two transitions in ^{107}Ag.

	method	$B(E2)\uparrow$ ($\frac{1}{2}^-_{\text{g.s.}} \rightarrow \frac{3}{2}^-_1$) [$e^2$b^2]	$B(E2)\uparrow$ ($\frac{1}{2}^-_{\text{g.s.}} \rightarrow \frac{5}{2}^-_1$) [$e^2$b^2]
(a)	previous CE exp. [64]	0.2120 (120)	0.3080 (140)
(b)	^{22}Ne calibration	0.2218 (126)	0.3222 (146)
(c)	average of (a) and (b)	0.2167 (87)	0.3148 (101)
(d)	from life times [64]	0.2535 (241)	0.3893 (272)

Table 5.2: ^{107}Ag $B(E2)\uparrow$ values for the $\frac{1}{2}^-_{\text{g.s.}} \rightarrow \frac{3}{2}^-_1$ and $\frac{1}{2}^-_{\text{g.s.}} \rightarrow \frac{5}{2}^-_1$ transitions.

Table 5.2 collects the present knowledge of the $B(E2)\uparrow$ values of the two ^{107}Ag transitions. By taking the weighted average of the $B(E2)\uparrow$ values from the previous Coulomb excitation experiments (a) and the values obtained by our ^{22}Ne calibration (b), the values in line (c) are obtained. It should be noted that the average values differ only by about 2 % from the values in (a), but are more precise. The values of (c) will then be used for the determination of the $B(E2)\uparrow$ value of ^{32}Mg (see section 6.3). The $B(E2)\uparrow$ values calculated from the known life times (see line (d) in table 5.2) were neglected since they are considerably less precise and even inconsistent with the directly measured $B(E2)\uparrow$ values.

Chapter 6

Analysis and Results

In the following chapter the analysis and the results of the Coulomb excitation experiments for the neutron-rich Mg isotopes ^{30}Mg and ^{32}Mg are presented. The main goal of the experiments was the determination of the $B(E2;\ 0^+_{\text{g.s.}} \rightarrow 2^+_1)$ values for ^{30}Mg and ^{32}Mg by low-energy "safe" Coulomb excitation.

6.1 Coulomb excitation of ^{30}Mg at 2.25 MeV/u

The main experiment in the experimental campaign Exp_Oct03 was the Coulomb excitation of ^{30}Mg with the aim to determine the ^{30}Mg $B(E2;\ 0^+_{\text{g.s.}} \rightarrow 2^+_1)$ value for the first time in a low-energy "safe" Coulomb excitation experiment. Due to the applied technique the experiment should result in a model-independent $B(E2)\uparrow$ value for the short-lived radioactive ^{30}Mg nucleus which has a half life of only 335 ms.

In order to Coulomb excite the first 2^+ level in ^{30}Mg at 1482.2 keV the 2.25 MeV/u ^{30}Mg^{7+} beam provided by REX-ISOLDE with an intensity of about 2×10^4 particles per second was incident on 1.0 $\frac{\text{mg}}{\text{cm}^2}$ natural Ni target. Data were taken during a total measuring time of about 3 days. Due to the fast release of the ^{30}Mg ions from the ISOLDE target (cf. figure 4.13) a global gate is used in the analysis and only events in the first 1.2 s after the T1 proton pulses are considered. In the following sections the different analysis steps for the determination of the $B(E2;\ 0^+_{\text{g.s.}} \rightarrow 2^+_1)$ value of ^{30}Mg are described in detail.

6.1.1 Purity of the ^{30}Mg beam

For the determination of the ^{30}Mg beam purity for Exp_Oct03 all of the methods described in section 4.4.2 could be applied except the analysis of the data from the ΔE-detectors since these detectors were only installed in 2004. In table 6.1 the results of the different methods are listed. An adopted value of $N(^{30}\text{Al})_{\text{total}} = 6.53\,(23)\,\%$ was obtained which is the weighted average of all applied methods.

In addition, in this experiment also the Coulomb excitation of the 244 keV state of ^{30}Al was investigated. In figure 6.1 the observed transition line is shown in the upper spectrum

	method	$N(^{30}\mathrm{Al})_{\mathrm{decay}}$ [%]	$N(^{30}\mathrm{Al})_{\mathrm{ISOLDE}}$ [%]	$N(^{30}\mathrm{Al})_{\mathrm{total}}$ [%]
(a)	breeding	4.49 (22)		
(b)	LASER on/off		4.74 (86)	
(c)	release curve		2.01 (7)	
	weighted average	4.49 (22)	2.03 (7)	6.52 (23)
(d)	β decay			7.7 (22)
	adopted value			6.53 (23)

Table 6.1: Amount of ^{30}Al in the beam deduced from different methods for the ^{30}Mg beam of Exp_Oct03 ($0 \leq T_{\mathrm{p}} \leq 1.2\,\mathrm{s}$).

(see next section for the Coulomb excitation spectrum of ^{30}Mg plotted in the lower panel of figure 6.1). When assuming a $B(E2)\uparrow$ value for the transition from the 3^+ ground state to the assumed 2^+ state at 244 keV of $B(E2)\uparrow = 3.1$ W.u. (see appendix C.2 for the definition of the Weisskopf units W.u.) taken from [65] (shell model calculation), the ^{30}Al amount in the beam is estimated to be $N(^{30}\mathrm{Al})_{\mathrm{total}} = 9.5\,(19)\,\%$ which is consistent with the average value of $6.53\,(23)\,\%$ resulting from the other methods.

When correcting the γ-yield from the target excitation of the ^{30}Al contamination, one additional aspect has to be considered: due to higher Z of $^{30}_{13}$Al compared to $^{30}_{12}$Mg the cross section for the excitation of the Ni target nuclei is lower for Al due to a higher energy loss in the target and a larger distance of closest approach (see section 2.1). In the present case (beam energy of 2.25 MeV/u and Ni target thickness of 1.0 $\frac{\mathrm{mg}}{\mathrm{cm}^2}$) the cross section for the Ni-excitation initiated by Al is about 25 % lower as compared to that of Mg resulting in a reduced value for the *effective* contamination.

6.1.2 Extraction of the $B(E2;\ 0^+_{\mathrm{g.s.}} \rightarrow 2^+_1)$ value

In a first step the scattered ^{30}Mg ions and the recoiling Ni target nuclei were identified via the energy measured in the CD-detector. In figure 6.2 the CD-energy is plotted versus the scattering angle Θ_{CD}. The plot only contains events which are coincident with a γ-ray in the MINIBALL array. For the Mg ejectiles detected in the CD the Θ_{CD}-range of 16.4° to 53.3° corresponds to Δ_s values of $6.1\,(6.0)\ \mathrm{fm} \leq \Delta_s \leq 22.6\,(22.5)$ fm when scattering from ^{58}Ni (^{60}Ni). For a backward scattering of the Mg nuclei, i.e. for Ni recoils detected in the CD, safe distances of $3.3\,(3.1)\ \mathrm{fm} \leq \Delta_s \leq 7.0\,(6.8)$ fm for ^{58}Ni (^{60}Ni) are calculated.

When gating on the ^{30}Mg ejectile respectively the Ni recoils and performing a Doppler correction for both detected and reconstructed particles, the four spectra displayed in figure 6.3 are obtained. Performing the Doppler correction for ^{30}Mg ions the γ-line from the transition of the first 2^+ state in ^{30}Mg to the 0^+ ground state is clearly visible for events with Mg (a) or Ni (b) detected in the silicon counter. Vice versa, the $2^+_1 \rightarrow 0^+_{\mathrm{g.s.}}$ transitions of the three most abundant Ni isotopes in the target, i.e.^{58}Ni, ^{60}Ni and ^{62}Ni, are observed when the Doppler shift correction is performed for Ni recoils. In addition to these

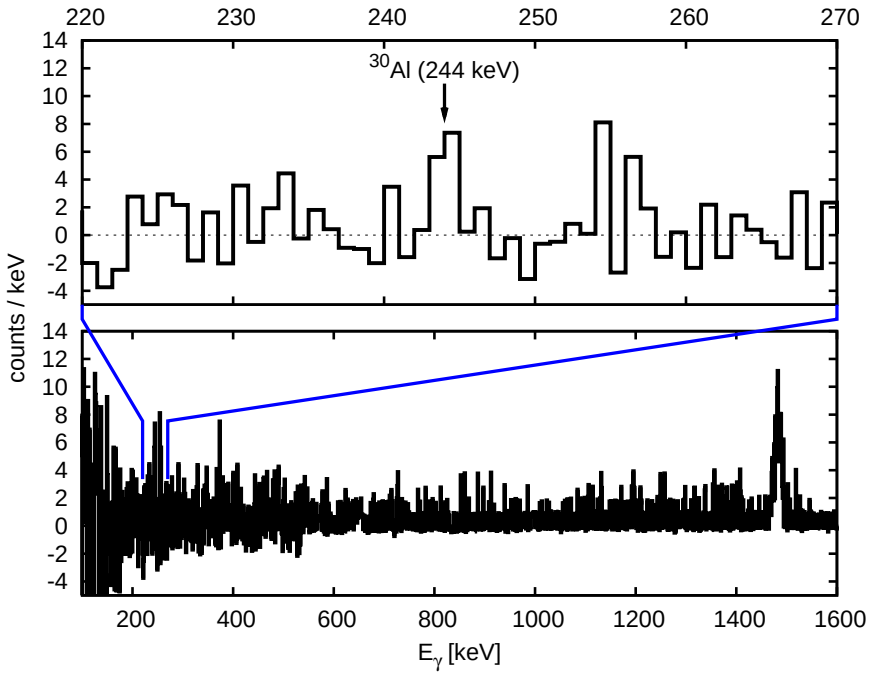

Figure 6.1: Random-subtracted γ-spectra showing the Coulomb excitation of the 244 keV state in ^{30}Al for Exp_Oct03. The spectrum shown in the upper panel is a cut-out from the γ-spectrum shown in the lower panel applying a Doppler correction for projectile excitation. Besides the Coulomb excitation of ^{30}Mg (lower panel) the γ-line resulting from the Coulomb excitation of the isobaric contaminant ^{30}Al is visible.

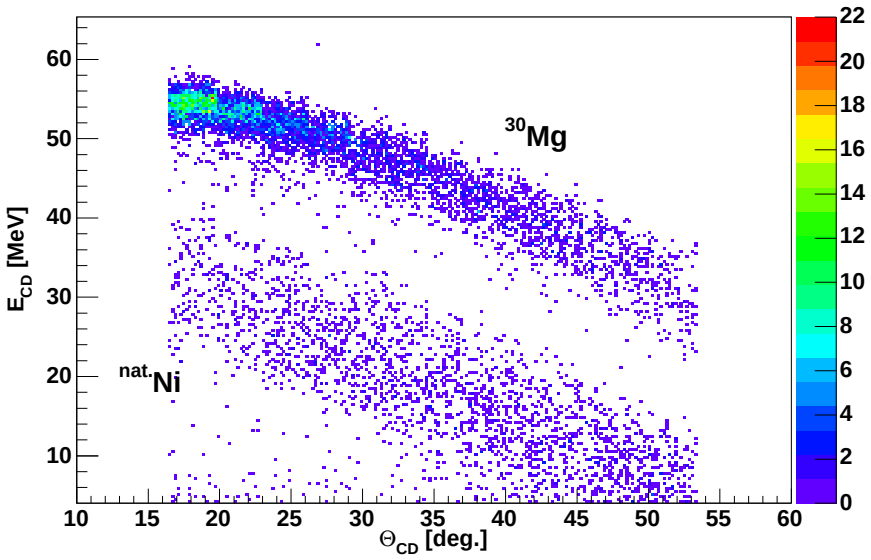

Figure 6.2: CD-energy vs. Θ_{CD} for the 2.25 MeV/u ^{30}Mg beam incident on the 1.0 $\frac{mg}{cm^2}$ natural Ni target for events with at least one γ-ray detected in the MINIBALL array. The ^{30}Mg ejectiles are well separated from the recoiling Ni nuclei due to their higher energy at a given laboratory scattering angle.

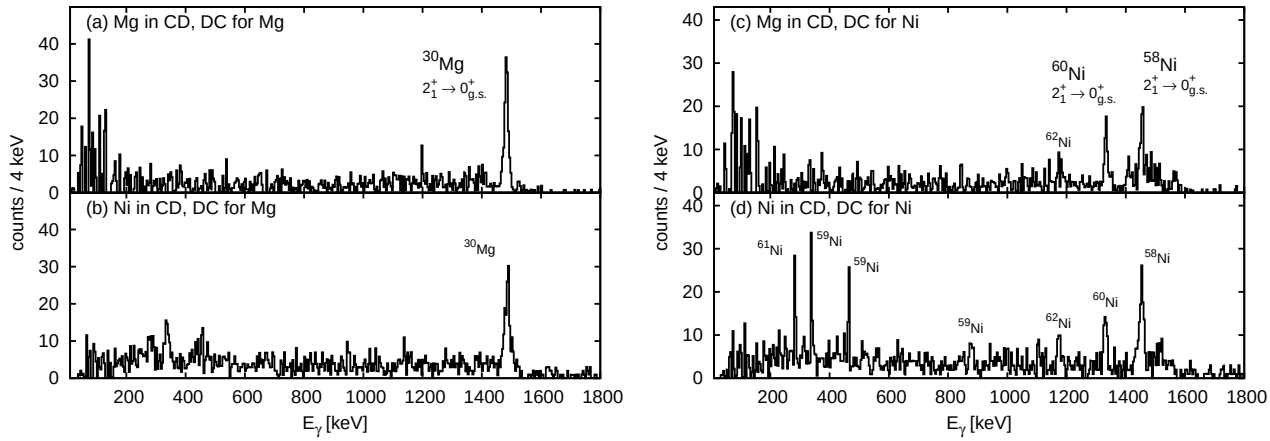

Figure 6.3: Doppler corrected γ-spectra for 2.25 MeV/u ^{30}Mg projectiles incident on a 1.0 $\frac{mg}{cm^2}$ natural Ni target: when the Doppler correction is performed assuming ^{30}Mg to be the γ-emitting nucleus, the spectra shown in (a) and (b) are obtained in the case of (a) the ejectiles and (b) the recoils are detected in the CD. Panels (c) and (d) display the corresponding spectra performing the Doppler correction for Ni recoils when (c) Mg and (d) Ni ions are detected in the particle detector. In (d) 1n-transfer lines leading to states in ^{59,61}Ni are apparent (see text).

three transitions, γ-rays from 1n-pickup reactions of ^{58,60}Ni show up in spectrum (d) for backward scattering. Although the distance between the nuclear surfaces of the colliding nuclei in the backscattering case is still larger than 3.0 fm (see above), the surprisingly strong occurrence of the transfer channels results from the extensive tail part of the neutron density distribution of ^{30}Mg which is characteristic for neutron-rich nuclei (see e.g. [66]).

Therefore, only the data from the "safe" Coulomb excitation with Mg detected in the CD were analyzed to determine the $B(E2)\uparrow$ value of ^{30}Mg. These events correspond to surface distances for Mg and Ni of more than 6.0 fm; no transfer lines can be observed in the corresponding spectrum 6.3 (c).

Determination of γ-yields

When extracting the γ-intensities from the Doppler corrected spectra two problems have to be overcome: i) due to the Doppler broadening the observed γ-energies from the decay of ^{58}Ni (1454.5 keV) and ^{30}Mg (1482.2 keV) are to some extent superimposed, ii) the low statistic of the γ-spectra. The first problem was minimized by suppressing those events in the spectrum Doppler corrected for Ni emitters which contribute to the full energy peak ($\pm 2\,\sigma$) of the ^{30}Mg transition in the spectrum Doppler corrected for Mg emitters (see also section 5.1.1). Referring to the second problem several tests were performed concerning the exact determination of the peak area for given low-statistic spectra. By testing different procedures for artificially created spectra with known peak areas, very good agreements of nominal and determined peak areas were found when assuming Poisson-statistics and taking as bin errors the square root of the value of the fit function $f(x)$ at the bin position x ($\sigma = \sqrt{f(x)}$) and not the usual square root of the count rate ($\sigma = \sqrt{N}$) which is only a good approximation if the number of counts is 10 or higher [67]. As this procedure requires a "real" count rate in all fitted bins the spectra without random-γ subtraction had to be fitted and therefore the background spectra had to be checked for possible contributions influencing the γ-yields from Coulomb excitation.

In figure 6.4 the two spectra used for the determination of the γ-yields of the Mg and Ni transition lines are shown. In contrast to the fit of the Mg line (a) the Ni fit also includes γ-rays observed in the random background spectrum. The ^{30}Si γ-ray from β-decay and the ^{40}K γ were fitted separately in the random spectrum (not shown) with Doppler correction performed for Ni. As the Ni recoils decay at rest or at very low recoil velocities, the ^{30}Si and ^{40}K γ-lines are (almost) not Doppler broadened and therefore can be identified as sharp lines in the Ni Doppler corrected random spectrum. The areas of the two random γ-lines were then scaled due to the different time windows for the coincident and the background gate and then included in the Ni fit. Due to the suppression of the Mg γs in spectrum (b) a small correction for ^{58}Ni had to be performed (cf. section 5.1.1 and figure 5.3) resulting in a final number of ^{58}Ni de-excitation γ-rays of $N_\gamma(^{58}\mathrm{Ni}) = 50.2 \pm 8.0$ (compared to the value of $N_\gamma(^{58}\mathrm{Ni}) = 50.2 \pm 6.4$ from the fit of figure 6.4 (b)).

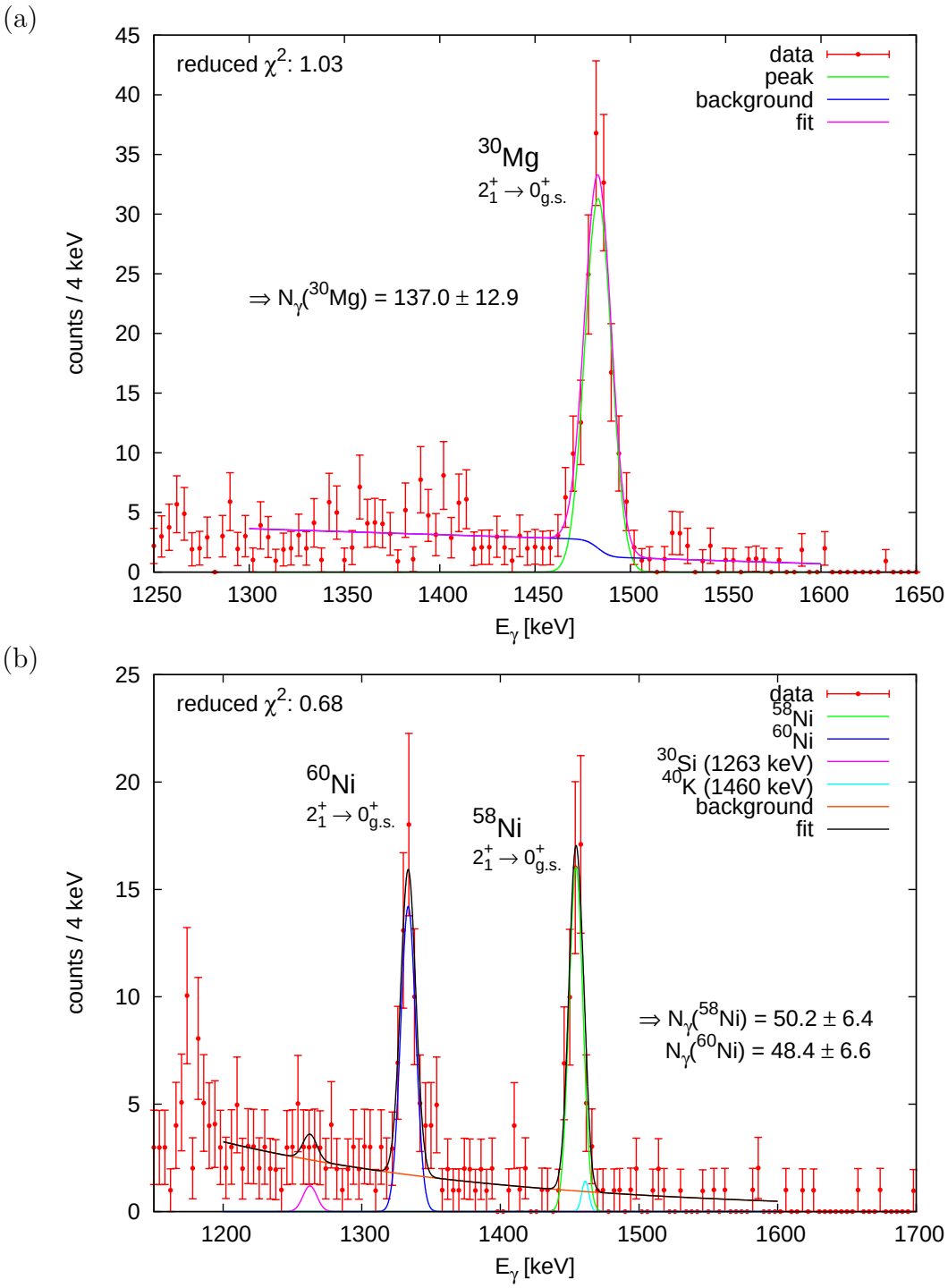

Figure 6.4: Doppler corrected spectra used in the determination of the γ-yields for the Mg and Ni transitions (no randoms have been subtracted). The fit of the 1482.2 keV ^{30}Mg γ (a) and the two Ni γs (b) are shown. The ^{30}Si γ-ray at 1263.2 keV from the β-decay and the ^{40}K 1460 keV line which were identified and fitted in the background spectrum were also included in the fit of the Ni γ-rays. Events leading to the Mg peak in (a) were suppressed in spectrum (b).

$B(E2)\uparrow$ determination

To determine the $B(E2;\ 0^+_{\text{g.s.}} \rightarrow 2^+_1)$ value of ^{30}Mg the resulting Ni γ-yields were corrected with the deduced effective beam contamination. The ^{30}Mg $B(E2)\uparrow$ value was then extracted with the aid of equation 2.31.

For the calculation of the Coulomb excitation cross sections the coupled-channel code CLX [28] was used. To integrate over the energy loss in the target, the target was divided in a certain number of sub-ranges (typically 10), then the energy loss of the projectile up to the middle of the corresponding target slices was calculated and the cross section calculation was performed for this beam energy. The sum of the energy-loss weighted cross sections obtained in the sub-ranges was then formed (see appendix D for a sample CLX calculation). The $B(E2)\uparrow$ value of ^{30}Mg was then varied until the experimental cross section could be reproduced (cf. equation 2.31).

For ^{30}Mg a quadrupole moment according to the rotational model was assumed (see section 7.1.1 for the influence of the choice of the quadrupole moment on the deduced $B(E2)\uparrow$ values). The analysis resulted in a $B(E2;\ 0^+_{\text{g.s.}} \rightarrow 2^+_1)$ value for ^{30}Mg of $241 \pm 30\,(\text{stat}) \pm 8\,(\text{sys}) = 241\,(31)\ e^2\text{fm}^4$ [68, 69]. While the statistical error accounts for the uncertainties in the γ-transition peak areas, the systematical error includes the uncertainties in the $B(E2)\uparrow$ values of the two Ni isotopes, the uncertainty of the beam contamination and an estimated contribution of 2 % from the γ-ray angular distributions.

6.1.3 Time dependence

To examine the independence of the extracted ^{30}Mg $B(E2)\uparrow$ value on the size and location of the analysis window after the T1 pulses, the time range of $0 \leq T_{\text{p}} \leq 1.2$ s used in the analysis was subdivided in several non-equidistant ranges and the number of Mg and Ni γs for each of the subranges was determined (see figure 4.13 for the distribution of the events relative to the last T1 pulse). In figure 6.5 the resulting $B(E2)\uparrow$ values for ^{30}Mg are shown where only the (dominating) statistical errors are included. Due to the low count rates in some of the T1-bins for the Mg- and Ni-intensities rather large errors are obtained. The individual $B(E2)\uparrow$ values are in good agreement within their errors and with the overall value of 241 (30) $e^2\text{fm}^4$. No systematic dependence of the $B(E2)\uparrow$ result on the width and location of the analysis window can be seen.

In addition to the T_{p} dependence, the resulting ^{30}Mg $B(E2)\uparrow$ value with respect to the beam particle distribution during the EBIS pulses was examined. Figure 6.6 shows the distribution of the particles during the EBIS pulse for the ^{30}Mg beam in Exp_Oct03. Most of the particles arrive at the MINIBALL target within a time window of 50 - 100 μs. When the ^{30}Mg $B(E2)\uparrow$ value is determined for certain time gates during the EBIS pulse, the results shown in figure 6.7 are obtained. As in the case of the T_{p}-dependence some of the data points are characterized by large error bars due to low statistics, but again no systematic effects are observable within the errors.

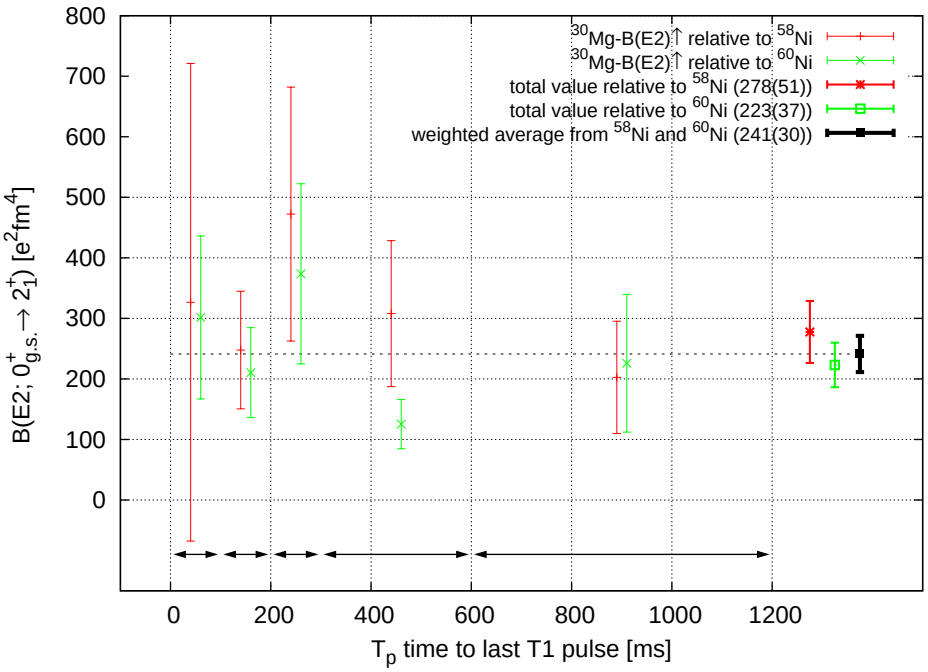

Figure 6.5: The extracted ^{30}Mg $B(E2)\uparrow$ value as a function of the time T_p after the last T1 proton pulse. Most of the data points are within the error bars in good agreement with the average $B(E2)\uparrow$ value of 241 (30) $e^2\mathrm{fm}^4$. The different T_p-bins are indicated by the arrows.

6.2 Coulomb excitation of ^{30}Mg at 2.69 MeV/u

After the energy upgrade of the REX-ISOLDE accelerator to beam energies of 3.0 MeV/u (see section 3.2.2) in 2004, the ^{30}Mg Coulomb excitation experiment of the experimental campaign Exp_Sep04 could be performed at higher beam energies compared to 2003. The higher beam energies lead to increased Coulomb excitation cross sections with the drawback of decreased "safe" distances of the nuclear surfaces for the same projectile target combinations.

The aim of the ^{30}Mg Coulomb excitation in 2004 was to confirm the measurement of 2003 at an increased statistics resulting in a lower statistical uncertainty in the determined $B(E2;\ 0^+_{\mathrm{g.s.}} \rightarrow 2^+_1)$ for ^{30}Mg. The experiment was performed with a 2.69 MeV/u ^{30}Mg ($q = 7^+$) beam with an intensity of about 1×10^5 particles per second. The natural Ni target ($1.0\ \frac{\mathrm{mg}}{\mathrm{cm}^2}$) of 2003 was replaced by an enriched (99.3 %) ^{60}Ni to suppress the superposition of the projectile and target de-excitation γ-rays. To maximize the yield a target with a thickness of $3.85\ \frac{\mathrm{mg}}{\mathrm{cm}^2}$ was used. The total measuring time was about 2 days. As in the analysis of the ^{30}Mg Coulomb excitation experiment of Exp_Oct03 only events within the first 1.2 s after the T1 proton pulses are considered. The analysis steps as well as the determination of the differential cross section for ^{30}Mg are described in the following sections.

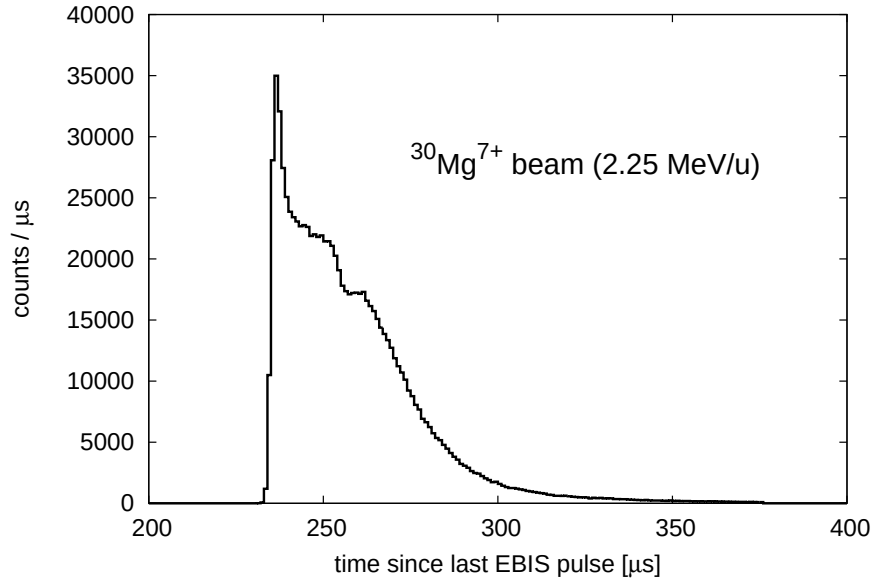

Figure 6.6: Time structure of the beam pulse extracted from the EBIS for the ^{30}Mg beam of Exp_Oct03. All particles are contained within a time window of about 150 μs.

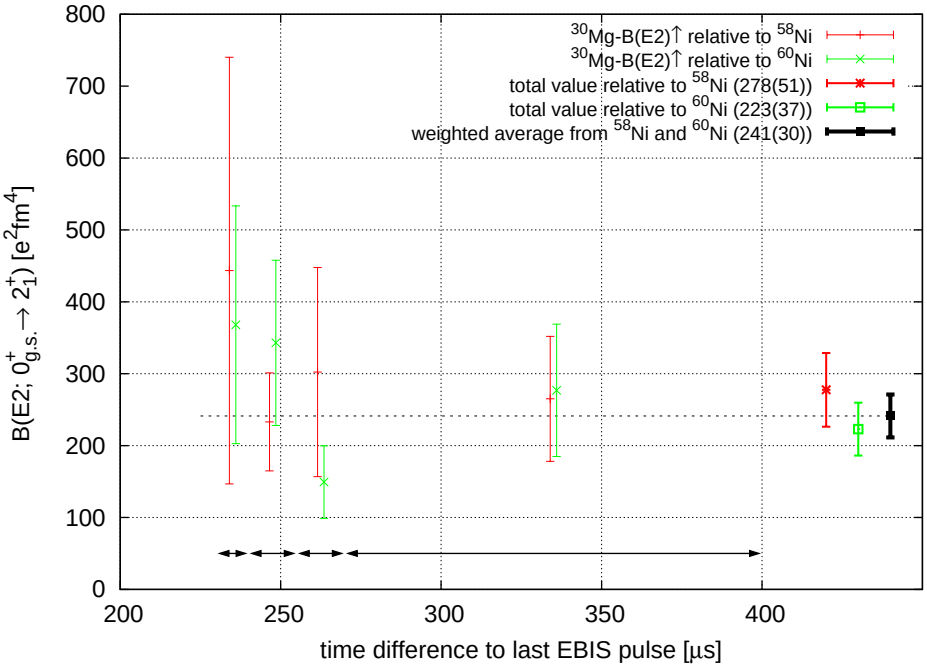

Figure 6.7: The extracted ^{30}Mg $B(E2)\uparrow$ value as a function of time after the EBIS pulse. The individual $B(E2)\uparrow$ values (statistical errors only) in the different time sub-ranges (indicated by the arrows) are consistent with the ^{30}Mg $B(E2)\uparrow$ value of 241 (30) e^2fm^4.

	method	$N(^{30}\mathrm{Al})_{\mathrm{decay}}$ [%]	$N(^{30}\mathrm{Al})_{\mathrm{ISOLDE}}$ [%]	$N(^{30}\mathrm{Al})_{\mathrm{total}}$ [%]
(a)	breeding	5.28 (47)		
(b)	LASER on/off		12.73 (71)	
(c)	release curve		14.98 (369)	
	weighted average	5.28 (47)	12.81 (70)	18.09 (84)
(d)	β-decay			17.32 (270)
	adopted value			18.02 (80)

Table 6.2: Amount of ^{30}Al in the beam deduced from different methods for Exp_Sep04.

6.2.1 Purity of the ^{30}Mg beam

In a first step the purity of the ^{30}Mg beam was determined. Due to the rather high beam intensity and the installation of the ΔE-detectors close to the beam axis (see section 3.4), the electronics was not able to cope with the resulting high count rates (see [55]). An analysis of the ΔE-data providing reliable results was therefore not possible. The obtained beam purities deduced from the other methods are listed in table 6.2. When taking the weighted average of all different methods a value of $N(^{30}\mathrm{Al})_{\mathrm{total}} = 18.0\,(8)\,\%$ was obtained which is considerably higher than in the experimental campaign Exp_Oct03. This is likely due to the slightly different operation temperature of the ISOLDE production target.

6.2.2 Extraction of the $B(E2;\ 0^+_{\mathrm{g.s.}} \rightarrow 2^+_1)$ value

The identification of scattered projectiles and recoiling ions was again accomplished by using the scattering angle dependent energy measured in the CD-detector. In figure 6.8 the energy in the CD-detector is plotted versus the Θ_{CD} angle. The spectrum only contains events which are in coincidence with a γ-ray detected in the MINIBALL array. In addition to the broad contribution from the scattered ^{30}Mg ejectiles also recoiling ^{60}Ni ions with energies below about 10 MeV can be observed. The Θ_{CD}-range of 16.4° to 53.3° corresponds to distances Δ_s between the nuclear surfaces of 3.8 fm $\leq \Delta_s \leq$ 17.6 fm when the Mg ions are detected by the CD-detector and to 1.3 fm $\leq \Delta_s \leq$ 4.3 fm for the recoiling Ni ions. In order to perform a "safe" Coulomb excitation experiment only events with ^{30}Mg in the CD-detector were chosen and to ensure surface distances of $\Delta_s \geq 6.5$ fm the allowed scattering angle range was restricted to Θ_{CD}-values of $\Theta_{\mathrm{CD}} \leq 36.6°$.

When gating on the Mg ejectiles in the CD with this scattering angle cut the spectra of figure 6.9 are obtained. The $2^+_1 \rightarrow 0^+_{\mathrm{g.s.}}$ transitions in ^{30}Mg (a) and ^{60}Ni (b) are observable. The broad contribution to the Mg spectrum results from the wrongly Doppler corrected Ni γ-rays, whereas in the Ni spectrum the wrongly Doppler corrected Mg de-excitation photons are visible as a broad bump. The shape of the ^{60}Ni transition line in (b) can be explained as follows: when the ^{60}Ni recoils are stopped in the thick target and decay at rest the γ-rays are not Doppler shifted resulting in a narrow contribution to the peak. If the Coulomb excitation reaction takes place towards the end of the target then the Ni

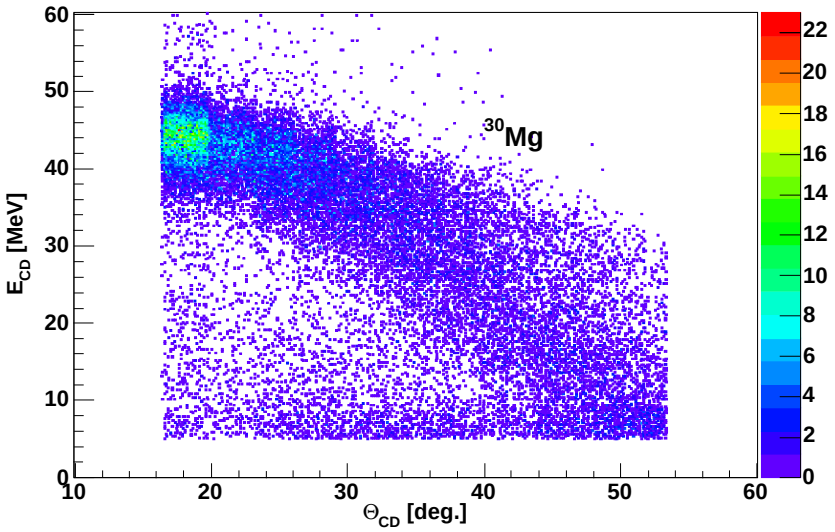

Figure 6.8: CD-energy vs. Θ_{CD} for a 2.69 MeV/u ^{30}Mg beam impinging on an isotopically enriched ^{60}Ni target. The scattered ^{30}Mg ejectiles can be identified. The broadened ejectile energy distribution (as compared e.g. to figure 6.2) results from the use of a 3.85 $\frac{\text{mg}}{\text{cm}^2}$ thick target.

recoils can leave the target and decay in-flight. Due to the assumption in the kinematics reconstruction (see section 4.1) that the reaction takes place at the target center the Ni recoils are calculated to be stopped in the target resulting in a broad contribution to the peak due to the failing Doppler correction.

The above assumption is confirmed when the ^{60}Ni 1332.5 keV transition γ is examined for different laboratory ^{30}Mg scattering angles: for small Θ_{CD} values the contribution from the wrongly Doppler corrected γ-rays to the peak is only small, whereas for larger Θ_{CD} values characterized by larger recoil velocities the contribution from the ^{60}Ni in-flight decay increases resulting in a broader peak shape.

For the determination of the peak area of the 1332.5 keV transition γ this effect can be included by fitting the peak with two different contributions. In figure 6.10 the fit to the Ni spectrum (without Mg contribution) is shown. The line shape of the Ni de-excitation γ-ray is well described when assuming the two contributions to the peak mentioned above. As in the kinematical reconstruction the Ni recoils are calculated to be stopped in the target (see above), the ^{30}Si γ-ray at 1263.2 keV is still visible as sharp line in the Ni Doppler corrected spectrum of figure 6.10.

$B(E2)\uparrow$ determination

After the extraction of the projectile and target de-excitation γ-yields and their correction with the deduced effective contamination the ^{30}Mg $B(E2)\uparrow$ value was determined by

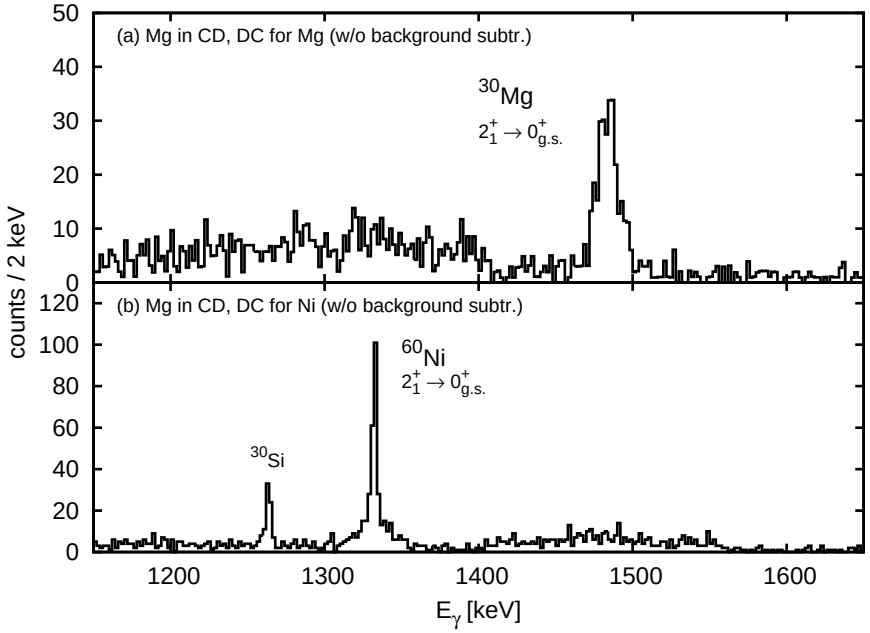

Figure 6.9: Doppler corrected γ-spectra for 2.69 MeV/u ^{30}Mg incident on the 3.85 $\frac{\text{mg}}{\text{cm}^2}$ ^{60}Ni target accepting only events where the Mg ejectiles are measured in the angular range of $16.4° \leq \Theta_{\text{CD}} \leq 36.6°$. No randoms have been subtracted: in the upper panel (a) the spectrum with Doppler correction performed for the Mg ejectiles is shown. The spectrum in (b) is obtained when the Doppler correction is carried out for the reconstructed Ni recoils. In addition to the Ni $2_1^+ \rightarrow 0^+_{\text{g.s.}}$ transition also a γ-ray of ^{30}Si (from β-decay) is observable in (b) (see also text).

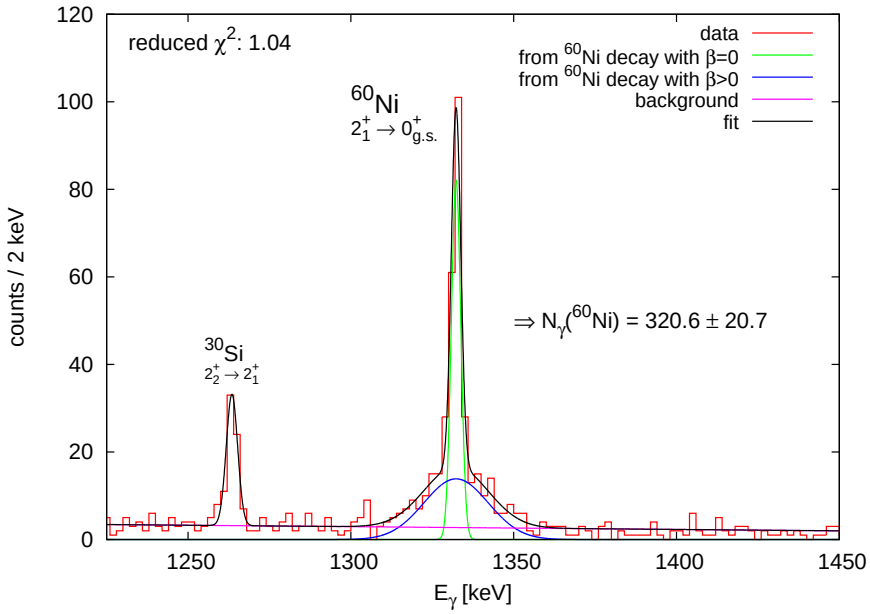

Figure 6.10: Fit to determine the peak area of the ^{60}Ni 1332.5 keV transition. The peak is fitted with the a contribution from the ^{60}Ni decay at rest (β=0) and in-flight ($\beta > 0$) resulting in a good description of the line shape. The ^{30}Si γ-ray is also fitted and shows the same widths as the "stopped" contribution to the ^{60}Ni peak.

the usual CLX calculation. The $B(E2;\ 0^+_{\text{g.s.}} \rightarrow 2^+_1)$ value for ^{30}Mg was determined to be $251 \pm 24\,(\text{stat}) \pm 12\,(\text{sys}) = 251\,(26)\ e^2\text{fm}^4$. The obtained value is in very good agreement with the value of $241\,(31)\ e^2\text{fm}^4$ from 2003. In addition, due to the higher statistics the relative error could be improved from 12.9 % to 10.4 % (see section 7.1.1 for the global ^{30}Mg $B(E2)\uparrow$ value of all experiments).

6.2.3 Differential cross section measurement

To examine in more detail the "safe" distance requirement the differential cross section $\left(\frac{d\sigma}{d\Omega}\right)_{\text{cm}}$ for the population of the ^{30}Mg 2^+ state at 1482.2 keV was determined for different Θ_{CD} scattering angles.

In addition to the usual determination of $\left(\frac{d\sigma}{d\Omega}\right)_{\text{cm}}$ in the different bins according to equation 2.31, which was also used in the case of ^{22}Ne (see section 5.2.2), the differential cross section was also determined by the "N_γ-method". In this method, the ^{30}Mg cross sections in the different Θ_{cm}-bins, $\sigma_{\text{CE,bin}}(^{30}\text{Mg})$, were calculated by

$$\sigma_{\text{CE,bin}}(^{30}\text{Mg}) = \frac{\epsilon_\gamma(^{60}\text{Ni})}{\epsilon_\gamma(^{30}\text{Mg})} \cdot \frac{W_\gamma(^{60}\text{Ni})}{W_\gamma(^{30}\text{Mg})} \cdot \frac{\sigma_{CE,\text{total}}(^{60}\text{Ni})}{N_{\gamma,\text{total}}(^{60}\text{Ni})} \cdot N_{\gamma,\text{bin}}(^{30}\text{Mg}), \tag{6.1}$$

where $\sigma_{\text{CE,total}}(^{60}\text{Ni})$ is the ^{60}Ni cross section in the total "safe" scattering angle range ($16.4° \leq \Theta_{\text{CD}} \leq 36.6°$) and $N_{\gamma,\text{total}}(^{60}\text{Ni})$ is the total number of observed Ni γ-rays in this

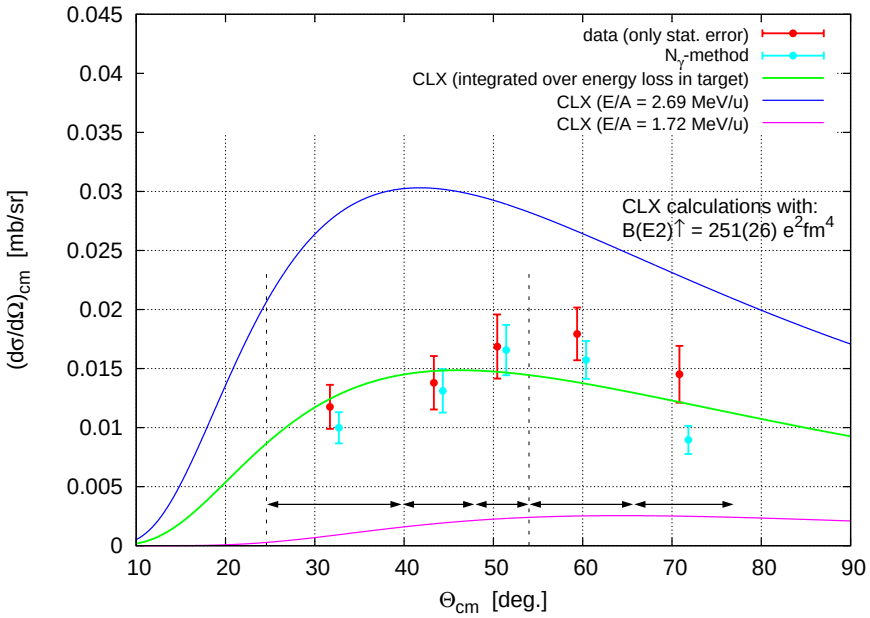

Figure 6.11: Differential cross section $\left(\frac{d\sigma}{d\Omega}\right)_{\mathrm{cm}}$ for Coulomb excitation of 2.69 MeV/u ^{30}Mg projectiles on a ^{60}Ni target: the data for both methods (besides the data point of the "N_γ-method" for the largest Θ_{cm}-bin) are in agreement with the CLX calculation when the integration is performed over the energy loss in the target (green line). For the $B(E2)\uparrow$ evaluation of ^{30}Mg only the Θ_{cm}-range between the dashed lines was used.

range. $N_{\gamma,\mathrm{bin}}(^{30}\mathrm{Mg})$ denotes the number of ^{30}Mg γ-rays in the different bins.

In figure 6.11 the deduced differential cross section using both methods is shown and compared to different CLX calculations. As in the "N_γ-method" the number of projectile de-excitation γ-rays in the different bins is compared to the *total* number of recoil γ-rays, the obtained differential cross section values allow to evaluate the Coulomb excitation strength only for the projectiles themselves. The $\left(\frac{d\sigma}{d\Omega}\right)_{\mathrm{cm}}$-values obtained from the two different methods are in good agreement apart from the value for the scattering angle bin of $65.7° \leq \Theta_{\mathrm{cm}} \leq 77.0°$ which corresponds to surface distances of 3.8 fm $\leq \Delta_s \leq$ 4.9 fm where a deviation from the expected theoretical distribution for the target integration calculation (green line) is observable.

This observation is supported by the occurrence of the ^{61}Ni 283.0 keV $\frac{1}{2}^-_1 \rightarrow \frac{3}{2}^-_{\mathrm{g.s.}}$ γ-ray (cf. figure 6.3) from the 1n-pickup reaction ^{60}Ni(^{30}Mg,^{29}Mg)^{61}Ni* which is observable when restricting the ^{30}Mg scattering angles to $65.7° \leq \Theta_{\mathrm{cm}} \leq 77.0°$. As this transfer γ-ray is *not* observable for the scattering angle range of $54.0° \leq \Theta_{\mathrm{cm}} \leq 65.7°$ which corresponds to surface distances for ^{30}Mg and ^{60}Ni of 4.9 fm $\leq \Delta_s \leq$ 6.5 fm, the restriction $\Delta_s \geq 5$ fm would have been sufficient instead of the applied more conservative choice of $\Delta_s \geq 6.5$ fm.

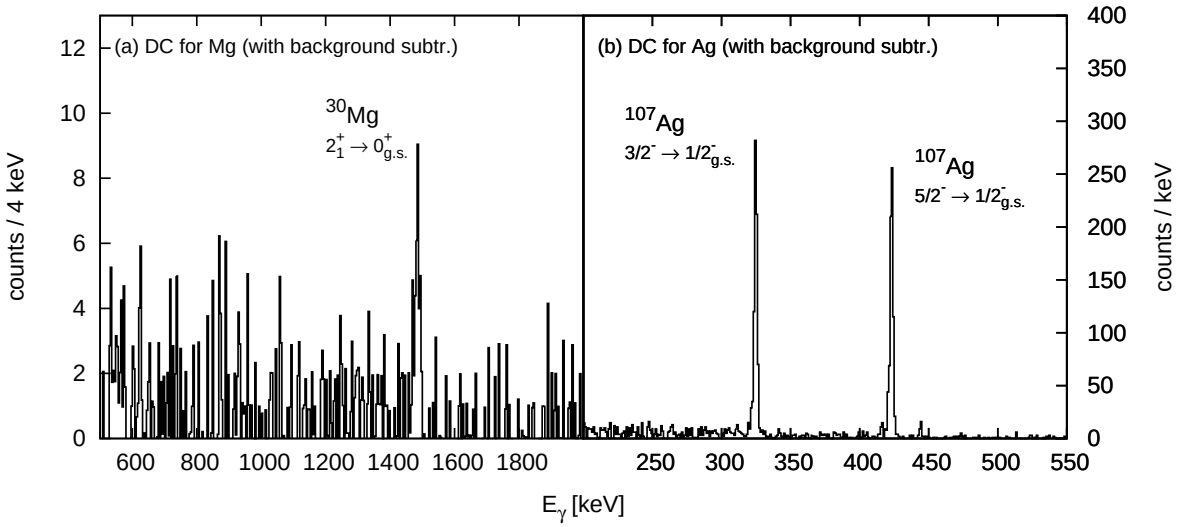

Figure 6.12: γ-spectra for a 2.69 MeV/u ^{30}Mg beam incident on a 4.4 $\frac{\text{mg}}{\text{cm}^2}$ ^{107}Ag target. The de-excitation γ-rays resulting from the Coulomb excitation of the ^{30}Mg projectiles (a) and the ^{107}Ag target nuclei (b) can be observed. The data were taken in coincidence with ^{30}Mg ions detected in the CD. Random spectra have been subtracted.

6.2.4 Measurement with a ^{107}Ag target

In addition to the two days run with the 3.85 $\frac{\text{mg}}{\text{cm}^2}$ ^{60}Ni target, a 13 hours measurement with a 4.4 $\frac{\text{mg}}{\text{cm}^2}$ ^{107}Ag target was also performed. In figure 6.12 the Doppler corrected γ-spectra are shown when gating on the scattered ^{30}Mg ejectiles detected in the CD. The well known γ-line at 1482.1 keV from the $2^+_1 \rightarrow 0^+_{\text{g.s.}}$ transition in ^{30}Mg is observable when the Doppler correction is performed for the detected Mg ejectiles (a), and the two ^{107}Ag lines at 324.8 keV and 423.2 keV resulting from the de-excitation of the first $\frac{3}{2}^-$ and $\frac{5}{2}^-$ states to the $\frac{1}{2}^-$ ground state show up in the spectrum (b) which is Doppler corrected for the recoiling Ag nuclei. Due to larger Z of $^{107}_{47}$Ag compared to $^{60}_{28}$Ni, the ^{107}Ag recoils get stuck in the thick target resulting in the narrow line widths of the transition γ-rays of figure 6.12 (b) (the uncorrected and the Ag-Doppler corrected spectra are almost identical as also in the kinematical reconstruction the ^{107}Ag recoils are calculated to get stuck in the target).

The extraction of the ^{30}Mg $B(E2; 0^+_{\text{g.s.}} \rightarrow 2^+_1)$ values results in a value of $291 \pm 46\,(\text{stat}) \pm 14\,(\text{sys}) = 291\,(48)\ e^2\text{fm}^4$. The rather large relative error of 16.5 % arises from the low count rate in the Mg peak (see figure 6.12 (a)). The obtained value is within the errors in agreement with the values of $241\,(31)\ e^2\text{fm}^4$ (see section 6.1.2) and $251\,(26)\ e^2\text{fm}^4$ (see section 6.2.2).

	method	$N(^{32}\mathrm{Al})_{\mathrm{decay}}$ [%]	$N(^{32}\mathrm{Al})_{\mathrm{total}}$ [%]	$N(^{32}\mathrm{Si})_{\mathrm{decay}}$ [%]	$N(^{32}\mathrm{Si})_{\mathrm{total}}$ [%]
(a)	breeding	13.1 (21)		4.26 (88)	
(b)	ΔE (60h-fit)		11.89 (25)		
(c)	ΔE (thin tar.)		10.68 (36)		1.02 (18)
	average		11.89 (72)		2.64 (88)

Table 6.3: Contributions of ^{32}Al and ^{32}Si in the ^{32}Mg beam for Exp_Sep04.

6.3 Coulomb excitation of ^{32}Mg

The first low-energy Coulomb excitation experiment of ^{32}Mg was performed in October 2004 at the REX-ISOLDE facility at CERN. The neutron-rich ^{32}Mg which has six neutrons more than the heaviest stable Mg isotope ^{26}Mg has a half life of only $t_{1/2}(^{32}\mathrm{Mg}) = 95\,(16)$ ms [53].

Because of the lower X-ray background caused by the accelerator at the present MINIBALL position and the more reliable operation of the rf-amplifiers of the REX-LINAC, the experiment was performed at a beam energy of 2.84 MeV/u instead of the nominal maximum REX energy of 3.0 MeV/u. To Coulomb excite the first 2^+ level in ^{32}Mg at 885.3 keV the ^{32}Mg beam ($q = 9^+$) with an intensity of about 1.5×10^4 particles per second was incident on a 4.4 $\frac{\mathrm{mg}}{\mathrm{cm}^2}$ thick ^{107}Ag target. Data were taken during a measuring time of about 60 hours. From figure 4.14 (a) it can be seen that the ^{32}Mg ions are characterized by a fast release from the ISOLDE target. In the analysis of the experiment only events within the first 400 ms after the T1 proton pulses were considered, i.e. $0 \leq T_{\mathrm{p}} \leq 0.4$ s.

The further analysis steps used in the extraction of the $B(E2;\ 0^+_{\mathrm{g.s.}} \rightarrow 2^+_1)$ value of ^{32}Mg are described in the following sections.

6.3.1 Purity of the ^{32}Mg beam

To determine the beam purity of the ^{32}Mg beam of Exp_Sep04, only two of the various methods discussed in section 4.4 could be applied. The amount of ^{32}Al and ^{32}Si resulting from the breeding could be determined, as well as the total amount of ^{32}Al and ^{32}Si could be deduced from the analysis of the data obtained with the ΔE-detectors (see section 4.4.2 and figure 4.14). Due to the rather low beam intensity and the short measuring time of only about 30 min, however, no quantitative information could be obtained from the LASER on/off-measurement. Moreover, the extraction of a value for the beam contamination from the release curve analysis was also not possible since ^{32}Al decays to the long-lived ^{32}Si ($t_{1/2}(^{32}\mathrm{Si}) = 132\,(13)$ y from [53]) with a half life of only $t_{1/2}(^{32}\mathrm{Al}) = 33\,(4)$ ms [53]. The analysis of the γ-spectra activity also does not allow for a quantitative analysis of the beam contaminants since the branching ratio of the β-decay of ^{32}Mg to ^{32}Al is not known.

In table 6.3 the contributions of ^{32}Al and ^{32}Si to the ^{32}Mg beam are listed. The analysis of the ΔE-detector data resulted in two quantitative determinations for the beam purity:

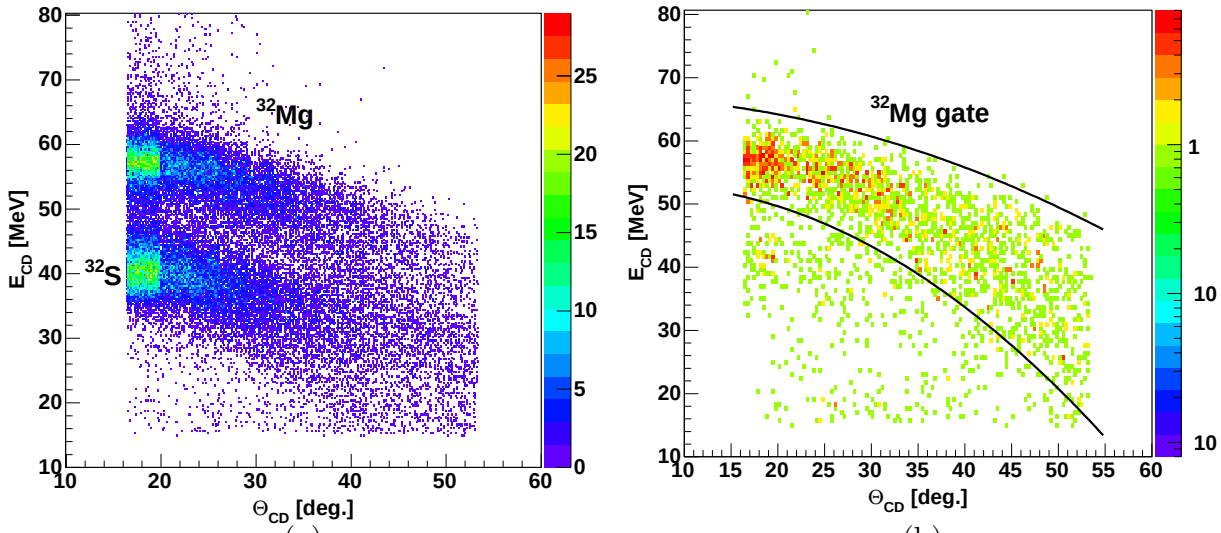

Figure 6.13: CD-energy vs. Θ_{CD} for the 2.84 MeV/u ^{32}Mg beam impinging on a 4.4 $\frac{\mathrm{mg}}{\mathrm{cm}^2}$ ^{107}Ag target: (a) Plot including events with a particle in the CD-detector and a γ-ray in the MINIBALL array. The scattered ^{32}Mg ejectiles as well as the isobaric ^{32}S contaminants can be identified. (b) When gating on a coincident γ-ray and only considering events in the first 400 ms after the T1 proton pulses, the ^{32}S ions can be strongly suppressed.

the contribution of ^{32}Al to the beam was monitored over the whole measurement of 60 hours (b) (cf. figure 4.14 (c)) and a short run with a thin 1.1 $\frac{\mathrm{mg}}{\mathrm{cm}^2}$ ^{107}Ag target yielded values of beam contributions for ^{32}Al and ^{32}Si (c) (see section 4.4.2 and [55]). For the amount of ^{32}Al and ^{32}Si in the beam, average values of $N(^{32}\mathrm{Al})_{\mathrm{total}} = 11.9\,(7)\,\%$ and $N(^{32}\mathrm{Si})_{\mathrm{total}} = 2.6\,(9)\,\%$ were obtained from the three individual values (see table 6.3). Since ^{32}Mg and ^{32}Al show the same fast ISOLDE target release behavior (cf. figure 4.14 (a)) and since the three values obtained for the ^{32}Al contamination are in very good agreement, it can be concluded that all isobaric contaminants originate from the β-decay during trapping and breeding, allowing only for a negligible small fraction to result from the primary ISOLDE target.

In addition to ^{32}Al and ^{32}Si an additional beam impurity resulting from the residual-gas ionization in the EBIS source is present (see figure 4.14). This ^{32}S contamination can be clearly identified via the energy in the CD-detector (see figure 6.13).

6.3.2 Extraction of the $B(E2;\ 0^+_{\mathrm{g.s.}} \rightarrow 2^+_1)$ value

For the determination of the $B(E2)\uparrow$ value of ^{32}Mg the energy measured in the CD-detector was utilized to identify the scattered ejectiles. Figure 6.13 shows the CD-energy plotted versus the corresponding Θ_{CD} values. The scattered ^{32}Mg ejectiles and the isobaric ^{32}S

nuclei originating from the residual gas of the EBIS can be well separated for small scattering angles (a). Due to the similar nuclear charge numbers Z and the non-optimal energy resolution obtained with the CD-counter the ^{32}Al isobars ^{32}Al cannot be separated from the Mg ejectiles and are fully contained in the analysis window. The situation is slightly different for the small ^{32}Si contribution of 2.6 (9) % which might only partly be contained in the chosen window.

The ^{32}S, however, can be suppressed very well when requiring a coincident γ-ray and if only the first 400 ms after the T1 proton pulses are analyzed (b). From figure 6.13 (b) it is also obvious that for large Θ_{CD} values the ejectile energies decrease more than for a thin target (cf. e.g. figure 6.2) requiring a Mg gate as shown in figure 6.13 (b). This asymmetric shape follows from the higher momentum transfers to the Ag recoils and the larger energy loss variation in the target for larger scattering angles. In the determination of the recoil γ-yields a correction due to the partial overlap of ^{32}S events with the ^{32}Mg gate is performed.

For a beam energy of 2.84 MeV/u the CD Θ_{CD}-range of 16.4° to 53.3° corresponds to surface distances of the Mg and Ag nuclei of 7.2 fm $\leq \Delta_s \leq$ 28.2 fm when ^{32}Mg is detected in the CD-detector. The current experiment can thus be denoted as "safe" for all these events.

The γ-spectrum of figure 6.14 is obtained when gating on the ^{32}Mg ejectiles in the CD-detector and considering only events in the first 400 ms after the T1 pulses. Although no random background subtraction was carried out in this case the spectrum can be regarded as background free. Besides the ^{32}Mg $2_1^+ \rightarrow 0_{\mathrm{g.s.}}^+$ transition γ-ray at 885.3 keV no additional de-excitation line is observable above 500 keV due to the limitation of the maximum excitation energies to about 1-2 MeV for low-energy Coulomb excitation experiments (see section 2.3). The FWHM resolution of the 885.3 keV γ-line after Doppler correction amounts to 11.0 keV.

Figure 6.15 displays the Doppler corrected spectra selecting the events as in figure 6.14 but subtracting the random background and performing the Doppler correction for Mg ejectiles (panel (a)) and reconstructed Ni-recoils (panel (b)). These spectra were used to determine the γ-intensities. By fitting the transition lines of ^{32}Mg (a) and ^{107}Ag (b) the γ-intensities can be determined.

$B(E2)\uparrow$ determination

To determine the $B(E2;\ 0_{\mathrm{g.s.}}^+ \rightarrow 2_1^+)$ value of ^{32}Mg the ^{107}Ag γ-intensities obtained from the fit were corrected to account for

- the transition from the 423.2 keV to the 324.8 keV state (see figure 5.6),
- possible emission of conversion electrons,
- the occurrence of ^{32}S in the ^{32}Mg gate (see figure 6.13) and
- the *effective* isobaric contamination with ^{32}Al and ^{32}Si.

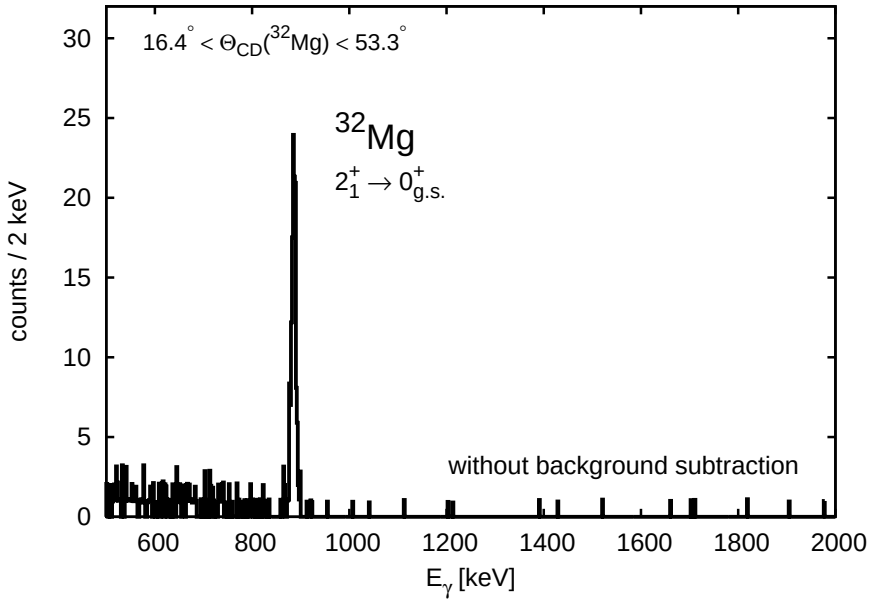

Figure 6.14: High-energy part of the γ-spectrum observed for the 2.84 MeV/u ^{32}Mg incident on a 4.4 $\frac{\text{mg}}{\text{cm}^2}$ ^{107}Ag target observed in coincidence with Mg ejectiles (no random subtraction). The Doppler correction was carried out assuming the ejectile to be the γ-emitting nucleus.

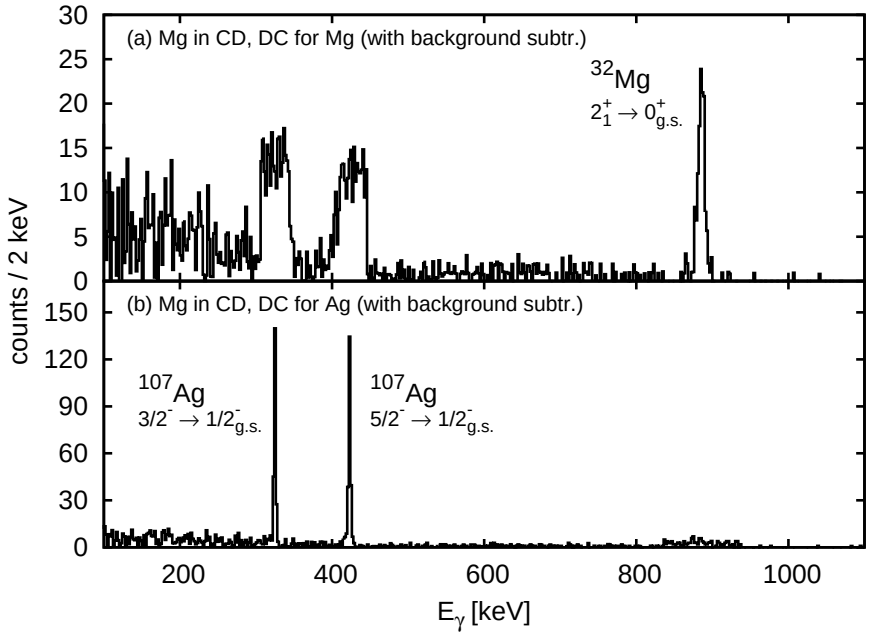

Figure 6.15: Total Doppler corrected γ-spectra for the ^{32}Mg Coulomb excitation experiment selecting events as for figure 6.14 but subtracting random events: the upper panel (a) shows the Doppler corrected spectrum for the γ-emitting Mg nuclei, panel (b) displays the corresponding spectrum when the correction is carried out for the reconstructed Ag recoils.

According to [53] the total internal conversion coefficients for the $\frac{3}{2}^-_1 \rightarrow \frac{1}{2}^-_{\text{g.s.}}$ and $\frac{5}{2}^-_1 \rightarrow \frac{1}{2}^-_{\text{g.s.}}$ transitions in ^{107}Ag amount to $\alpha = 0.0180(1)$ and $\alpha = 0.0104$, respectively.

The contribution of ^{32}S was estimated by determining the number of ^{32}S ions contributing to the Mg gate of figure 6.13 (b). When requiring times T_p since the last T1 proton pulse of $0.8\,\text{s} \leq T_\text{p} \leq 2.4\,\text{s}$, the amount of ^{32}S in the Mg gate could be determined as for the chosen time window only the S ions are present in the gate and no ^{32}Mg (and also no ^{32}Al and ^{32}Si) ions (cf. figure 4.14 (a)). By also considering the fact that the Coulomb excitation probabilities for the excitation of the relevant ^{107}Ag states by ^{32}Mg and ^{32}S projectiles are different, the factors for the correction of the two ^{107}Ag γ-yields could be determined. The obtained correction factors amount only to about 0.4 % for both Ag γ-lines.

In the extraction of the ^{32}Mg $B(E2)\uparrow$ value, the ^{32}Si ions were assumed to be fully contained in the Mg gate of figure 6.13 (b). This assumption was accounted for in the systematical error of the ^{32}Mg $B(E2)\uparrow$ value.

With the 885.3 keV γ-intensity obtained from a fit and the corrected ^{107}Ag intensities of the 324.8 keV and 423.2 keV de-excitation γ-rays, the ^{32}Mg $B(E2)\uparrow$ values can then be determined relative to the two Ag transitions using the CLX code. For the two Ag $E2$ matrix elements the values obtained from the weighted average of the previous Coulomb excitation experiments and the calibration with the ^{22}Ne experiment are taken (see section 5.2.3). For the static quadrupole moment of ^{32}Mg the rotational model value for prolate deformation was assumed (see also section 7.1.1).

The analysis results in a final ^{32}Mg $B(E2;\, 0^+_{\text{g.s.}} \rightarrow 2^+_1)$ value of $434 \pm 35\,(\text{stat}) \pm 39\,(\text{sys}) = 434\,(52)\ e^2\text{fm}^4$, where the total relative error amounts to 12.1 %. In table 6.4 the ^{32}Mg $B(E2)\uparrow$ values relative to the two Ag transitions as well as their weighted average and the error budget are listed. In the final ^{32}Mg $B(E2)\uparrow$ value the uncertainty due to the beam contamination and the ^{32}Si and ^{32}S corrections which are the same for both single values was only considered once resulting in a slightly increased final total error compared to the simple weighted average of the two single values.

	rel. to 324.8 keV	rel. to 423.2 keV	weighted average
$B(E2)\uparrow$ [e^2fm^4]	427.1	441.3	434.1
total error [e^2fm^4]	63.5	63.7	52.4
stat. error [e^2fm^4]	49.5	50.2	35.2
sys. error [e^2fm^4]	39.8	39.2	38.7
statistical errors [%]			
$\sigma(N_\gamma(\mathrm{Mg}))$ [%]	8.9	8.9	
$\sigma(N_\gamma(\mathrm{Ag}))$ [%]	7.4	7.1	
average stat. error [%]	11.6	11.4	8.1
systematical errors [%]			
Ag transition [%]	0.4	0.4	
internal conversion [%]	0.6		
B(E2)(Ag) [%]	4.0	3.2	
γ efficiency [%]	1.7	1.5	
γ corr. factor [%]	0.1	0.1	
eff. contamination [%]	7.8	7.7	
^{32}Si correction [%]	2.6	2.6	
^{32}S correction [%]	0.4	0.4	
average sys. error [%]	9.3	8.9	8.9

Table 6.4: Summary and error budget for the ^{32}Mg $B(E2)\uparrow$ values determined relative to the two Ag transitions $\frac{1}{2}^-_{\mathrm{g.s.}} \rightarrow \frac{3}{2}^-_1$ and $\frac{1}{2}^-_{\mathrm{g.s.}} \rightarrow \frac{5}{2}^-_1$. The weighted average (with a proper consideration of the same systematical uncertainties) is also shown.

Chapter 7

Discussion

In the present chapter the results obtained from the Coulomb excitation experiments with ^{30}Mg and ^{32}Mg are summarized and compared to theoretical predictions and results from intermediate-energy Coulomb excitation measurements.

7.1 The neutron-rich isotopes ^{30}Mg and ^{32}Mg

7.1.1 The $B(E2;\ 0^+_{\text{g.s.}} \rightarrow 2^+_1)$ values for ^{30}Mg and ^{32}Mg

For ^{30}Mg the three experiments performed during the experimental campaigns Exp_Oct03 and Exp_Sep04 can be summarized resulting in a final $B(E2)\uparrow$ value. When combining the five (in two experiments the $B(E2)\uparrow$ was determined relative to two target transitions) individual $B(E2)\uparrow$ values, care has to be taken of identical systematic errors. First, the uncertainty in the beam contamination was the same for the $B(E2)\uparrow$ values determined relative to the transitions in ^{58}Ni and ^{60}Ni for Exp_Oct03. In addition, the same uncertainty in the ^{60}Ni target $B(E2)\uparrow$ value were given for the Coulomb excitation experiments with the natural Ni target in 2003 and the enriched ^{60}Ni target in 2004. As the third and final identical systematic uncertainty, the beam purity was known with the same accuracy for the two ^{30}Mg $B(E2)\uparrow$ values determined relative to the two transitions in ^{107}Ag in 2004.

In table 7.1 the five individual measurements of the $B(E2;\ 0^+_{\text{g.s.}} \rightarrow 2^+_1)$ value of ^{30}Mg are summarized and the weighted average of the measurements is given. The final global weighted average value for ^{30}Mg results in $B(E2;\ 0^+_{\text{g.s.}} \rightarrow 2^+_1) = 253\,(21)\ e^2\text{fm}^4$. The results for the Coulomb excitation experiment of ^{32}Mg are summarized in the lower part of table 7.1.

In the determination of the $B(E2)\uparrow$ values of ^{30}Mg and ^{32}Mg the static quadrupole moments of the 2^+ states were calculated using the rotational model assuming a prolate deformation for the nuclei. This assumption is supported by the calculations in [16] and [18] where both for ^{30}Mg and ^{32}Mg spectroscopic quadrupole moments corresponding to a prolate deformation are predicted.

To investigate the influence of the static quadrupole moments on the deduced $B(E2)\uparrow$

nucleus	beam en. [MeV/u]	target, thick. [$\frac{\text{mg}}{\text{cm}^2}$]	normalization transition	$B(E2)\uparrow$ [$e^2\text{fm}^4$]	total [$e^2\text{fm}^4$]	stat. [$e^2\text{fm}^4$]	sys. [$e^2\text{fm}^4$]
^{30}Mg	2.25	$^{\text{nat.}}$Ni, 1.0	^{58}Ni, $0^+_{\text{g.s.}} \rightarrow 2^+_1$	277.6	53.7	51.2	16.2
”	”	”	^{60}Ni, $0^+_{\text{g.s.}} \rightarrow 2^+_1$	223.0	38.1	36.8	9.8
”			weighted average	241.2	31.1	29.9	8.4
”	2.69	^{60}Ni, 3.85	^{60}Ni, $0^+_{\text{g.s.}} \rightarrow 2^+_1$	251.3	26.5	23.7	11.9
”	2.69	^{107}Ag, 4.4	^{107}Ag,$\frac{1}{2}^-_{\text{g.s.}} \rightarrow \frac{3}{2}^-_1$	279.4	66.1	63.2	19.6
”	”	”	^{107}Ag,$\frac{1}{2}^-_{\text{g.s.}} \rightarrow \frac{5}{2}^-_1$	303.5	71.2	68.6	19.0
”			weighted average	290.6	48.4	46.5	13.6
”			global w. average	253.4	21.3	17.6	11.9
^{32}Mg	2.84	^{107}Ag, 4.4	^{107}Ag,$\frac{1}{2}^-_{\text{g.s.}} \rightarrow \frac{3}{2}^-_1$	427.1	63.5	49.5	39.8
”	”	”	^{107}Ag,$\frac{1}{2}^-_{\text{g.s.}} \rightarrow \frac{5}{2}^-_1$	441.3	63.7	50.2	39.2
”			weighted average	434.1	52.4	35.2	38.7

Table 7.1: Summary of the $B(E2;\ 0^+_{\text{g.s.}} \rightarrow 2^+_1)$ values of ^{30}Mg and ^{32}Mg in the present work.

values, in addition to the calculations assuming a quadrupole moment according to the rotational model with a prolate deformation (“$Q^{\text{rot}}_{2^+}$ (prolate)”), the calculations were also performed with different assumptions for the quadrupole moments, i.e. assuming a vanishing quadrupole moment and a quadrupole moment according to the rotational model but corresponding to an oblate deformation (“$Q^{\text{rot}}_{2^+}$ (oblate)”). In table 7.2 the resultant $B(E2)\uparrow$ values for ^{30}Mg and ^{32}Mg are compared. When assuming a vanishing quadrupole moment instead of the prolate case, the $B(E2)\uparrow$ values decrease by about 5 %. As this decrease is small compared to the total uncertainties of the $B(E2)\uparrow$ values and theory predicts large prolate quadrupole moments, the final $B(E2;\ 0^+_{\text{g.s.}} \rightarrow 2^+_1)$ values are given for the assumption $Q^{\text{rot}}_{2^+}$ (prolate).

$B(E2)\uparrow$ for	normalization transition	assumed Q_{2^+}	$B(E2)\uparrow$ [$e^2\text{fm}^4$]	error [$e^2\text{fm}^4$]
^{30}Mg	^{60}Ni, $0^+_{\text{g.s.}} \rightarrow 2^+_1$	$Q^{\text{rot}}_{2^+}$ (prolate)	251.3	26.5
”	”	0	238.5	25.1
”	”	$Q^{\text{rot}}_{2^+}$ (oblate)	227.1	23.9
^{32}Mg	^{107}Ag,$\frac{1}{2}^-_{\text{g.s.}} \rightarrow \frac{3}{2}^-_1$	$Q^{\text{rot}}_{2^+}$ (prolate)	427.1	62.5
”	”	0	402.4	58.9
”	”	$Q^{\text{rot}}_{2^+}$ (oblate)	381.2	55.8

Table 7.2: Influence of quadrupole moment on deduced $B(E2)\uparrow$ values for ^{30}Mg and ^{32}Mg.

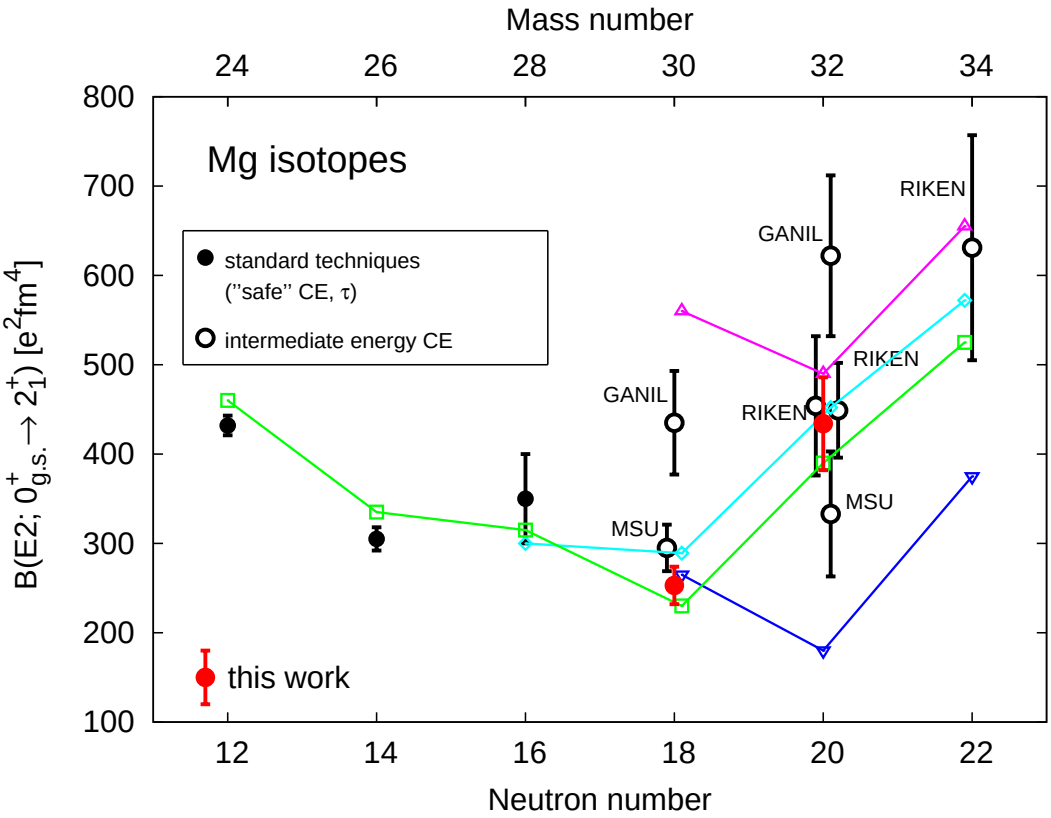

Figure 7.1: Experimental $B(E2)\uparrow$ values for the neutron-rich Mg isotopes. The present values for ^{30,32}Mg are displayed together with results from standard techniques for ^{24,26,28}Mg [59] and results from intermediate-energy measurements for ^{30,32,34}Mg (GANIL [12], MSU [10] and RIKEN [9, 11]). The theoretical predictions are drawn with lines to guide the eye ($\Diamond$: [13, 20], $\triangledown$: [16]-normal, $\triangle$: [16]-intruder, $\square$: [18]).

7.1.2 Comparison with intermediate-energy measurements

In figure 7.1 the $B(E2)\uparrow$ values determined in this work are shown together with previous measurements at the intermediate-energy facilities GANIL, MSU and RIKEN. In addition to the experimental values also predictions from selected theoretical calculations are drawn (see section 7.1.3).

In the case of ^{30}Mg the $B(E2)\uparrow$ value was previously measured at MSU (295 (26) e^2fm^4 [10]) and GANIL (435 (58) e^2fm^4 [12]). It stands out that our value is lower compared to the MSU and GANIL values by about 15 % and 40 %, respectively. This raises the question for the course of these discrepancies which are rather likely due to two problems (which will be discussed in the following) inherent in the experiments at intermediate energies which are difficult to control properly (see also section 2.5).

At beam energies of about 30 - 50 MeV/u used in the intermediate-energy experiments the excitation of the nuclei can also be caused by nuclear forces in addition to the elec-

tromagnetic forces, and interferences of the Coulomb and the nuclear forces have to be taken into account. In figure 7.2 the calculated inelastic differential cross section is shown for ^{24}Mg of 32 MeV/u impinging on a ^{208}Pb and a ^{12}C target. The interference of the excitation caused by the Coulomb and the nuclear forces is clearly visible even at small scattering angles, say $\lesssim 6^\circ$, which one usually tries to select in these experiments.

Another important issue is the occurrence of feeding from higher lying states to the investigated state. As the maximum excitation energies in intermediate-energy experiments can be as high as 5 - 15 MeV, other 2^+ states can also be populated by Coulomb excitation which may decay to the first 2^+ state. As usually the feeding γ-rays are not individually observable, the feeding contribution has to be estimated from model calculations.

In the case of the ^{30}Mg measurement at MSU no correction for possible feeding of the 2_1^+ state was applied. In the GANIL measurement, however, a mean feeding contribution of 18.5 % for the two experiments performed was estimated and included in their $B(E2)\uparrow$ analysis. Correcting the MSU value with this feeding contribution, a corrected MSU value of 240 (21) e^2fm^4 would be obtained which would be in agreement with the present value of 253 (21) e^2fm^4. Due to the experimental settings, which are not identical for the GANIL and the MSU measurements, the calculated GANIL feeding contribution is not exactly transferable to the MSU measurement but nevertheless might at least explain the difference in the $B(E2)\uparrow$ values determined at MSU and in this work. The discrepancy of our value to the GANIL value remains unknown at this point.

For ^{32}Mg our $B(E2)\uparrow$ value of 434 (52) e^2fm^4 is in good agreement with the two RIKEN values of 454 (78) e^2fm^4 [9] and 449 (53) e^2fm^4 [11]. In the MSU value of 333 (70) e^2fm^4 [10] a feeding correction of about 25 % is included. If no feeding correction is applied a ^{32}Mg $B(E2)\uparrow$ value of 440 (55) e^2fm^4 is obtained which agrees with the two RIKEN values and the value determined in this work. Similar to the case of ^{30}Mg, the ^{32}Mg $B(E2)\uparrow$ value of 622 (90) e^2fm^4 determined by the GANIL group is considerably higher than found in the other measurements raising the question of possible systematic effects in these measurements at GANIL.

7.1.3 Comparison with theoretical predictions

Because of the great interest in the structure of the neutron-rich Ne, Na and Mg nuclei a large number of model calculations exist for these nuclei. Figure 7.3 compares the $B(E2)\uparrow$ values for ^{30}Mg and ^{32}Mg obtained in the present work to these predictions. The theoretical values were taken from: [13, 20] (Utsuno *et al.*, 1999,2002), [16] (Caurier *et al.*, 2001) [18] (Rodriguez-Guzman *et al.*, 2002), [19] (Stevenson *et al.*, 2002), [14] (Dean *et al.*, 1999), [17] (Kimura *et al.*, 2002), [15] (Peru *et al.*, 2000), and [21] (Yamagami *et al.*, 2004).

When comparing our experimental $B(E2)\uparrow$ value for ^{30}Mg to theory, the shell model calculations performed in [16] are particularly interesting. The calculations are performed separately for *sd*-shell configurations and also for ground state "intruder" configurations with neutrons excited from the *sd* to the *pf* shell. As the ^{30}Mg $B(E2)\uparrow$ value of 253 (21) e^2fm^4 is in very good agreement with the calculation assuming only *sd*-shell configurations it can be concluded that ^{30}Mg lies still outside the *island of inversion*. Our $B(E2)\uparrow$ value

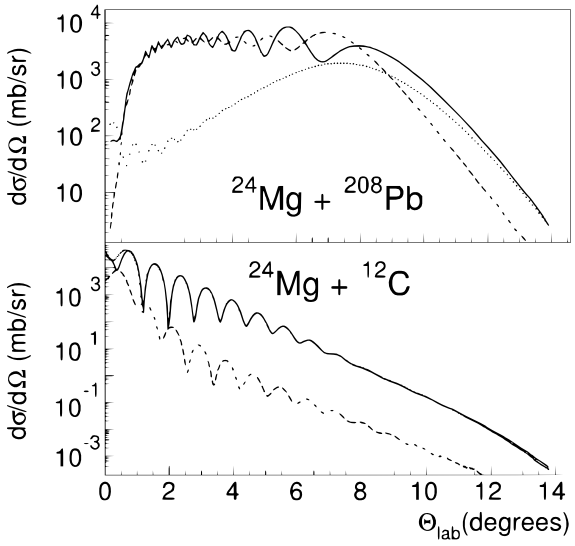

Figure 7.2: Differential cross section for 32 MeV/u ^{24}Mg impinging on a ^{208}Pb or a ^{12}C target showing the different contributions to the excitation of the 2^+ state in ^{24}Mg. The contributions from Coulomb (dashed lines) and nuclear (dotted lines) excitations as well as the resulting cross sections (solid lines) are shown (from [12]).

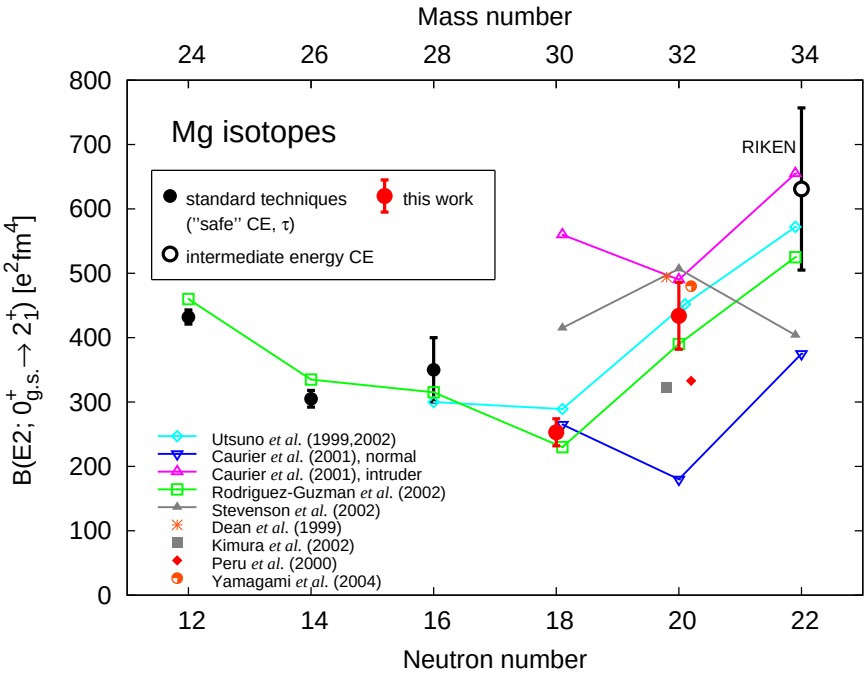

Figure 7.3: The $B(E2)\uparrow$ values determined in the present work for ^{30}Mg and ^{32}Mg are compared to different theoretical predictions (see text for the references).

Isotope	$B(E2;\ 0^+_{\text{g.s.}} \rightarrow 2^+_1)$ [$e^2\text{fm}^4$]	$t_{1/2}(2^+_1)$ [ps]	$\lvert\beta_2\rvert$
^{30}Mg	253 (21)	1.55 (13)	0.400 (17)
^{32}Mg	434 (52)	11.9 (14)	0.501 (30)

Table 7.3: Half lifes and quadrupole deformation parameters for ^{30}Mg and ^{32}Mg derived from the determined $B(E2)\uparrow$ values.

for ^{30}Mg is also well reproduced by the Monte Carlo shell model (MCSM) calculations of [13, 20] including particle-hole excitations from the *sd* to the *pf* shell, as well as by the calculations of [18] within the framework of the Angular Momentum Projected Generator Coordinate Method (AMPGCM).

For ^{32}Mg the calculations in [13, 18, 20] and in particular also the "intruder" calculation of [16] can well describe the present $B(E2)\uparrow$ value of 434 (52) $e^2\text{fm}^4$. Our result therefore confirms that ^{32}Mg is lying inside the *island of inversion* and exhibits an almost pure "intruder" ground state configuration.

7.2 Summary

In summary, the first "safe" low-energy Coulomb excitation experiments have been carried out at REX-ISOLDE with the aim to determine the $B(E2;\ 0^+_{\text{g.s.}} \rightarrow 2^+_1)$ values for the neutron-rich Mg isotopes ^{30}Mg and ^{32}Mg. The Mg projectiles provided by the REX-ISOLDE facility at CERN with energies up to 2.84 MeV/u were incident on the MINIBALL targets with thicknesses of a few $\frac{\text{mg}}{\text{cm}^2}$. The de-excitation γ-rays of both projectile and target excitations were detected with the MINIBALL γ-spectrometer. By measuring the γ-yields the $B(E2)\uparrow$ values of ^{30}Mg and ^{32}Mg could be determined relative to the well known $B(E2)\uparrow$ values of the target nuclei.

The analysis of the experiments resulted in final $B(E2)\uparrow$ values for ^{30}Mg of $B(E2;\ 0^+_{\text{g.s.}} \rightarrow 2^+_1) = 253\,(21)\ e^2\text{fm}^4$ and for ^{32}Mg of $B(E2;\ 0^+_{\text{g.s.}} \rightarrow 2^+_1) = 434\,(52)\ e^2\text{fm}^4$. As the ^{30}Mg result can well be described by a shell model calculation with a "normal" shell ordering and no "intruder" ground state configuration, it can be concluded that ^{30}Mg lies outside the *island of inversion*. The large $B(E2)\uparrow$ value of ^{32}Mg can well be described assuming a $2p-2h$ intruder ground state with a prolate deformation. In table 7.3 the half lifes of the first 2^+ states and the magnitude of the quadrupole deformation parameters β_2 for ^{30,32}Mg are listed which can be derived from the measurements presented in this work.

With the measurement of the $B(E2)\uparrow$ values of ^{30}Mg and ^{32}Mg the next logical step would be the exploration of the collectivity in the neutron-rich Mg isotopes towards even more exotic nuclei starting with ^{34}Mg to review the RIKEN result. As the ISOLDE yields drop by about one order of magnitude for each additional neutron, such an experiment at the ISOLDE facility would only be feasible with increased ISOLDE yields and further (possible) gains in the REX-ISOLDE efficiency.

Appendix A

Coulomb excitation

A.1 Excitation cross section

In first order perturbation theory, the Coulomb excitation cross section for an electric excitation of order $E\lambda$ is given by [26]

$$\sigma_{E\lambda} = \left(\frac{Z_t e}{\hbar v}\right)^2 a_0^{-2\lambda+2} B(E\lambda) f_{E\lambda}(\xi) \tag{A.1}$$

with

$$f_{E\lambda}(\xi) = \int_{\Theta_1}^{\Theta_2} \frac{df_{E\lambda}(\Theta,\xi)}{d\Omega} d\Omega \tag{A.2}$$

$$= \frac{16\pi^3}{(2\lambda+1)^3} \sum_\mu |Y_{\lambda\mu}(\frac{\pi}{2},0)|^2 \int_0^\pi |I_{\lambda\mu}(\Theta,\xi)|^2 \frac{\cos(\frac{\Theta}{2})}{\sin^3(\frac{\Theta}{2})} d\Theta \; . \tag{A.3}$$

$Y_{\lambda\mu}(\Theta,\phi)$ are the normalized spherical harmonics and the functions $I_{\lambda\mu}(\Theta,\xi)$ are given by

$$I_{\lambda\mu}(\Theta,\xi) = \int_{-\infty}^{\infty} e^{i\xi(\epsilon\sinh(w)+w)} \times \frac{[\cosh(w)+\epsilon+i(\epsilon^2-1)^{\frac{1}{2}}\sinh(w)]^\mu}{[\epsilon\cosh(w)+1]^{\lambda+\mu}} dw \; . \tag{A.4}$$

For a magnetic excitation of order $M\lambda$, the cross section is given by

$$\sigma_{M\lambda} = \left(\frac{Z_t e}{\hbar c}\right)^2 a_0^{-2\lambda+2} B(M\lambda) f_{M\lambda}(\xi) \tag{A.5}$$

with

$$f_{M\lambda}(\xi) = \frac{16\pi^3}{(2\lambda+1)^2} \sum_\mu \frac{(\lambda+1)^2-\mu^2}{\lambda^2(2\lambda+3)} |Y_{\lambda+1,\mu}(\frac{\pi}{2},0)|^2 \tag{A.6}$$

$$\times \int_0^\pi |I_{\lambda+1,\mu}(\Theta,\xi)|^2 \cot^2(\frac{\Theta}{2}) \cdot \frac{\cos(\frac{\Theta}{2})}{\sin^3(\frac{\Theta}{2})} d\Theta \; .$$

A.2 Angular distributions

The γ-ray angular distribution for the Coulomb excitation of an initial state $|i\rangle$ to the final state $|f\rangle$ and subsequent de-excitation to the state $|ff\rangle$ (which can be identical to $|i\rangle$) is given by

$$\begin{aligned} W(\Theta_\gamma) &= \sum_{k\,even, M_i, M_f, L, L'} |a_{i\to f}|^2 \begin{pmatrix} I_f & I_f & k \\ M_f & -M_f & 0 \end{pmatrix} (-1)^{M_f} \\ &\quad \times F_k(L, L', I_{ff}, I_f)\sqrt{2k+1} P_k(\cos(\Theta_\gamma))\delta_L \delta_{L'} \ . \end{aligned} \tag{A.7}$$

This equation holds for the special case where the scattered particles are detected in a ring counter being symmetric around the beam axis. In equation A.7, $a_{i\to f}$ is the excitation amplitude (see equation 2.5) and Θ_γ denotes the angle between the γ-ray and the incident beam in the cm-system. The Wigner or $3j$-symbol is defined by [30]

$$\begin{pmatrix} j_1 & j_2 & j_3 \\ m_1 & m_2 & m_3 \end{pmatrix} = (-1)^{j_1 - j_2 - m_3}(2j_3+1)^{-1/2}\langle j_1 m_1 j_2 m_2 | j_3 - m_3\rangle \ , \tag{A.8}$$

where $\langle j_1 m_1 j_2 m_2 | j_3 - m_3\rangle$ are the Clebsch-Gordon-coefficients. The $\gamma - \gamma$ correlation function $F_k(L, L', I_{ff}, I_f)$ is given by [26]

$$\begin{aligned} F_k(L, L', I_{ff}, I_f) &= (-1)^{I_{ff}+I_f-1}\sqrt{(2k+1)(2I_f+1)(2L+1)(2L'+1)} \\ &\quad \times \begin{pmatrix} L & L' & l \\ 1 & -1 & 0 \end{pmatrix} \begin{Bmatrix} L & L' & k \\ I_f & I_f & I_{ff} \end{Bmatrix} \ , \end{aligned} \tag{A.9}$$

where $\begin{Bmatrix} L & L' & k \\ I_f & I_f & I_{ff} \end{Bmatrix}$ is the $6j$-symbol defined by [30]

$$\langle j_1, (j_2 j_3) J_{23}; J | (j_1 j_2) J_{12}, j_3; J\rangle = \tag{A.10}$$

$$(-1)^{j_1+j_2+j_3+J}\sqrt{(J_{12}+1)(2J_{23}+1)} \begin{Bmatrix} j_1 & j_2 & J_{12} \\ j_3 & J & J_{23} \end{Bmatrix} \tag{A.11}$$

with j_1, j_2 and j_3 being the three angular momenta coupling to a resultant angular momentum J. The multipole transition amplitudes $\delta_{\pi L}(1 \to 2)$ for γ radiation of multipolarity πL with frequency ω and wave number $k = \frac{\omega}{c}$ are given by [27]

$$\delta_{\pi L} = i^{s(L)}\sqrt{\frac{8\pi(L+1)}{L[(2L+1)!!]^2\hbar}\left(\frac{\omega}{c}\right)^{2L+1}} \frac{\langle I_2 || \mathcal{M}\pi L || I_1\rangle}{\sqrt{2I_1+1}} \ , \tag{A.12}$$

where $s(L)$ is given by

$$s(L) = \begin{cases} L & \text{for} \quad E\lambda \ , \\ L+1 & \text{for} \quad M\lambda \ . \end{cases} \tag{A.13}$$

Appendix B

Rotational model

In *collective* models the excitations are caused by collective motions of a nucleus, i.e. vibrational or rotational motion of the nucleus as a whole involving *all* nucleons.

In the *rotational* model the excitations are explained by collective rotations of deformed nuclei. For spherical nuclei an excitation due to a rotation is quantum mechanically forbidden, but possible by vibrational excitation.

B.1 Quadrupole moment and Deformation

The electric quadrupole moment of a nucleus is a measure of the extent to which the nuclear charge distribution deviates from spherical symmetry. For an axially deformed nucleus the intrinsic quadrupole moment Q_0 defined with respect to the body fixed symmetry axis is given by [30]

$$eQ_0 = \int (3z^2 - r^2)\rho(\mathbf{r})dV \ , \tag{B.1}$$

where $\rho(\mathbf{r})$ is the charge-density distribution. A positive Q_0 value corresponds to a prolate deformation, a negative to an oblate deformation. The intrinsic quadrupole moment Q_0 is related to the spectroscopic quadrupole moment Q by

$$Q = \frac{3K^2 - I(I+1)}{(I+1)(2I+3)} Q_0 \ , \tag{B.2}$$

where K is the projection of the total angular momentum I on the quantization axis of the intrinsic system. For an electric quadrupole ($E2$) transition the reduced transition probability $B(E2)$ is related to the intrinsic quadrupole moment Q_0 by the relation

$$B(E2; I_i \to I_f) = \frac{5}{16\pi} e^2 Q_0^2 \langle I_i K 20 | I_f K \rangle^2 \ , \tag{B.3}$$

where the Clebsch-Gordon-coefficient $\langle I_i K 20 | I_f K \rangle$ represents the coupling of the angular momenta in the intrinsic frame. In the special case of $I_i = 0^+$ and $I_f = 2^+$ with $K = 0$

$$B(E2; 0^+ \to 2^+) = \frac{5}{16\pi} e^2 Q_0^2 \tag{B.4}$$

is obtained.

For a statically deformed nucleus the radius in the intrinsic frame can be written as

$$R(\Theta, \phi) = R_0(1 + \beta_2 Y_{20}(\Theta, \phi)) \tag{B.5}$$

with the quadrupole deformation parameter β_2 and the nuclear radius R_0 (e.g. $R_0 = 1.2\,\mathrm{fm} \cdot A^{1/3}$). From B.1 in first order in β_2, the intrinsic quadrupole moment Q_0 is related to β_2 by

$$Q_0 = \frac{3}{\sqrt{5\pi}} R_0^2 Z \beta_2 \,, \tag{B.6}$$

where Z denotes the nuclear charge.

For the special case of an $E2$ transition from a state $I_i = 0^+$ to a state $I_i = 2^+$ the following relation between the quadrupole deformation parameter β_2 and the $B(E2)\uparrow$ value is obtained (by combining equations B.3 and B.4):

$$|\beta_2| = \frac{4\pi}{3} \frac{1}{ZeR_0^2} \sqrt{B(E2;\ 0^+_{\mathrm{g.s.}} \rightarrow 2^+_1)} \,. \tag{B.7}$$

A determination of the $B(E2)\uparrow$ value therefore allows to extract the magnitude of the quadrupole deformation parameter β_2 of the investigated nucleus.

B.2 Quadrupole moment and Reduced matrix element

The quadrupole moment Q is responsible for transitions between the magnetic sublevels of the same state and therefore related to the diagonal reduced matrix element of a state with angular momentum I by [30]

$$\langle I||\mathcal{M}(E2)||I\rangle = \sqrt{\frac{5(2I+1)}{16\pi}} \frac{1}{\langle II20|II\rangle} eQ \,. \tag{B.8}$$

In the framework of the rotational model the diagonal reduced matrix element can therefore be calculated from the $B(E2)\uparrow$ value as the quadrupole moment and the $B(E2)\uparrow$ are related through equation B.3.

Appendix C

Electromagnetic transitions and Collectivity

The reduced electric quadrupole transition probabilities, $B(E2)$, which can be extracted from the "safe" Coulomb excitation experiments presented in this work, are largely independent of nuclear models. By comparing experimentally determined $B(E2)$ values with predictions from theory it is possible to draw conclusions regarding the nature of the excitations and transitions.

C.1 Emission of electromagnetic radiation

As already mentioned in section 2.6, the emission of electromagnetic radiation is the most important decay channel for low-lying excited nuclear states. For the decay of an excited nucleus in an initial state I_i to a final state I_f, the γ-radiation of multipole order $\pi\lambda$ has to obey the usual selection rules

$$\begin{aligned} |I_i - I_f| \;\leq \lambda \leq\; & I_i + I_f, \\ \pi_i \pi_f \quad = \quad & \begin{cases} (-1)^{\lambda} & \text{for} \quad E\lambda, \\ (-1)^{\lambda+1} & \text{for} \quad M\lambda, \end{cases} \end{aligned} \tag{C.1}$$

where π_i and π_f are the parities of the initial and final nuclear states, respectively.

The life time of an excited nuclear state is strongly dependent on the multipolarity of the γ-transitions by which it can decay. The transition rate $\mathcal{W}$ per unit time of a given multipolarity $\pi\lambda$ for a nucleus in state I_i is given by [58]

$$\mathcal{W}(\pi\lambda; I_i \rightarrow I_f) = \frac{8\pi(\lambda+1)}{\lambda[(2\lambda+1)!!]^2} \frac{1}{\hbar} \left(\frac{E_\gamma}{\hbar c}\right)^{2\lambda+1} B(\pi\lambda; I_i \rightarrow I_f) \tag{C.2}$$

with E_γ being the energy of the emitted γ-ray and the reduced transition probability $B(\pi\lambda; I_i \rightarrow I_f)$. For multipolarity $E2$, which is the most important decay mode for the experiments described in this work, the transition rate is thus determined to be

$$\mathcal{W}(E2) = 1.22 \times 10^9 \cdot E_\gamma^5 \cdot B(E2) \;, \tag{C.3}$$

where the energy E_γ is given in units of MeV and the B(E2) value in $e^2\text{fm}^4$. As the life time τ of an excited state is related to the transition rate $\mathcal{W}$ by $\tau = \frac{1}{\mathcal{W}}$, the measurement of the reduced transition probability allows to extract the life time of an excited state with given transition multipolarity $\pi\lambda$.

C.2 Collectivity of transitions

The electromagnetic transition of a nucleus from an initial state I_i to the final state I_f may be the result of only *one* particle changing its state or may involve a change in motion of *many* particles. The resulting transition probabilities for such collective transitions with many particles being involved are in general much larger than for the case of only one nucleon involved [70]. By comparing the measured transition probabilities with the single-particle probabilities, the "collectivity" of the states involved in the transitions can be estimated and measured.

The approximations for the single-particle probabilities, assuming only one nucleon to be involved in the transitions, are referred to as Weisskopf single-particle estimates. In the following, only the results are outlined; a detailed derivation can be found in [58, 71].

For the reduced transition probabilities the Weisskopf single-particle estimates or Weisskopf units (W.u.) are found to be

$$B_W(E\lambda) = \frac{1}{4\pi}\left(\frac{3}{\lambda+3}\right)^2 1.2^{2\lambda} A^{2\lambda/3} e^2 fm^{2\lambda} \tag{C.4}$$

$$B_W(M\lambda) = \frac{10}{\pi}\left(\frac{3}{\lambda+3}\right)^2 1.2^{2\lambda-2} A^{(2\lambda-2)/3} \mu_N^2 fm^{2\lambda}\ , \tag{C.5}$$

where $E\lambda$ ($M\lambda$) denotes an electric (magnetic) transition of order λ. In equation C.5, μ_N denotes the nuclear magneton defined by

$$\mu_N = \frac{e\hbar}{2M_p c} \tag{C.6}$$

with M_p being the proton mass (M_p=938.3 MeV/c^2). As an example for $E2$ transitions, one Weisskopf unit (1 W.u.) corresponds to $B_W(E2)$=5.54 $e^2\text{fm}^4$ and $B_W(E2)$=6.04 $e^2\text{fm}^4$ for $A = 30$ and $A = 32$, respectively.

If for a given transition the experimentally found reduced transition probability is in agreement with the Weisskopf single-particle estimate, the excitation can be regarded as of single-particle nature. On the other hand, if the value is found to be much larger than the Weisskopf estimate, the excitation is caused by many nucleons acting together.

Appendix D

Coulomb excitation calculations

The Coulomb excitation calculations were performed using the coupled-channel codes CLX [28] and GOSIA [29]. In the following sections sample calculations with CLX and GOSIA are shown.

D.1 Sample CLX calculation

A sample CLX calculation is carried out for the case of the Coulomb excitation of the first 2^+ state (at 885.3 keV) of ^{32}Mg projectiles with a beam energy of 2.84 MeV/u on a ^{107}Ag target. In table D.1 the CLX input file with a description of the parameters is shown (see also the FORTRAN code `clx.f` for a description of the input parameters).

CLX input file	description
`2.84 MeV/u 32Mg -> 107Ag`	title
`11111111`	output control
`2 2 0.`	multipolarity parameters
`0.  0.  0.`	calculation parameters
`47 32`	$Z_t,\ A_p$
`12 107`	$Z_p,\ A_t$
`90.88`	total projectile energy [MeV]
`50.  50.  1`	$\Theta_{\mathrm{min}},\ \Theta_{\mathrm{max}},\ \Delta\Theta$
`1 0 0.0 1 0`	$N,\ J,\ E$ [MeV], $\pi,\ K$ (ground state)
`2 2 0.8853 1 0`	$N,\ J,\ E$ [MeV], $\pi,\ K$ (2_1^+ state)
`1 2 0.20833 2`	$N_1,\ N_2$, red. matrix element [eb], multipolarity ($E2$)
`2 2 -0.24900 2`	$N_1,\ N_2$, red. matrix element [eb], multipolarity ($E2$)

Table D.1: Sample CLX input file with description of parameters.

The two reduced matrix elements correspond to an assumed ^{32}Mg $B(E2)\uparrow$ value of $434\,e^2\mathrm{fm}^4$ and were calculated using equation 2.9 (for the reduced matrix element of

0.20833 eb for the transition from the 0^+ ground state to the 2_1^+ state) and equations B.2, B.3 and B.8 (for the diagonal reduced matrix element of -0.24900 eb according to the rotational model with an assumed prolate deformation), respectively.
After performing the Coulomb excitation calculation by running CLX with:

```
$ clx < file.clx
```

the output of the program will contain the following lines:

```
SCATTERING ANGLE IN CM SYSTEM = 50.00 DEGREES

LEVEL EXCITATION CM CROSS-SECTION
INDEX PROBABILITY [b/sterad]

 1 0.957795E+00 0.252876E+01
 2 0.422047E-01 0.112140E+00
```

The differential Coulomb excitation cross section for the excitation of the ^{32}Mg 2_1^+ state for the given conditions at a cm-scattering angle of Θ_{cm}=50° is therefore $\left(\frac{d\sigma}{d\Omega}\right)_{\mathrm{cm}}$= 112.1 mb/sr.

D.2 Sample GOSIA calculation

A sample GOSIA calculation is performed for the case of the Coulomb excitation of the 2_1^+ state of ^{30}Mg projectiles with a beam energy of 2.69 MeV/u on a ^{60}Ni target. The GOSIA input file is shown in table D.2 with a short description of the parameters (see GOSIA manual for a detailed parameter description).

The two reduced matrix elements correspond to an assumed ^{30}Mg $B(E2)\uparrow$ value of 253 e^2fm^4 and were calculated in the same way as for the CLX input file (see section D.1). After performing the GOSIA Coulomb excitation calculation with the command:

```
$ gosia < file.gosia
```

the output file will contain the following lines:

```
LEVEL 1 POPULATION 0.986936E+00
LEVEL 2 POPULATION 0.130643E-01
```

The probability to excite the ^{30}Mg 2_1^+ state for the given conditions at a lab-scattering angle of the ^{30}Mg ejectiles of Θ_{lab}=30° is therefore $P_{0^+_{\mathrm{g.s.}}\rightarrow 2_1^+} = 0.0131$. According to equation 2.1, the Coulomb excitation cross section can be obtained by multiplying the probability $P_{i\rightarrow f}$ with the corresponding Rutherford cross section $\left(\frac{d\sigma}{d\Omega}\right)_{\mathrm{Ruth}}$. From equations 2.2, 2.3 and 2.4 the Rutherford cross section for the cm-scattering angle of Θ_{cm}=44.5° (corresponding to

GOSIA input file	description
`OP,COUL`	option for calculation
`LEVE`	start of level input
`1,1,0,0.`	$N,\ \pi,\ J,\ E$ [MeV] (ground state)
`2,1,2,1.4822`	$N,\ \pi,\ J,\ E$ [MeV] (2_1^+ state)
`0,0,0,0`	end of level input
`ME`	start of matrix element input
`2,0,0`	multipolarity $E2$
`1,2,0.15906`	$N_1,\ N_2,$ red. matrix element $[eb]$
`2,2,-0.19011`	$N_1,\ N_2,$ red. matrix element $[eb]$
`0,0,0`	end of matrix element input
`EXPT`	start of experiment specifications
`1,12,30`	nr. of experiments, $Z_p,\ A_p$
`-28,60,80.7,30,5,1,0,0,360,0,1`	$Z_t,\ A_t,\ E_p$ [MeV], $\Theta_{\rm lab}$
	(see GOSIA manual for other parameters)
`OP,STAR`	option for calculation
`OP,EXIT`	exit

Table D.2: Sample GOSIA input file with description of parameters.

the lab-angle of $\Theta_{\rm lab}$=30°) is calculated to be $\left(\frac{d\sigma}{d\Omega}\right)_{\rm Ruth}$=2.459 b. A differential Coulomb excitation cross section of $\left(\frac{d\sigma}{d\Omega}\right)_{\rm cm}$= 32.1 mb/sr is thus obtained for the excitation of the ^{30}Mg 2_1^+ state at a ^{30}Mg lab-scattering angle of $\Theta_{\rm lab}$=30°.

Appendix E

Analysis software

For the analysis of the Coulomb excitation experiments presented in this work different analysis codes had to be developed: the data processing code itself, a code for the calibration of the detectors and a code for the optimization of the MINIBALL cluster positions. Short descriptions of the different codes and usage instructions are outlined in the following.

E.1 Data processing

The data processing executable reads in the raw data [72] written with the MARaBOU DAQ system [49], processes the data and writes the results to a ROOT [51] file. The data processing includes

- the positioning (in software) of the MINIBALL clusters according to the angles given in the configuration file,
- the eventbuilding for particles and γ-rays (see section 3.5),
- the kinematical reconstruction,
- the MINIBALL cluster addback (see section 4.2.1) and
- the use of pulse shape analysis (PSA) [25] to determine the γ-ray interaction points.

The analysis code consisting of different files can be compiled in the `evtbld` directory by `./m` . In table E.1 the most important files of the code are listed together with short descriptions.

file name	description
offl_ana.cc	main-file
ClAna.hh	header file containing class definition of analysis class ClAna
RootAna.hh	header file containing class definition of user-defined classes
AnaDefs.hh	header file containing experiment specific definitions
geometry.c	setting up of triple clusters in MINIBALL coordinate system
energy_range_ functions.cc	routines for energy loss calculations
med_sub.c	routines to read MED data and write it to the variables defined in hd.h
ClAna.cc	file containing event building
MBAna.cc	MINIBALL routines (e.g. PSA, cluster addback)
ParticleAna.cc	particle routines (i.e. particle building for CD-detector, kinematical reconstruction)
m, Makefile	makefiles

Table E.1: Description of most important analysis code files.

The usage of the executable "offl_root_med" is as follows (see also in the file offl_ana.cc):

```
  $ offl_root_med <PARAMETERS>

<PARAMETERS> is a list of 9 parameters:

  1:  input .med file
  2:  number of events to process ("-1" for all)
  3:  name of output ROOT file
  4:  filename with calibration factors for XIA DGF modules
  5:  filename with calibration factors for CAEN V785 ADC modules
  6:  filename with calibration factors for CAEN V775 TDC modules
  7:  config-file containing positions of 8 clusters in MB frame
  8:  window width for event building in μs (default:  4 μs)
  9:  reference point for eventbuilding (default:  0.5)
```

E.2 Energy calibration

The energy calibration code allows to determine calibration constants for the channels of the MINIBALL array from ^{60}Co and ^{152}Eu calibration data. In addition, the calibration of the channels of the $\Delta E - E$ telescope using a triple α source (consisting of ^{239}Pu, ^{241}Am and ^{244}Cm) is possible.
The usage of the calibration executable "`MBcal`" is as follows (see also the file `MBcal.cc` for examples):

```
  $ MBcal <PARAMETERS>

<PARAMETERS> is a list of 18 parameters:

  1:  calibration source:  "0":  60Co; "1":  152Eu; "2":  triple alpha
  2:  ROOT file with uncalibrated energy spectra
  3:  spectra names in ROOT file
  4:  input calibration file (if 152Eu calibration is wanted)
  5:  output file name with resulting calibration constants
  6:  output file name file for result of calibration
  7:  first channel to calibrate
  8:  last channel to calibrate
  9:  channel_output_flag:  set to "1" if more information is wanted
 10:  expected peak sigma (in bins) for peakfind routine
 11:  relative percentage for peakfind routine
 12:  fit_flag:  if "1", then peaks are fitted
 13:  fit_sigma:  sigma for routine FitSinglePeak()
 14:  fit_range:  range for fit
 15:  number of bins N (0-N) which are set equal to "0"
 16:  debug_flag:  if "1", then additional debugging is given
 17:  function_debug_flag:  if "1", more deb.  information is given
 18:  maximum ADC diff.  of found 152Eu peak pos.  to lit.  value
```

To obtain the ROOT file containing uncalibrated spectra for all XIA DGF and CAEN modules, the data has to be processed with the definition `#define CALIB_OUTFILE` in the file `AnaDefs.hh` instead of the usual `#define RUN` definition.

E.3 MINIBALL cluster position optimization

The Θ_c and α_c angles of the clusters in the MINIBALL coordinate system can be optimized by this code (see section 4.2.3).
The usage of the position optimization executable "`MBgeo_opt`" is as follows (see also the file `MBgeo_opt.cc` for examples):

```
$ MBgeo_opt <PARAMETERS>

<PARAMETERS> is a list of 33 parameters:

 1:  cluster number to be optimized
 2:  ALPHA-optimization-flag:  "1":  yes, "0":  no
 3:  if ALPHA-optimization:  minimum dalpha value
 4:  if ALPHA-optimization:  maximum dalpha value
 5:  if ALPHA-optimization:  step width of wanted dalphas
 6:  THETA-optimization-flag:  "1":  yes, "0":  no
 7:  if THETA-optimization:  minimum dtheta value
 8:  if THETA-optimization:  maximum dtheta value
 9:  if THETA-optimization:  step width of wanted dthetas
10:  input ROOT file
11:  selection for histograms ("cut")
12:  name of tree in ROOT file
13:  number of events to process of input ROOT file
14:  config file containing angles for all clusters
15:  energy (in keV) of γ-ray which is used for optimization
16:  uncertainty of upper γ-ray energy
17:  number of bins of histograms for optimization
18:  lower bin of histos (in keV)
19:  upper bin of histos (in keV)
20:  expected sigma (in bins) for peakfind routine
21:  relative percentage for peakfind routine
22:  max.  deviation (in bins) of maximum bin to peakfind position
23:  fit_flag (if "1" peak is fitted)
24:  sigma for fit
25:  range for fit
26:  maximum deviation (in keV) from peakfind position to fit position
27:  minimum number of required counts in maximum bin of histogram
28:  min.  number of required segments (per det.)  to fulfill cond.  "27"
29:  average β value (if "-1":  from ejectile; if "-2":  from recoil)
30:  distance from target to mean z-position in detector
31:  ratio where middle point in segment is placed ("0"-"1")
32:  debug_flag (if "1", additional debugging info is given)
33:  function_debug_flag (if "1", add.  function deb.  info is given)
```

Bibliography

[1] M. Goeppert Mayer, Phys. Rep. **75**, 1969 (1949).

[2] O. Haxel, J. Jensen, and H. Suess, Phys. Rep. **75**, 1766 (1949).

[3] T. Otsuka, Y. Utsuno, R. Fujimoto, B. Brown, M. Honma, and T. Mizusaki, Eur. Phys. J. A **15**, 151 (2002).

[4] C. Thibault, R. Klapisch, C. Rigaud, A. Poskanzer, R. Prieels, L. Lessard, and W. Reisdorf, Phys. Rev. C **12**, 644 (1975).

[5] X. Campi, H. Flocard, A. Kerman, and S. Koonin, Nucl. Phys. A **251**, 193 (1975).

[6] E. K. Warburton, J. A. Becker, and B. A. Brown, Phys. Rev. C **41**, 1147 (1990).

[7] B. H. Wildenthal and W. Chung, Phys. Rev. C **22**, 2260 (1980).

[8] G. Neyens, M. Kowalska, D. Yordanov, K. Blaum, P. Himpe, P. Lievens, S. Mallion, R. Neugart, N. Vermeulen, Y. Utsuno, et al., Phys. Rev. Lett. **94**, 022501 (2005).

[9] T. Motobayashi, Y. Ikeda, K. Ieki, M. Inoue, N. Iwasa, T. Kikuchi, M. Kurokawa, S. Moriya, S. Ogawa, H. Murakami, et al., Phys. Lett. B **346**, 9 (1995).

[10] B. Pritychenko, T. Glasmacher, P. Cottle, M. Fauerbach, R. Ibbotson, K. Kemper, V. Maddalena, A. Navin, R. Ronningen, A. Sakharuk, et al., Phys. Lett. B **461**, 322 (1999).

[11] H. Iwasaki, T. Motobayashi, H. Sakurai, K. Yoneda, T. Gomi, N. Aoi, N. Fukuda, Z. Fülöp, U. Futakami, Z. Gacsi, et al., Phys. Lett. B **522**, 227 (2001).

[12] V. Chisté, A. Gillibert, A. Lepine-Szily, N. Alamanos, F. Auger, J. Barrette, F. Braga, M. D. Cortina-Gil, Z. Dlouhy, V. Lapoux, et al., Phys. Lett. B **514**, 233 (2001).

[13] Y. Utsuno, T. Otsuka, T. Mizusaki, and M. Honma, Phys. Rev. C **60**, 054315 (1999).

[14] D. J. Dean, M. T. Ressell, M. Hjorth-Jensen, S. E. Koonin, K. Langanke, and A. P. Zuker, Phys. Rev. C **59**, 2472 (1999).

[15] S. Péru, M. Girod, and J. Berger, Eur. Phys. J. A **9**, 35 (2000).

[16] E. Caurier, F. Nowacki, and A. Poves, Nucl. Phys. A **693**, 374 (2001).

[17] M. Kimura and H. Horiuchi, Prog. Theo. Phys. **107**, 33 (2002).

[18] R. Rodríguez-Guzmán, J. Egido, and L. Robledo, Nucl. Phys. A **709**, 201 (2002).

[19] P. Stevenson, J. Rikovska Stone, and M. R. Strayer, Phys. Lett. B **545**, 291 (2002).

[20] Y. Utsuno, T. Otsuka, T. Mizusaki, and M. Honma, Nucl. Phys. A **704**, 50c (2002).

[21] M. Yamagami and N. V. Giai, Phys. Rev. C **69**, 034301 (2004).

[22] D. Habs, O. Kester, T. Sieber, H. Bongers, S. Emhofer, P. Reiter, P. Thirolf, G. Bollen, J. Äystö, O. Forstner, et al., Hyperf. Int. **129**, 43 (2000).

[23] E. Kugler, Hyperf. Int. **129**, 23 (2000).

[24] J. Eberth, G. Pascovici, H. Thomas, N. Warr, D. Weisshaar, D. Habs, P. Reiter, P. Thirolf, D. Schwalm, C. Gund, et al., Prog. Part. Nucl. Phys. **46**, 389 (2001).

[25] M. Lauer, Dissertation, Universität Heidelberg (2004), URL `http://www.mpi-hd.mpg.de/cb/theses.html`.

[26] K. Alder, A. Bohr, T. Huus, B. Mottelson, and A. Winther, Rev. Mod. Phys. **28**, 432 (1956).

[27] K. Alder and A. Winther, *Electromagnetic excitation: theory of Coulomb excitation with heavy ions* (North-Holland, 1975).

[28] H. Ower, coulomb excitation code CLX.

[29] T. Czosnyka, D. Cline, L. Hasselgren, C. Wu, R. Diamond, H. Kluge, C. Roulet, E. Hulet, R. Lougheed, and C. Baktash, Nucl. Phys. A **458**, 123 (1986).

[30] A. Bohr and B. Mottelson, *Nuclear Structure*, vol. 1 (W.A. Benjamin, Inc., 1969).

[31] F. de Boer, H. Wollersheim, H. Emling, H. Grein, E. Grosse, W. Spreng, G. Eckert, T. Elze, K. Stelzer, and C. Lauterbach, Z. Phys. A **325**, 457 (1986).

[32] W. Wilcke, J. Birkelund, H. Wollersheim, A. Hoover, J. Huizenga, W. Schröder, and L. Tubbs, Atom. Data and Nucl. Data Tab. **25**, 389 (1980).

[33] D. Cline, Ann. Rev. Nucl. Part. Sci. **36**, 683 (1986).

[34] Homepage of the ISOLDE facility, URL `http://isolde.web.cern.ch/ISOLDE/`.

[35] V. Fedoseyev, G. Huber, U. Köster, J. Lettry, V. Mishin, H. Ravn, and V. Sebastian, Hyperf. Int. **127**, 409 (2000).

[36] O. Kester, T. Sieber, S. Emhofer, F. Ames, K. Reisinger, P. Reiter, P. Thirolf, R. Lutter, D. Habs, B. Wolf, et al., Nucl. Instr. Meth. B **204**, 20 (2003).

[37] J. Cederkäll, F. Ames, P. Butler, P. Delahaye, V. Fedoseev, M. Lindroos, T. Nilsson, T. Sieber, F. Wenander, M. Pantea, et al., Nucl. Phys. A **746**, 17 (2004).

[38] F. Ames, G. Bollen, P. Delahaye, O. Forstner, G. Huber, O. Kester, K. Reisinger, and P. Schmidt, Nucl. Instr. Meth. A **538**, 17 (2005).

[39] C. Gund, Dissertation, Universität Heidelberg (2000), URL `http://www.mpi-hd.mpg.de/cb/theses.html`.

[40] H. Boie, Diplomarbeit, Universität Heidelberg (2002), URL `http://www.mpi-hd.mpg.de/cb/theses.html`.

[41] X-Ray Instrumentation Associates (XIA), URL `http://www.xia.com/`.

[42] L. Palafox Gamir, Dissertation, Universität Heidelberg (1997), URL `http://www.mpi-hd.mpg.de/cb/theses.html`.

[43] D. Weißhaar, Dissertation, Universität zu Köln (2002), URL `http://kups.ub.uni-koeln.de/frontdoor.php?source_opus=718`.

[44] M. Lauer, Diplomarbeit, Universität Heidelberg (2001), URL `http://www.mpi-hd.mpg.de/cb/theses.html`.

[45] J. Cub, C. Gund, D. Pansegrau, G. Schrieder, and H. Stelzer, Nucl. Instr. Meth. A **453**, 522 (2000).

[46] A. Ostrowski, S. Cherubini, T. Davinson, D. Groombridge, A. Laird, A. Musumarra, A. Ninane, A. di Pietro, A. Shotter, and P. Woods, Nucl. Instr. Meth. A **480**, 448 (2002).

[47] N. Warr, MINIBALL electronics at CERN (2004), URL `http://www.ikp.uni-koeln.de/~warr/doc/electronics_Jul2004.pdf%`.

[48] CAEN Technologies, Inc., URL `http://www.caen.it/`.

[49] R. Lutter et al., MARaBOU Data Aquisition System, URL `http://www.bl.physik.uni-muenchen.de/marabou/html/`.

[50] F. Köck, Dissertation, Universität Heidelberg (1994).

[51] ROOT, An Object-Oriented Data Analysis Framework, URL `http://root.cern.ch/`.

[52] R. Firestone, *Table of Isotopes*, vol. 8 (John Wiley & Sons, Inc., 1996).

[53] Evaluated Nuclear Structure Data File (ENSDF), URL http://www.nndc.bnl.gov/ensdf/index.jsp.

[54] U. Köster, V. N. Fedoseyev, A. N. Andreyev, U. C. Bergmann, R. Catherall, J. Cederkäll, M. Dietrich, H. De Witte, D. V. Fedorov, L. Fraile, et al., Nucl. Instr. Meth. B **204**, 347 (2003).

[55] V. Bildstein, Master's thesis, Universität Heidelberg (2005), URL http://www.mpi-hd.mpg.de/cb/theses.html.

[56] GEANT4, URL http://geant4.web.cern.ch/geant4/.

[57] H. Boie, GEANT4 MINIBALL simulation, URL http://www.mpi-hd.mpg.de/mbwiki/wiki/MiniballSimulation.

[58] D. Pelte and D. Schwalm, *In-beam gamma-ray spectroscopy with heavy ions* (North-Holland, 1982), vol. 3, p. 1.

[59] S. Raman, C. W. N. Jr., and P. Tikkanen, Atom. Data and Nucl. Data Tab. **78**, 1 (2001).

[60] M. Bhat, Nucl. Data Sheets **80**, 789 (1997).

[61] M. King, Nucl. Data Sheets **69**, 1 (1993).

[62] P. Raghavan, Atom. Data and Nucl. Data Tab. **42**, 189 (1989).

[63] O. Kenn, K.-H. Speidel, R. Ernst, J. Gerber, P. Maier-Komor, and F. Nowacki, Phys. Rev. C **63**, 064306 (2001).

[64] J. Blachot, Nucl. Data Sheets **89**, 213 (2000).

[65] R. Kozub, C. Chitwood, D. Fields, C. Lister, J. Olness, and E. Warburton, Phys. Rev. C **28**, 2343 (1983).

[66] J. Meng, I. Tanihata, and S. Yamaji, Phys. Lett. B **419**, 1 (1998).

[67] P. Bevington and D. Robinson, *Data Reduction and Error Analysis for the Physical Sciences*, vol. 2 (McGraw-Hill, Inc., 1992).

[68] O. Niedermaier, H. Scheit, V. Bildstein, H. Boie, J. Fitting, R. von Hahn, F. Köck, M. Lauer, U. Pal, H. Podlech, et al., Nucl. Phys. A **752**, 273 (2005).

[69] O. Niedermaier, H. Scheit, V. Bildstein, H. Boie, J. Fitting, R. von Hahn, F. Köck, M. Lauer, U. Pal, H. Podlech, et al., Phys. Rev. Lett. **94**, 172501 (2005).

[70] A. deShalit and H. Feshbach, *Theoretical Nuclear Physics Vol. 1: Nuclear Structure* (John Wiley & Sons, Inc., 1974).

[71] S. Wong, *Introductory Nuclear Physics* (Prentice-Hall, Inc., 1990).

[72] R. Lutter, MED Data Structure description, URL `http://www.bl.physik.tu-muenchen.de/marabou/html/doc/MedStruc%ture.pdf`.

Danksagung

An dieser Stelle möchte ich mich bei allen bedanken, die mich während der Entstehung dieser Arbeit begleitet, unterstützt und zum Gelingen beigetragen haben. Besonders hervorheben möchte ich:

- Herrn Prof. Dr. Dirk Schwalm, der mir diese Arbeit ermöglichte und durch viele Vorschläge, Ideen und Diskussionen maßgeblich zu ihrer Entstehung beigetragen hat,
- Herrn Dr. Heiko Scheit für die sehr gute Betreuung und für die Hilfe und Unterstützung bei allerlei kleineren und größeren Problemen,
- Herrn Prof. Dr. Hans Emling für die Übernahme des Zweitgutachtens,
- die aktuellen und ehemaligen Mitglieder der CB-Gruppe am MPI-K für das sehr gute Arbeitsklima und die nette Atmosphäre, wobei ich hier besonders Vinzenz Bildstein, Hans Boie, Jörg Fitting, Dr. Frank Köck und Dr. Martin Lauer nennen möchte,
- alle Mitglieder der MINIBALL- und REX-ISOLDE-Kollaborationen, die nicht zuletzt durch die Übernahme von Schichten während der experimentellen Kampagnen am CERN zur Entstehung der Arbeit beigetragen haben,
- alle Mitarbeiter des Max-Planck-Instituts für Kernphysik in Heidelberg,
- meine Freunde und meine Komilitonen vom Sommersemester 1996,
- meine Familie, wobei ich hier insbesondere meine Eltern, meine Brüder und meine Großeltern erwähnen möchte, und
- vor allem Ina Kyas für ihre unermüdliche und liebevolle Unterstützung.